ABSTRACT

Title of Dissertation: EFFECTS OF PREHEATED COMBUSTION AIR ON LAMINAR COFLOW DIFFUSION FLAMES UNDER NORMAL AND MICROGRAVITY CONDITIONS

Mohammad Ghaderi Yeganeh, Doctor of Philosophy, 2005

Dissertation Directed By: Professor Ashwani K. Gupta
Department of Mechanical Engineering

Global energy consumption has been increasing around the world, owing to the rapid growth of industrialization and improvements in the standard of living. As a result, more carbon dioxide and nitrogen oxide are being released into the environment. Therefore, techniques for achieving combustion at reduced carbon dioxide and nitric oxide emission levels have drawn increased attention. Combustion with a highly preheated air and low-oxygen concentration has been shown to provide significant energy savings, reduce pollution and equipment size, and uniform thermal characteristics within the combustion chamber. However, the fundamental understanding of this technique is limited.

The motivation of the present study is to identify the effects of preheated combustion air on laminar coflow diffusion flames. Combustion characteristics of laminar coflow diffusion flames are evaluated for the effects of preheated combustion air temperature under normal and low-gravity conditions. Experimental

measurements are conducted using direct flame photography, particle image velocimetry (PIV) and optical emission spectroscopy diagnostics. Laminar coflow diffusion flames are examined under four experimental conditions: normal-temperature/normal-gravity (case I), preheated-temperature/normal gravity (case II), normal-temperature/low-gravity (case III), and preheated-temperature/low-gravity (case IV). Comparisons between these four cases yield significant insights.

In our studies, increasing the combustion air temperature by 400 K (from 300 K to 700 K), causes a 37.1% reduction in the flame length and about a 25% increase in peak flame temperature. The results also show that a 400 K increase in the preheated air temperature increases CH concentration of the flame by about 83.3% (CH is a marker for the rate of chemical reaction), and also increases the C_2 concentration by about 60% (C_2 is a marker for the soot precursor). It can therefore be concluded that preheating the combustion air increases the energy release intensity, flame temperature, C_2 concentration, and, presumably, NO_x production.

Our work is the first to consider preheated temperature/low-gravity combustion. The results of our experiments reveal new insights. Where as increasing the temperature of the combustion air reduces the laminar flame width under normal-gravity, we find that, in a low-gravity environment, increasing the combustion air temperature causes a significant increase in the flame width.

EFFECTS OF PREHEATED COMBUSTION AIR ON LAMINAR COFLOW DIFFUSION FLAMES UNDER NORMAL AND MICROGRAVITY CONDITIONS

By

Mohammad Ghaderi Yeganeh

Dissertation submitted to the Faculty of the Graduate School of the
University of Maryland, College Park, in partial fulfillment
of the requirements for the degree of
Doctor of Philosophy
2005

Advisory Committee:
Professor Ashwani K. Gupta, Mechanical Engineering, Chairman/Advisor
Associate Professor Gregory S. Jackson, Mechanical Engineering
Associate Professor Keith Herold, Mechanical Engineering
Assistant Professor Bao Yang, Mechanical Engineering
Associate Professor Ken Yu, Aerospace Engineering

Dedication

to my parents, my wife, and my children

Acknowledgements

I first would like to thanks ALLAH, through whom all things are possible. All praise and thanks are due to Him.

I would like to thank Professor Ashwani K. Gupta for affording me this research opportunity, and for his support during this research work.

My appreciation goes also to my doctoral committee members: Professor Jackson, Professor Herold, Professor Yu, and Professor Yang. I thank them for their guidance, assistance and willingness to serve on my committee. My special thanks are to Professor Ohadi for introducing me to the program at the University of Maryland.

I would like to extend my sincere thanks to Professor Mahmoud Salehi; Sharif University of Technology, for his continuous support, encouragement and invaluable assistance that he provided during my education at Sharif University as well as University of Maryland.

I also would like to thank Professor K. Kitagawa; Nagoya University, for his invaluable assistance in the development of the experimental facility.

Professor C. T. Avedisian; Cornell University, is acknowledged for providing drop tower test opportunity.

This research was supported by NASA microgravity combustion research program. This support is gratefully acknowledged.

I would like to thank all my friends at the combustion lab for their invaluable assistance and many great discussions that we had.

I am forever indebted to my parents. Their love, dedication, and help were always the foundation of my work and patience during this long course of learning. I also want to

express my thanks to my wife for her endless understanding, patience, and support when it was needed. My special thanks to my children, who suffered from not having much time and fun with their dad.

Table of Contents

List of Tables

List of Figures

List of Symbols

A	Einstein coefficient
Bi	Biot number
C	number of particles per unit volume
C_p	specific heat
d	jet exit diameter
d_i	particle image diameter
d_p	diameter of particle
E^*	excited energy
Fo	Fourier number
Fr	Froud number
Gr	Grashof number
g	degeneracy in the excited state
h	Plank's constant
k	thermal conductivity
K	Boltzmann constant
L	characteristic heated length
L_f	flame length
M	magnification of the lens
N*	population in the excited state
N_{tot}	total number of species
P	pressure
Q(T)	partition function

Re	Reynolds number
Re_L	characteristic Reynolds number of diffusion flame
Ri	Richardson number
S	band emission intensity
Sr	Strouhal number
T	local temperature
T_a	ambient temperature
T_0	flame or wall temperature
t	time
t_c	characteristic time
u_F	forced flow velocity
u_{f0}	uniform average fuel velocity
u_{a0}	uniform average air stream velocity
u_{iner}	velocity based on viscous shear-buoyancy force balance
U	flow velocity vector
U_g	gravitationally induced velocity
U_s	velocity lag
U_p	particle velocity
V	velocity
w	luminous flame diameter
z	streamwise distance
Z_{st}	stoichiometric mixture fraction
α	thermal diffusivity

δ characteristic thickness of the viscous or thermal layer

ζ normalized stream wise distance

θ' nondimensionalized temperature

μ viscosity

ν kinematic viscosity

ρ local density

τ relaxation time

Φ_v viscose dissipation

χ_c anharmonic constant

1 Introduction

1.1 Environment and Energy Conservation

Global energy consumption has been increasing around the world due largely to rapid growth of industrialization and improvement in the standard of living. Increasing emissions of carbon dioxide and nitrogen oxide into environment are the direct results of this increased energy consumption. Therefore energy consumption in a way to prevent environmental damages has become of great concern. Presently and in the foreseeable future, environmental preservation is a matter of great urgency. For that reason, those techniques that can provide combustion with simultaneous reduction of carbon dioxide and oxides of nitrogen emissions have drawn increased attention.

The Toronto congress held in 1988, fifteen years after the first oil crisis, was the first official meeting to declare the need for action in terms of global warming issues. In 1992, the United Nations Conference on the Environment and Development adopted the United Nations Framework Convention on Climate Change. This was enforced in March 1994. In addition, the Kyoto Protocol, which was adopted at COP3 (the Kyoto Protocol to the United Nation Framework Convention on Climate Change) in 1997 to determine the detailed targets associated with the reduction of carbon dioxide emissions for individual developed country by 2010. These were determined on the basis of 1990 emission levels and had been successfully adopted by developed countries by 2002.

During 1960s to early 1970s, two serious problems emerged as the result of combustion technologies. The first problem was pollutant emission, such as sulfur oxide, nitrogen oxide and smog generated by combustion, and the other was requirement for efficient use of energy caused by the oil crisis. With the oil crisis of 1973, the problem of the energy crisis was thrust to the forefront. Attention was focused on the development of a combustion system with low fuel consumption and using various low-grade fuels.

An ultra-lean mixture is defined as fuel/air lean premixed gas mixture with the fuel concentration near to the lower flammability limit. Because combustion of this ultra-lean mixture had not been possible under usual conditions, a new method to accelerate the reaction by using some type of mechanism has been sought. Research on the combustion of ultra-lean mixtures at the combustion limit has been a challenge to combustion engineers and attractive to researchers in the field. Because ultra-lean mixtures do not burn under normal pressure and temperature conditions, it becomes necessary for the mixture to accelerate the reaction by methods such as: (1) catalytic oxidation using a catalyst, (2) injection of active elements such as high energy radicals, (3) preheating, or (4) increase of pressure.

Among these, except for oxidation with catalyst, interest has been focused on a method of preheating the ultra-lean mixture using a heat recirculation method [1]. The heat recirculation method mentioned here is proposed as a method of preheating the unburned mixture without using external energy. The method provides a means of recirculating the heat from the high temperature side (burned gas) back to the unburned mixture side using an appropriate heat exchanger method. The preheating

gives additional enthalpy to the unburned mixture without dilution by the combustion products. The methods of recovering waste heat and preheating combustion air using various types of heat exchangers have been employed primarily to improve thermal efficiency and stable combustion [1].

1.2 Excess Enthalpy Combustion for Low Heating Value Fuels

In 1971, Weinberg [2,3] of Imperial College introduced the fact that preheating the mixture using the heat recirculation method can attain stable combustion of an ultra-lean mixture and expand the flammability limits of the mixture. He proposed the concept of additional enthalpy combustion for ultra-lean mixtures. A special feature of this method is that a heat source for preheating is not necessary to maintain combustion except at the time of start-up. Furthermore, the temperature of the final exhaust gas does not necessarily become high.

The novelty of Weinberg's idea lies in maintaining sustained combustion without any assistance from an external heat source, for example, by applying the heat recirculation method used in conventional industrial furnaces for an ultra-lean mixture. In this case, the success of applying the heat recirculation method depends on (1) whether or not a heat exchange method is appropriate and (2) how much of the heat loss from a combustion unit can be reduced. Although various heat exchange methods have been proposed, the major heat recirculation methods studied to date can be broadly classified into (1) indirect (external) heat recirculation methods and (2) direct (internal) heat recirculation methods.

1.3 Internal and External Heat Recirculation Methods

The indirect (external) heat recirculation methods are methods of circulating heat at the exterior of a flame zone without essentially changing the structure of the flame as represented by the double spiral type burner proposed by Lloyd and Weinberg [2,3], namely, a so-called Swiss Roll burner. The indirect (external) heat recirculation methods can further be classified into methods that mainly utilize conduction only or methods that actively utilize radiation for the heat feedback. For these methods, a combustor was proposed wherein a porous solid wall is positioned to enclose the combustion chamber [1], because the porous solid wall has the function of converting the sensible heat of gas into radiation energy at a high conversion efficiency. When burned gases behind the flame pass through porous solid wall, the sensible heat is converted into radiation energy and the unburned mixture is preheated using this radiation energy.

In contrast, the direct (internal) heat recirculation methods [1] are methods of feeding back heat directly from the side of burned gases to the side of unburned gases by inserting, for example, a porous metal with high thermal conductivity into the flame zone, changing the internal structure of the flame and forming an additional enthalpy flame. It is called heat-recirculation combustion in which reactants are heated prior to the flame zone by heat transfer from burned products without mixing of the two streams [4]. The temperature histories of premixed combustion in a one-dimensional adiabatic system are schematically compared in Figure 1.1 for the cases with and without heat recirculation. The maximum temperature in heat recirculating combustion is determined by the amount of recycled heat that is independent of the

equivalent ratio of the mixture or the calorific value of the fuel used. This is certainly true for adiabatic premixed combustion. Accordingly it has been held that heat-recirculating combustion brings a temperature rise throughout combustion processes in proportion to the amount of recycle heat.

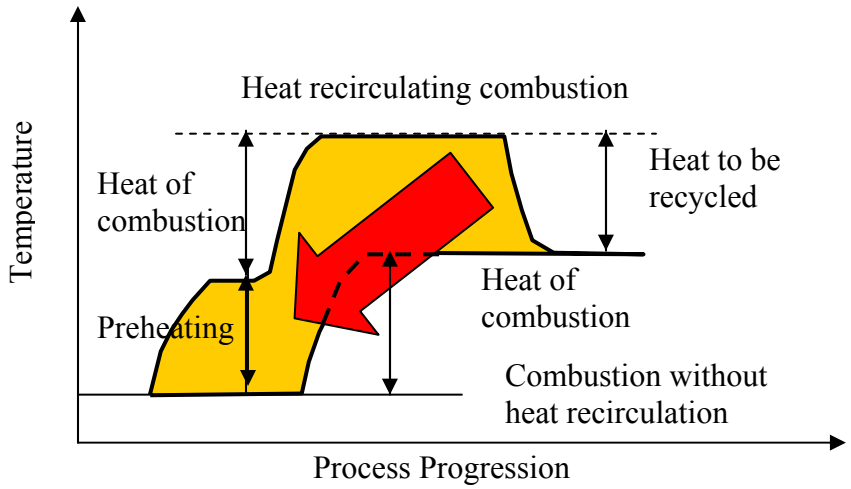

Figure 1.1 Temperature History of the Heat-Recirculation Combustion of Premixed Reactant in One-Dimensional Adiabatic System [1]

1.4 Flammability Limits

Figure 1.2 shows the effect of preheating combustion air on flammability limits, however the type of flame used in this figure is premixed flame. At normal ambient temperature, an ordinary hydrocarbon gaseous fuel mixed with atmospheric air exhibits a flammable region around stoichiometric mixture. An increase of temperature of the mixture expands the flammability limits significantly, as illustrated in Figure 1.2. A large increase in the temperature may cause auto-ignition. In contrast, if a fuel of low calorific value is adopted, the flammable region disappears at

ambient temperature and reappears when the mixture is preheated over a certain temperature level, as shown in the Figure 1.2 exhibiting conceptual trends.

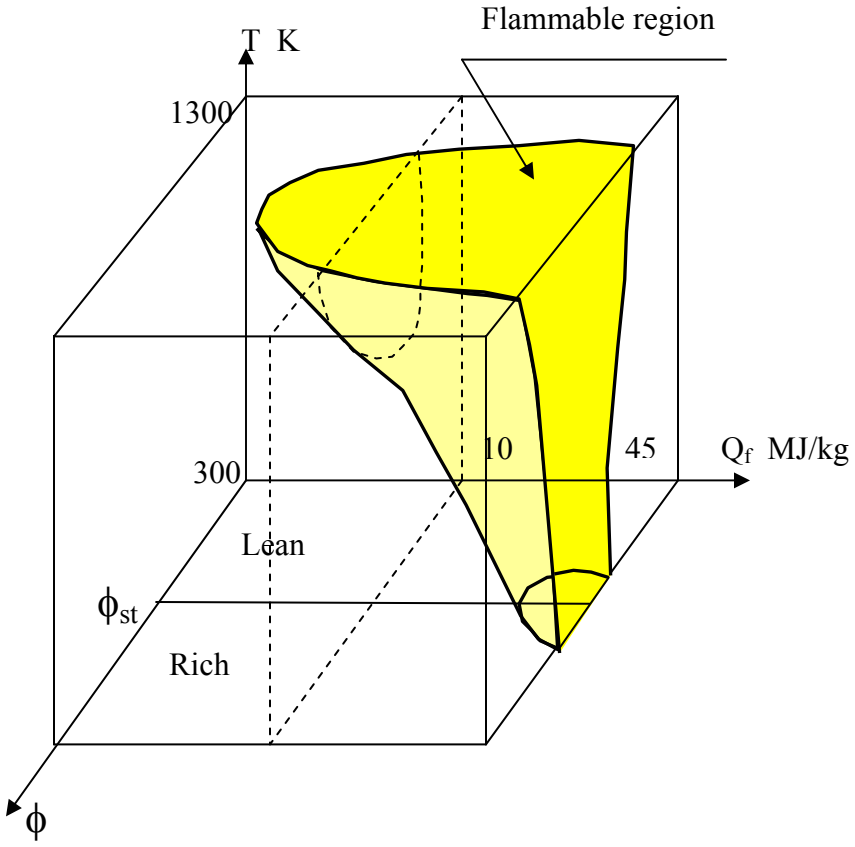

Figure 1.2 Flammable Domain Expressed by Calorific Value of Fuel, Q_f, Initial Temperature of Mixture, T_f, and Mixture Equivalence Ratio, ϕ [1]

1.5 Objectives, Methods and Scope of Dissertation Work

The overall objective of the present study is to identify the effect of preheated combustion air on laminar coflow diffusion flames. Combustion characteristics of laminar coflow diffusion flames are evaluated for the effects of preheated combustion

air temperature under normal and low-gravity conditions. Specific objectives of the dissertation work are as follows:

- Examine the global preheated combustion air laminar diffusion flame structure and shape under normal gravity conditions
- Provide detailed information on the flowfield associated with preheated combustion air laminar coflow diffusion flame under normal gravity conditions using Particle Image Velocimetry (PIV) techniques
- Determine the selected radicals distribution within the flame using optical emission spectroscopy techniques and create a three-dimensional, spatial distribution of these radicals to observe the effect of preheated combustion air on the laminar diffusion flame front and reaction rate
- Obtain vibrational temperature distributions of preheated combustion air laminar diffusion flame using C_2 vibrational bands
- Examine the effects of low-gravity on laminar coflow diffusion flame at preheated combustion air temperature using a 1 second free-fall drop tower
- Compare laminar coflow diffusion flame at normal and preheated combustion air temperature under low gravity conditions

Experimental measurements are conducted using direct flame photography, particle image velocimetry (PIV) and optical emission spectroscopy diagnostics. Laminar coflow diffusion flames are examined under four experimental conditions: normal-temperature/normal-gravity (case I), preheated-temperature/normal gravity

(case II), normal-temperature/low-gravity (case III), and preheated-temperature/low-gravity (case IV). Comparisons between these four cases yield significant insights as follows:

- First, compare case I with case II to reveals the effect of preheating the combustion air under normal-gravity conditions. The results thus obtained are then used to form the basis for comparison with the corresponding results obtained under low-gravity conditions. In both cases I and II, direct flame photography, particle image velocimetry (PIV) and optical-emission spectroscopy diagnostics are all employed to examine the laminar coflow diffusion flames. Direct flame photography is applied to acquire information about the global flame structure, shape and intensity. PIV diagnostics are used to provide a better understanding of the effects of preheated combustion air upon the flowfield. The PIV data provides detailed information on the dynamics of the flow associated with preheated combustion air conditions, two components of its mean and rms velocity, its strain rate and 2-D vorticity. The effect of preheated air upon the propane-air diffusion flame is measured by optical-emission spectroscopy. In these experiments, the spatial distributions of flame temperature are determined from the conventional two–line method, using C_2 vibrational bands. An Abel transformation is applied to create a three-dimensional, spatial distribution of selected radicals within the flame.

- Study comparison of case I and III from literature. The motivation of these studies has been theoretical; although microgravity combustion has few real-world applications, it is easier to model. Modeling of diffusion flame without the influence of gravity has somewhat less complication and provides a convenient comparison with the experimental data. In other words, because of buoyancy, analytical and most numerical models assume this potential influence can be neglected. Such assumptions are not available in experiments, conducted at earth's gravity, intended to validate these models. Many investigators have examined flame shape and appearance under normal and low-gravity conditions and using different fuel types and different techniques to reduce the effects of gravity (see chapter 2 for more details).

- Compare cases II and IV to study the effects of low gravity on laminar coflow diffusion flame at preheated combustion air temperature. The experimental facility used for low gravity is the same as that used for normal gravity conditions. Measurements of laminar jet diffusion flame shapes under low gravity conditions are carried out using a 1 second free-fall drop tower. Direct flame photography is the only diagnostic that applied in order to obtain the global characteristics of the flame.
- Finally, comparing case III and IV, involves the effects of preheating combustion air on laminar coflow diffusion flame under microgravity conditions. For comparing, Lin and Faeth correlations [12] are used to obtain

flame length and width for normal temperature combustion air under low gravity conditions.

2 Laminar Diffusion Flame in Microgravity

2.1 Introduction

The objective of this chapter is to review the investigations of laminar diffusion flames under microgravity conditions. Many investigators have examined the flame shapes and appearances under normal and low gravity conditions and using different fuel types and different techniques to reduce the effects of gravity. Later on the correlations reviewed in this chapter will be used to compare with the results of experiments with preheated combustion air flame under low gravity conditions examined in this present study. In the following chapter it will be explained that buoyancy forces has important role to maintain the combustion air for the diffusion flame. Density differences are responsible for this buoyancy forces.

The following analysis in this chapter also shows the importance of buoyancy force compared with the viscous shear force. A simple phenomenological consideration can help to quantify the limitations caused by the potential intrusion of buoyancy motion due to gravity during experiments with diffusion flames. Nondimensionalized variables are needed for such analysis, which are obtained for natural convection using momentum and energy equations. Under microgravity conditions, the diffusion flame behavior would be different. Microgravity or other conditions that minimize effects of gravity are used, to eliminate the difficulties of flame studies on earth. The large density changes owing to combustion induce complex buoyant flows at normal gravity. Therefore activities like measurement or

observations of important phenomena would be complicated. The present discussion emphasizes on laminar diffusion flame in gases such as laminar jet diffusion flames in still and coflowing gases. This discussion will be applied in analyzing the results taken by preheated combustion air flame experiments under microgravity conditions.

Naturally, the intrusion of buoyancy becomes more problematic for laminar jet diffusion flames as jet velocities decreases. This behavior is inconvenient because it implies that Stokes flow regime at small Reynolds numbers cannot be reached for flame studies without the intrusion of earth's gravity. Stokes flow regime in which the inertial forces can be neglected is an important limit that has been invaluable for understanding non-reactive fluid mechanics. Thus, buoyant non-premixed flames are a common experimental configuration, for lack of an alternative, even though buoyancy causes complications and introduces phenomena that have little relevance to most practical applications. Even these circumstances are problematic, however, because large buoyant velocities cause flames to develop thin boundary layer-like structures that limit spatial resolution available for measurements. An additional difficulty due to effects of earth's gravity is that gas velocities progressively increase with increasing flame size; this eventually cause laminar flames to become turbulent and introduces problems of complex flame geometry and unsteady flame behavior, which further complicate measurements [5,6].

2.2 Influence of Gravity on Flames

Under the influence of gravitational field, gaseous combustion products, whose densities at the flame front are typically ten times less than unburnt reactants at

standard temperature and pressure, separate and then will rise [8]. The density differences generate buoyancy forces that drive the flow. This serves to provide new reactants to a fire or ignition source. The density differences depend upon temperature or concentration gradients; for example, the density of the product gases is related, through an equation of state, to the temperature term in the energy equation. In the momentum equation, the hydrostatic pressure, itself a function of density variation, combines with the gravitational body force acting on the fluid to drive the flow. The momentum and energy equations couple through the density variations. Thus, the set of partial differential equations for natural convection problems is coupled, non-linear, and usually elliptical, and the equations must be solved simultaneously. When combustion processes and the associated finite-rate chemical kinetics are added to the problem, solution of the basic equations to even the simplest of combustion systems is often complicated processes. Therefore simplification and approximations are often utilized.

In the Boussinesq approximation, density variation is neglected in the mass continuity equation, and is approximated as a pure temperature effect in the momentum equation (pressure effects are neglected). Another simplification is the neglect of axial diffusion and of a balance of transverse momentum, i. e. the boundary layer approximation. The thickness of the velocity and thermal boundary layers are fortuitously almost identical for combustion gases, further simplifying the governing equations [7]. In most practical combustion applications, natural convective influence is necessary neglected, often without scientific justification.

The estimate of characteristic velocity can be based on balance between the buoyancy force and either the inertial or viscous terms in the momentum equation. Rather than equivalence with the internal force, the boundary force can be balanced with the viscous term, and the characteristic velocity becomes

$$u_{vis} = \delta^2 g(\Delta\rho/\mu) \qquad (2.1)$$

or

$$u_{vis} = \delta^2 (g/\mu)\rho(\Delta T/T) \qquad (2.2)$$

where δ is a characteristic thickness of the (unknown) viscous or thermal layer (for gases, these are nearly identical). The choice between inertia and viscous shear as the balancing force with buoyancy force with buoyancy depends on the magnitude of the Grashof number. With $Gr > 1$, a boundary layer type of flow exists and it is more appropriate to balance buoyancy with inertia. When $Gr < 1$, the latter balance of forces gives a better estimate of the magnitude of buoyancy-induced velocity in the flame.

When both forced and buoyant convection are present, the characteristic velocity is generally chosen as the known forced flow velocity, u_F, and the resulting important coefficient upon non-dimensionalization of the momentum equation of the momentum equation is:

$$Gr/Re^2 = (\Delta\rho/\rho)(gL/u_F^2) \qquad (2.3)$$

Noting that the gas density ratio is approximately unity in most combustion systems, the remaining group (gL/u_F^2) is a Richardson number, Ri, or an inverse Froud number, Fr. This group compares the relative importance of the natural and imposed flow.

Most analytical and numerical methods assume the influence of buoyancy can be neglected, due to its complications. Such assumptions are not available in experiments; conducted under normal gravity, intend to validate these models. For buoyancy to be negligible, the magnitude of Gr (Grashof number) and Ri (Richardson number) should at most be of order 10^{-1}. One potential way to minimize buoyancy-driven flow in combustion systems is to utilize low pressure [9]. However, low pressure may not make complete non-buoyant flow. The effect of gravity on an object can be reduced to very small level by being located at a sufficiently large distance away from the earth's surface or by placing the object in free fall.

2.2.1 Quantifying Gravitational Disturbance

Simple phenomenological considerations can help to quantify the limitations caused by gravity during fundamental experiments with homogeneous diffusion flames. The potential intrusion of buoyant motion due to gravity can be represented by Grashof number, and by Richardson number [10]. For flame, it can be estimated that $\Delta\rho/\rho \approx 1$ because the density of the reactants is large compared with the density of the combustion products, and $Gr < O(10^{-1})$ for effects of buoyant motion due to gravity to be small [11]; as a result $L < O$ (100 μm) is required for non-buoyant behavior at normal gravity for typical value of ν (10 mm^2 S^{-1}) in flames at atmospheric pressure. Clearly, such dimensions are too small for reasonable spatial resolution using available or anticipated combustion apparatus and instrumentation.

Experiments in the presence of finite flow velocities, where convective transport is important, provide a way of circumventing the limitations of molecular

transport represented by the Grashof number. The Richardson number, Ri, is a measure of the relative importance of buoyant motion due to gravity and a characteristic forced convective velocity of the flame, u_F, e.g. the burner exit velocity of a jet diffusion flame burning in a still environment. The physical basis for this parameter can be seen by finding the characteristic velocity of buoyant motion when a light gas rises a distance L [10].

$$u_B = (\Delta\rho g L/\rho)^{1/2} \qquad (2.4)$$

The characteristic velocity of buoyant motion is based on the balance between buoyant and inertial forces; effects of molecular transport will be considered subsequently. Forming the ratio of the square of these velocities then yields the Richardson number, where Ri << 1 denotes conditions where the intrusion of buoyancy is small.

Effects of molecular transport of mass, momentum, and thermal energy (heat) are central issues for diffusion flames. These effects can be conveniently interpreted in terms of momentum transport, however, because the ratios of heat and mass diffusivities are nearly unity in gaseous environments of interest to combustion phenomena, e.g. the dimensionless numbers representing those ratios, the Prandtl, Pr, and Schmidt, Sc, numbers, are nearly unity for gases. It is then convenient to interpret transport effects as a ratio of a convective velocity, u_F, to a characteristic molecular transport velocity, υ/L, by defining a characteristic Reynolds number of diffusion flames, Re_L, as follows:

$$\mathrm{Re}_L = Lu_F/\nu = (Gr/Ri)^{1/2} \qquad (2.5)$$

The L appearing in equation (2.5) is associated with some dimension of the luminous region of the flame as originally specified in the definition of Gr and Ri. Noting that $Gr = O(10^3)$ for a flame length of 10 mm (which provides reasonable spatial resolution for measurements) at atmospheric pressure from Grashof equation, whereas $Ri < O(10^{-1})$ for forced motion to dominate buoyant motion due to gravity [10], equation (2.5) then yields

$$Re_L > 10^2 \qquad (2.6)$$

This result helps to quantify the difficulties of carrying out studies at small Reynolds numbers where effects of forced motion are small, which is already evident from the discussion of Grashof equation. The small Reynolds number problem can be expressed more directly in terms of the Reynolds number based on the fluid jet diameter, d, which typically is used to characterize the convective conditions of jet diffusion flames, defined as follows:

$$Re = du_F / \upsilon \qquad (2.7)$$

Then, combining equations (2.4) and (2.6) gives (for $Ri < 1$)

$$Re > 10^2 / (L/d) \qquad (2.8)$$

Noting that laminar jet diffusion flame typically have $L/d = O(10)$ to provide boundary layer like flows that are convenient for analysis [12-16] equation (2.13) yields

$$Re > 10 \qquad (2.9)$$

in order to control the intrusion of gravity. This implies that the Stokes flow regime ($Re < 1$), which is a natural limit that had been invaluable for gaining a better understanding of fluid mechanics, cannot be reached during diffusion flame studies

on earth without the intrusion of gravity. Thus, buoyant non-premixed flames are a common configuration for flame studies on earth for lack of an alternative, even though effects of buoyant motion complicate measurements and introduce phenomena that have little relevance to practical flames.

Flow velocities in non-buoyant round laminar jet diffusion flames in still air gases tends to decrease in inverse proportion to distance from the jet exit, whereas the characteristic buoyant convection velocity, u_B, tends to increase in proportion to the square root of the distance from the jet exit; this implies that effects of fluid motion due to gravity become progressively more important with increasing distance from the jet exit.

2.3 Laminar Jet Diffusion Flames in Still Gases

Laminar diffusion flames are of interest because they provide model flame systems that are far more tractable for analysis and experiments than more practical turbulent diffusion flames. Laminar diffusion flames also merit study because understanding their transport and chemical reaction process is a necessary precursor to understanding these processes in turbulent diffusion flames.

2.3.1 Jet Flame in Still Gases

There are several experiments, which have been carried out to obtain the shapes of non-buoyant laminar jet diffusion flames using either drop towers to provide microgravity environments [16-22] or aircraft facilities [16] to provide low gravity environments. A series of studies had done along this line of laminar jet

diffusion flames using a 2.2 second free-fall drop tower due to Cochran and co-workers [17,18].

Studies following the work of Cochran and coworkers, due to Bahadori and coworkers [20-22] sought to resolve potential effects of transient flame development and soot luminosity on measurements of the shape of non-buoyant round laminar jet diffusion flames using both 2.2 second and 5.2 second drop towers. Sunderland et al. [16] considered the luminous flame lengths of non-buoyant soot-containing round laminar jet diffusion flames as part of a study of the laminar smoke point properties of non-buoyant laminar diffusion flames. In their studies, Cochran and coworkers, Bahadori and coworkers, and Sunderland et al. all observed a linear correlation between luminous flame length and fuel flow rates, independent of jet exit diameter, for each fuel burning in air. This behavior also is typical of the luminous flame length of buoyant round laminar jet diffusion flames [23]. Thus, to the extent that this linear relationship is retained for truly steady and non-buoyant laminar jet diffusion flames, it offers an important characteristic useful for testing flame shape predictions.

The shapes of laminar jet diffusion flames also have attracted significant theoretical attention. Measured flame lengths for both soot-free and soot-containing flames have been used to developed empirical models and to evaluate theoretical predictions for a range of buoyant conditions. The most well known empirical model for laminar diffusion flames is the linear correlation between the luminous flame length and the corresponding fuel flow rate [23] that was mentioned earlier. Burke and Schumann [24] modeled a classical example of a laminar diffusion flame. Their flame contained fuel and airflow with the same linear flow velocity in coaxial

cylinder tubes. Several laminar diffusion flame models of varying complexity also have been proposed [11,14,25-28] that successfully predict the linear correlation between stoichiometric flame lengths and the fuel flow rates (or equivalently between the stoichiometric flame length normalized by the jet exit diameter and the jet exit Reynolds number). Among these, the analysis of Spalding [11] (which is described in detail by Kuo [25]) offers a potentially simple and robust method for estimating the shapes of steady non-buoyant round laminar jet diffusion flames. Nevertheless, modifications of this approach to deal with soot containing flames (as opposed to soot free flames), the capabilities of this approach to estimate (or correlate) all flame shape properties (as opposed to simply luminous flame lengths), and the performance of this approach for truly steady and non-buoyant round laminar jet diffusion flames, are all issues that need to be addressed.

2.3.2 Theoretical Method

Lin et al. [13] used the simplified analysis of non-buoyant round laminar jet diffusion flames due to Spalding [11] to develop a convenient method to help interpret and correlate laminar jet diffusion flame in still air (Figure 2.1). Major assumptions of the analysis are as follow: steady, axisymmetric laminar jet diffusion flame; negligible effects of buoyancy; small effects of changes in kinetic energy and viscous dissipation; larger flame aspect ratio so that the boundary layer approximation apply and effects of the details of jet exit conditions can be replaced by jet invariants for the conservation of mass, momentum, and energy in the integral sense; thin film sheet involving fast chemistry; diffusivities of mass, momentum, and

energy are all equal; constant thermophysical and transport properties; and small effects of radiation.

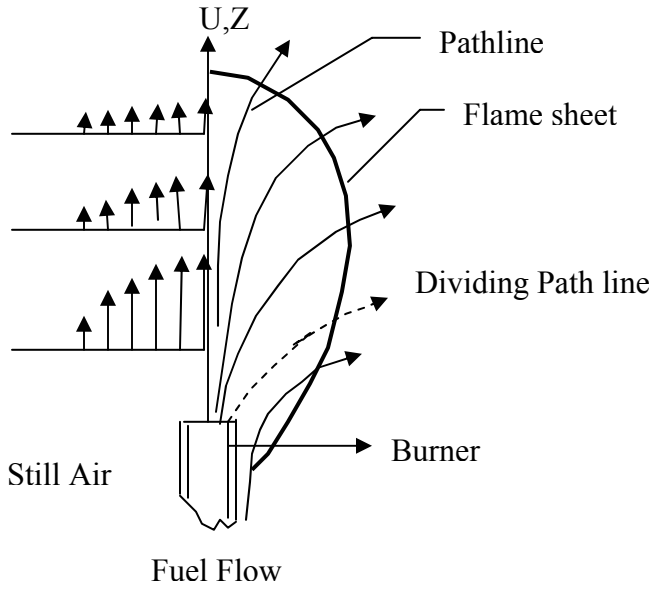

Figure 2.1 Sketch of Flame Structure for a Non-Buoyant Laminar Jet Diffusion Flames in a Still Gas [13]

The property assumptions are not satisfied for laminar jet diffusion flames, however, and are only adopted so that simple flame shape formulas could be obtained, motivated by the past success of similar approximations for analysis of the shapes of laminar jet diffusion flames, given the basic solution, correlation of the measurements was sought by selecting conditions to find mean transport properties and introducing some empirical parameters to match measurements and predictions.

Solution of the governing equations using the assumptions, after association the location of the luminous flame boundary with the location of the thin flame sheet

where the stoichiometric mixture fraction is reached, yield the following expression for the luminous flame length [13]:

$$L_f / d = (3/32)\mathrm{Re}Sc/Z_{st} \qquad (2.10)$$

L_f: distance from jet exit to luminous flame tip

d: jet exit diameter

Re: jet Reynolds number

Z_{st}: stoichiometric mixture fraction

The value of Z_{st} can be found simply as the mass fraction of burner exit fluid (fuel) in a stoichiometric mixture of burner-exit fluid and ambient fluid (air). The variation of Z_{st} is not large for combustion of hydrocarbon/air mixtures. The corresponding expression for the flame shape, yielding the flame diameter as a function of streamwise distance, is as follows [13]:

$$wZ_{st}/d = 3^{1/2}(z/L_f)\left[(L_f/z)^{1/2} - 1\right]^{1/2} \qquad (2.11)$$

w: luminous flame diameter

z: streamwise distance

Differentiating equation (2.11) and setting the result equal to zero, provides expression for the maximum flame diameter and the streamwise distance where this maximum diameter is reached [13] as:

$$W_{MAX}\ Z_{st}/d = 9/16 \qquad at \qquad z/L_f = 9/16 \qquad (2.12)$$

Correlation of the measurement was sought by selecting conditions to find mean transport properties and introducing some empirical parameters to match measurements and predictions. First of all, the equal diffusivity approximation was

relaxed by introducing the Schmidt number into equation (2.10) to get equation (2.13) because the flame sheet is mainly affected by mass transport properties represented by the Schmidt number. Transport properties affect equations (2.10 – 2.12) through the Schmidt number and the viscosity used to compute the Reynolds number. It was found that a reasonable correlation of luminous flame lengths could be obtained by approximation these properties by the properties of air at the average of the adiabatic flame temperature and the ambient temperature. The reason for this selection is for flames burning in air, nitrogen dominates the composition of both air and bulk of the flame. The range of the flame shape correlations was extended to flames having small aspect ratios by introducing a virtual origin at a distance L_0 from the jet exit, which is a conventional step for properties like luminous flame length. The flame length expression was then fine-tuned by introducing an empirical coefficient, C_f, as empirical flame length parameter. With these changes, equation (2.10) for the luminous flame length becomes [13]:

$$(L_f - L_0)/d = (3C_f/32)\mathrm{Re}Sc/Z_{st} \tag{2.13}$$

While equation (2.11) for the luminous flame diameter becomes [14]

$$wZ_{st}/d = 3^{1/2}\zeta(\zeta^{1/2} - 1)^{1/2} \tag{2.14}$$

ζ: normalized streamwise distance

where

$$\zeta = (z - L_0)/(L_f - L_0) \tag{2.15}$$

Thus, the flame radius properties are only indirectly affected by assumed transport properties, through the computation of the flame length of equation (2.13).

2.3.3 Comparison With Measured Data

The expression of equations (2.13) and (2.14) yield reasonable predictions of luminous flames shapes, given the correlation for L_0 and C_f of Table 2.1. Typical results for flames in still air are illustrated in Figure 2.2. For ethylene-(tests 03E and 16E) and Propane - (test 18P) fueled flames from the LSP experiments. Test conditions involved still air at ambient temperature of 300K, ambient pressure of 35-130 kPa, initial jet diameter of 1.6 and 2.7 mm, and jet exit Reynolds flame lengths of 15-63 mm.

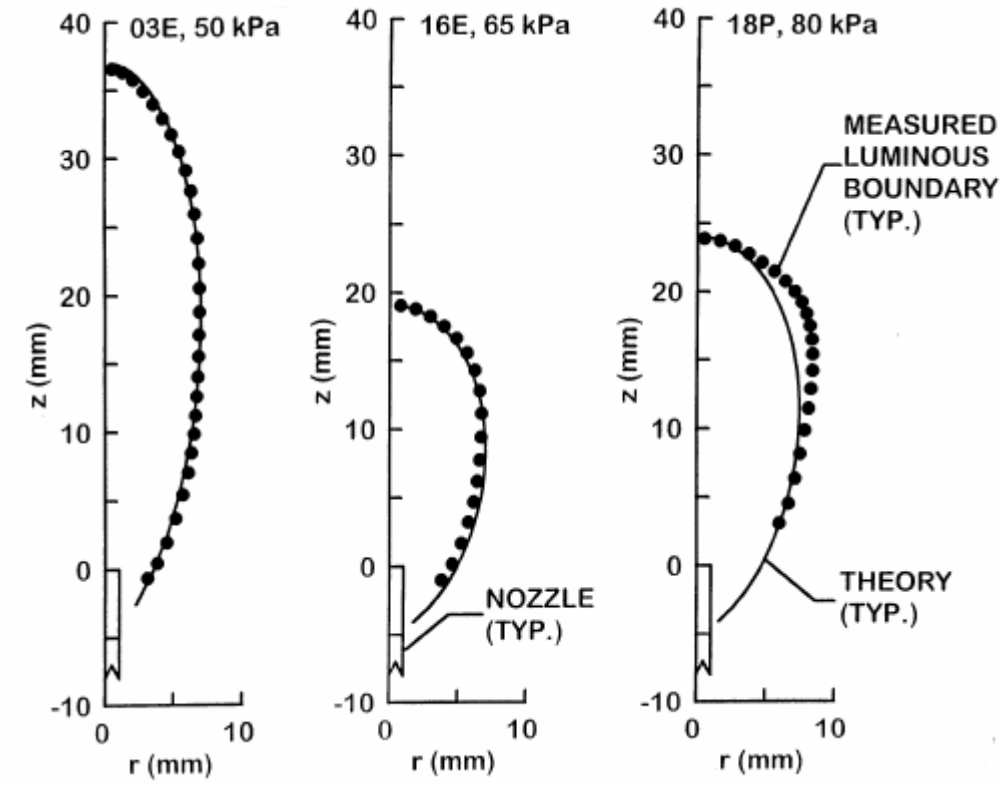

Figure 2.2 Measured and Predicted Luminous Flames Shapes for Typical Closed Tip Non-Buoyant Round Hydrocarbon-Fueled Luminous Jet Diffusion Flames in Still Air (tests 03E, 16E, and 18P from the LSP experiment) [13]

These test conditions involved soot-containing luminous flames near laminar smoke point conditions, and include both non-sooting and sooting flames.

2.4 Jet Flames in Coflowing Gases

Lin and Faeth [12] extend their study to consider the shapes of non-buoyant round laminar jet diffusion flames in coflowing air, prompted by the widespread use of this configuration to study the structure and soot formation processes of laminar diffusion flames. Similar to their study for flame in still air, a way to correlate flame shape results was sought, based on simplified analysis of non-buoyant laminar coflowing jet diffusion flames.

2.4.1 Background

Another advantage of the laminar coflowing jet diffusion flame configuration is that it has been widely used to study the soot formation properties of diffusion flames [24], [31-33]. While fast mixing reduces soot formation within diffusion flames, past studies of both laminar opposed and coflowing jet diffusion flame show that the way that mixing is carried out is important as well [34-40]. In fact, existing evidence from both laminar and turbulent jet diffusion flames, and from empirical industrial practice, suggests that soot reductions can be achieved most effectively by ensuring that velocities normal to the flame sheet are directed from the fuel rich toward the fuel lean side. This configuration, called “soot-formation-oxidation flame condition” by Kang et al. [37], tends to reduce the residence times of soot formation

conditions by drawing these materials directly through the flame sheet toward fuel lean oxidation conditions. in contrast, when velocities normal to the flame sheet are directed from the fuel lean toward the fuel rich side called "soot formation flame conditions" by Kang et al. [37], residence times of soot precursors and soot at fuel rich soot formation conditions are enhanced, making oxidation of these materials more problematic when oxidation conditions are finally reached.

Studies of effects of velocities normal to the flame sheet on soot formation have been carried out in laminar opposed and coflowing jet diffusion flames [34-40]. During most of these studies [34-37], velocities normal to the flame sheet were varied by varying the compositions of the oxidant- and fuel-carrying streams. As pointed out by Sunderland et al. [36], however, these composition changes alone are sufficient to retard soot formation and enhance soot oxidation, which tends to reduce soot concentrations, obscuring the effect of hydrodynamics on soot control. In addition, the practical utility of varying reactant-stream compositions to control soot formation in diffusion flames is relatively limited. Dai and Faeth [41] sought a direct evaluation of effects of velocities normal to the flame sheet on soot formation in diffusion flame by considering pure air and fuel reactant streams for laminar coflowing diffusion flames. Their measurements showed that laminar soot-point flame lengths and fuel flow rates can be increased, broadening the range of fuel flow rates where the flames remain soot free, by increasing air/fuel stream velocity ratio. The mechanism of the effect involves the magnitude and direction of flow velocities relative to the flame sheet where increased air/fuel stream velocity ratios cause progressive reduction of flame residence times in the fuel rich soot formation region. The range of soot free

conditions is limited by both liftoff, particularly at low pressure, and the intrusion of effects of buoyancy on effective air/fuel stream velocity ratios, particularly at high pressures. By modifying Syed et al. [42] soot model, numerical simulations from Kaplan and Kailasanath [39] exhibit similar tendencies for soot concentrations within laminar coflowing jet diffusion flames to decrease for locally enhanced air stream velocities. They used the ability of numerical simulations to provide detailed information on temperature, velocity, and species concentration distributions and to numerically track soot particles as they are convected through the flame.

2.4.2 Theoretical Method

The configuration for analysis of non-buoyant round laminar jet diffusion flames in coflowing gases is illustrated in Figure 2.3. Except for changed ambient flow properties, this analysis was carried out under the same assumptions as the analysis of flame in still air. The approach is limited to self-similar behaving far from the source so that the details of source properties are not important; therefore, the source is represented by uniform average fuel and air-stream velocities $u_{f,o}$ and $u_{a,o}$. the mixture fractions (defined as the fraction of mass at point that originated from the source fuel stream) of the source fuel and air streams are $f_{f,o}$ = 1and $f_{a,o}$ = 0 by definition. The enthalpy defect of the source can be defined in an analogous way, but this is not necessary because conservation of energy principles are not needed to find flame shapes under the present assumptions. The streamwise velocity defect is defined as follows [12]:

$$u_d = u_{a,o} - u \qquad (2.16)$$

noting that the air stream velocity approaches $u_{a,o}$ at all distances from the sources, based on above assumption. In the far field, where self similar behavior is approached, $u_d / u_{a,o} << 1$ and quadratic and higher terms in u_d can be neglected in governing equations, then, under the present approximations, the governing equation for conservation of mixture fraction can be found in the same manner as the far field formulation of laminar wake processes, as follows [12]

$$u_{a,o}\frac{\partial f}{\partial x}=\frac{\nu}{r}\frac{\partial}{\partial r}\left(r\frac{\partial f}{\partial r}\right) \tag{2.17}$$

$r = 0: \quad \partial f/\partial r = 0, \qquad r\rightarrow \infty: \ f = 0$ (2.18)

the final condition of the analysis is conservation of the flow of fuel stream mass in the streamwise direction, which can be written as follows in far field [12]:

$$\int_0^\infty frdr=\frac{d^2 u_{f,o}}{8u_{a,o}} \tag{2.19}$$

the solution of these equations can be obtained using either conventional separation of variables or conversion into an ordinary differential equation by a suitable similarity transformation. The resulting expression for the mixture fraction distribution in the self-similar regime is as follows [12]:

$$f=u_{f,o}d^2\exp\{-\eta^2)/(16\nu x) \tag{2.20}$$

where

$$\eta=(r/2)[u_{a,o}/(\nu x)]^{1/2} \tag{2.21}$$

the location of the luminous flame boundary is assumed to coincide with the location of the thin flame sheet where the concentrations of fuel and oxidizer are zero and the stoichiometric mixture fraction is reached, $f = Z_{st}$.

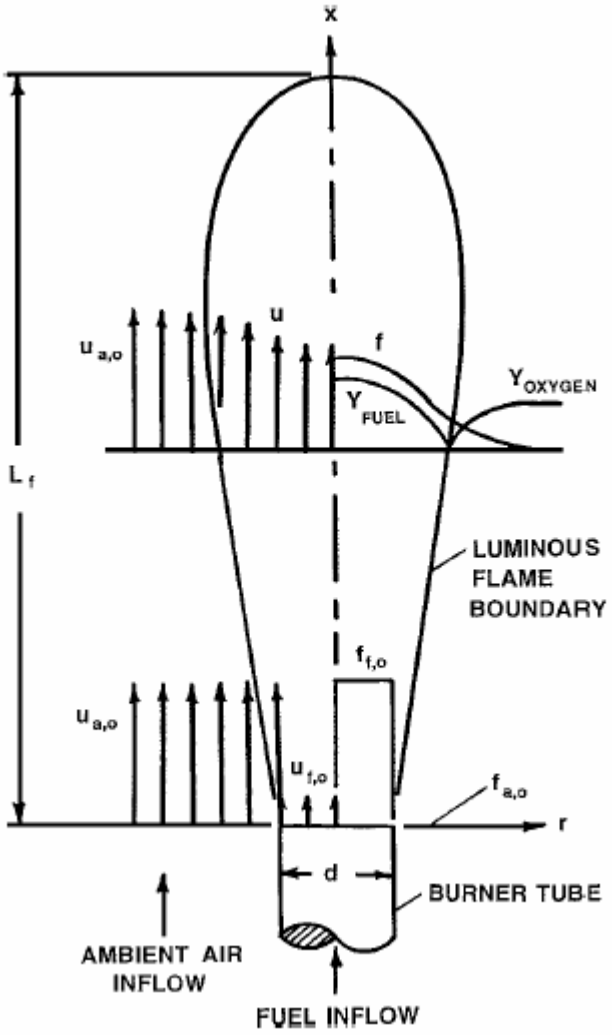

Figure 2.3 Sketch of Flame Structure for Non-Buoyant Round Laminar Jet Diffusion Flame in a Coflowing Gas [12]

Introducing this mixture fraction into equation (2.20), for conditions along the flame axis, yields the following expression for luminous flame length [12]:

$$\frac{L_f}{d} = \frac{\mathrm{Re}}{16 Z_{st}} \tag{2.22}$$

the corresponding expression for flame shape, providing the flame diameter as a function of streamwise distance, is as follows [12]:

$$w/d=[(x/L_f)(u_{f,o}/u_{a,o})\ln\{L_f/x\}/Z_{st}]^{1/2} \quad (2.23)$$

Finally, a convenient measure of the flame diameter is its value at $x/L_f = ½$, as follows [12]:

$$w_{1/2}/d=[(u_{f,o}/u_{a,o})\ln\{2\}/(2Z_{st})]^{1/2} \quad (2.24)$$

Correlation of the measurement was sought in the same manner as Lin et al [13]. The equal diffusivity approximation was relaxed by introducing the Schmidt number into equation (2.22); the Schmidt number and viscosity used to compute the Reynolds number where taken from the properties of air at the average of the adiabatic flame temperature and the ambient temperature; the correlation of flame length was improved at small aspect ratio by introducing a virtual origin at a distance L_0 from the jet exit; and the flame length correlation was fine-tuned for effects of soot luminosity, by introducing the empirical coefficient C_f as discussed later. With these changes, equation (2.22) for the luminous flame length becomes [12]

$$\frac{(L_f - L_0)}{d} = \frac{C_f \,\mathrm{Re} Sc}{16 Z_{st}} \quad (2.25)$$

Whereas equation (2.23) for the luminous diameter becomes [12]

$$w/d=[-\zeta(u_{f,o}/u_{a,o})\ln\{\zeta\}/Z_{st}]^{1/2} \quad (2.26)$$

Where

$$\zeta = \frac{(x - L_0)}{(L_f - L_0)} \quad (2.27)$$

Equation (2.25) indicates that luminous flame lengths in coflow are proportional to the mass flowrate of fuel and independent of coflow velocity, similar to flames in still gases, but they are only 2/3 as long. Direct effects of coflow velocity manifest

themselves with respect to flame diameters, which are proportional to $d(u_{f,o} / u_{a,o})^{1/2}$ from equation(2.26).

2.4.3 Experimental Results

A portion of the measured and predicted lengths of non-buoyant flames in still and coflowing air is plotted in Figure 2.4. Corresponding values of L_0 and C_f used in the correlations of equations (2.13) and (2.25) are summarized in Table 2.1.

The measurements and predictions in Figure 2.4 can be separated into four groups as follows: laminar smoke point flame length in still gas correlated according to equation (2.13) from Lin et al. [13]; laminar smoke point flame lengths in strong coflow with $u_{a,o}/u_{f,o} > 1$, $Fr_a > 0.1$, correlated according to equation (2.25) from Lin and Faeth [12]; laminar soot point flame lengths in still gases correlated according to equation (2.13) from Xu et al.[43]; and laminar soot point flame length in strong coflow with $u_{a,o}/u_{f,o} > 0.5$ and $Fr_a > 1$ correlated according to equation (2.13) from Xu et al. [43]. The results illustrated for soot points in Figure 2.4 also agree with length of the luminous blue flame sheet for conditions exceeding the soot point, as mentioned earlier, the measurement for all four conditions are in good agreement with the corresponding correlations from equations (2.13) and (2.25), particularly the view of the approximate nature of the simplified theories.

The luminous flame lengths for still gases are appreciably longer than for strong coflow for both laminar smoke and soot point conditions, for example, L_f (still air) / L_f (coflowing air) $\approx$ 3/2 in agreement with equations (2.13) and (2.25). In addition, the length of soot-free flames is only roughly half that of soot containing

flames at the laminar smoke point for results in still air and in coflowing air respectively.

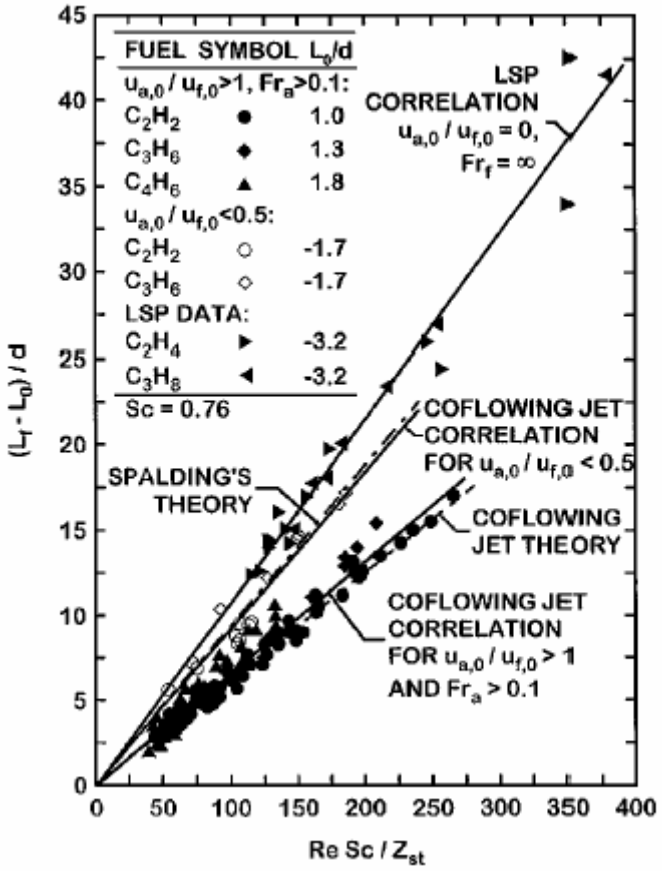

Figure 2.4 Luminous Flame Lengths of Round Hydrocarbon-Fueled Laminar Jet Diffusion Flames Burning in Still and Coflowing Air: Smoke Point Flame Lengths in Still Gas from Lin et al. [13], Smoke Point Flame Length in Coflow from Lin and Faeth[12], Soot Point Flame Lengths in Still Gas from Xu et al. [43], and Soot Point Flame Lengths in Coflow from Xu et al.[43] (Reproduced from [12])

These differences are mainly due to different locations of luminous flame lengths, associated with the presence of soot and the stoichiometric flame sheet as the laminar smoke point is approached. The evaluation of prediction for flames in coflowing air can be considered from results illustrated in Figure 2.5, where measurements and predictions for various jet exit and ambient conditions are plotted

for acetylene – fueled flames. The approximate analysis is seen to provide good predictions of trends in the far field with respect to variations in air/fuel velocity ratio and Reynolds numbers.

Table 2.1 Summaries of Flame Length Correlations for Non-Buoyant Round Laminar Jet Diffusion Flame [7]

Flame system	Source	L_0/d	C_f
Still or slowly coflowing air surroundings,			
Space-based, soot-containing system in still air ($u_{a,o}/u_{f,o}=0$, $Fr_a = \infty$)	Urban et al. [33]	-3.2	1.13
Ground based, soot containing system in slow coflow ($0.22 \leq u_{a,o}/u_{f,o} \leq 0.5$)	Lin and Faeth [12]	-1.7	0.97
Ground base, soot free system in slow coflow ($u_{a,o}/u_{f,o} < 0.2$ and $Fr_f > 5$)	Xu et al. [43]	0.0	0.54
Ground based, KC-135,soot containing system in still	Sunderland et al. [32]	0.4	0.8
Ground base, soot free system in still air	Sunderland et al. [16]	2.4	0.56
Coflowing air surroundings, $u_{a,o}/u_{f,o} > 0.5$, $Fr_a > 0.1$			
Ground based, soot containing system in fast coflow	Lin and Faeth [12]	1.4	1.05
Ground base, soot free system in fast coflow	Xu et al. [43]	0.0	0.5

Predictions near the nozzle, however, are not satisfactory owing to failure of the far-field approximations, which has been observed by others [44].

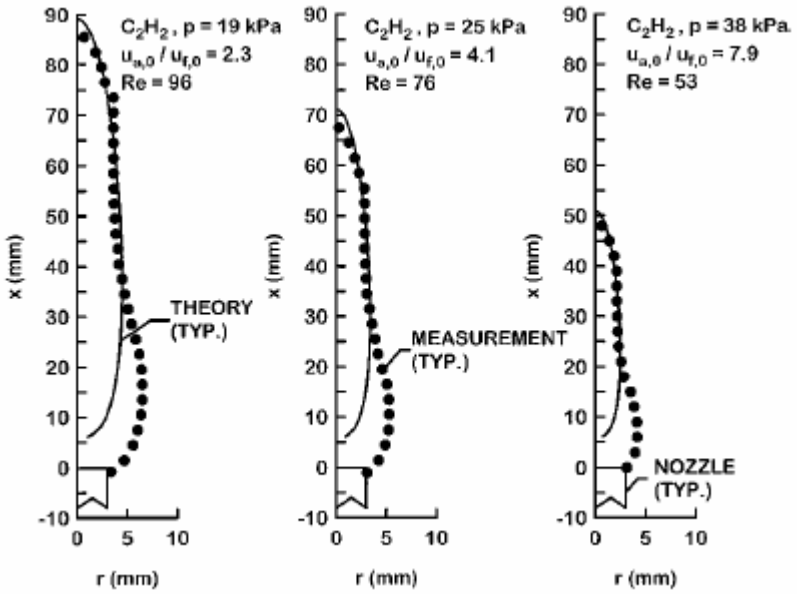

Figure 2.5 Measured and Predicted Laminar Flame Shapes for Typical Acetylene Fueled Non-Buoyant Round Laminar Jet Diffusion Flames in Coflowing Air at Various Conditions [12]

The evaluation of the predictions of equations (2.13) and (2.25) based on the results illustrated in Figures 2.3 to 2.5 is encouraging and shows that they provide a simplified way to estimate the shapes of round laminar jet diffusion flames. The luminous flame shapes are useful because they provide a simple non-intrusive measurement to help gain insight into the properties of laminar diffusion flames.

3 Experimental Test Facility, Diagnostics, and Methods

3.1 Experimental Test Facility

The experimental facility used for normal gravity is the same as that used for low gravity conditions. The facility consists of hardware, which is equipped into the metal frame to form the experimental packages. The experiments are conducted to examine the behavior of flame in normal and low gravity conditions. Since in low gravity experiments, the whole facility drops from a tower, the tightness of equipments inside the frame is very important issue. The only diagnostic that is applied for experiments under low gravity condition is direct flame photography. The normal gravity experiments are conducted using the facility that has been used in microgravity conditions. Different types of diagnostics such as Direct flame photography, particle image velocimetry and optical emission spectroscopy have been used for experiments under normal gravity conditions. Modification is done on the facility to conduct the experiments using diagnostics such as PIV and optical emission spectroscopy.

3.1.1 Experimental Test Facility for Use in 1 second Drop Tower

A photograph of the experimental apparatus used is shown in Figure 3.1. The facility equipped with the components, which are installed into two levels in the main frame. The parts that installed into the upper level are glass combustion chamber, image and data acquisition system including CCD camera and digital camcorder and the parts that installed into the bottom level are electrical system, fuel line, air line,

coolant line, and preheater. The components are described in the following section and more details of every component are put in Appendix at the end.

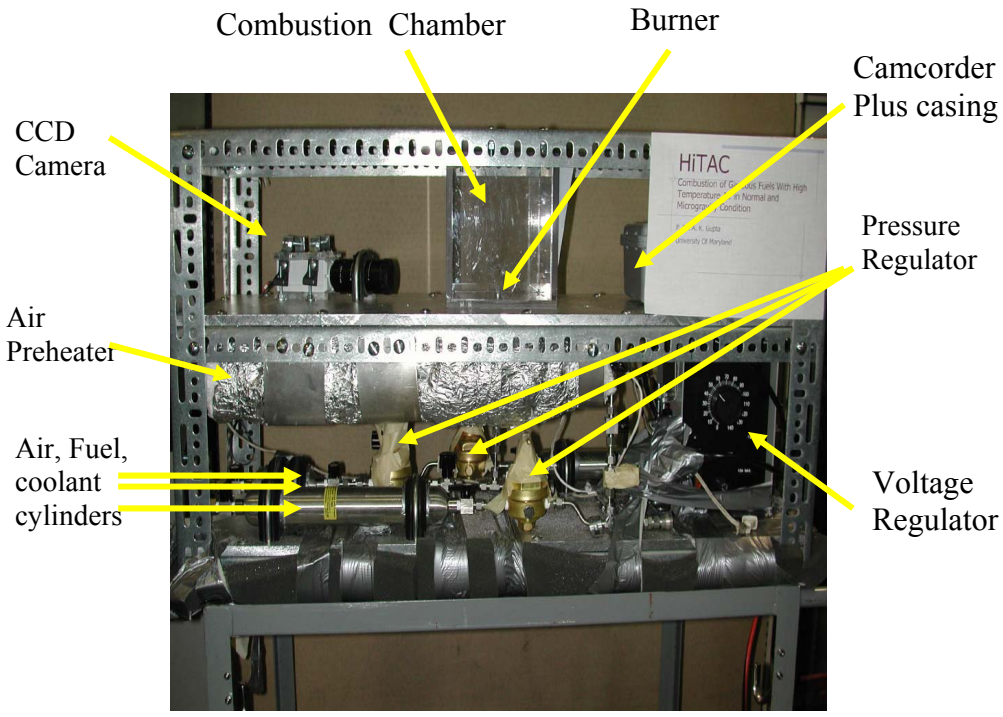

Figure 3.1 A Photograph of the Experimental Facility for Use in 1 Second Drop Tower

3.1.2 Glass Combustion Chamber

Combustion chamber (Figure 3.1) is made of glass with fully optical view. There is a vent at the top of the chamber. Burner is inserted into the chamber from the bottom plate of combustion chamber. The combustion chamber is operated at one atmosphere, so that there is no issue on safe operation of the chamber since it has not been operated at high pressure.

3.1.3 Image and Video Data Acquisition System

The components of the video data acquisition system are CCD camera model CV-S3300, close focus lens, and Canon Elura 2 MC Camcorder. The pictures, which have been taken by CCD camera, are recording in the tape by camcorder. An s-video wire connects the CCD camera to the camcorder. The Canon ELURA 2MC camcorder is adopted for recording the images. It is installed in a well-insulated casing so that there is no disturbances to the tape drive mechanism. The digital tape is used as recording media, and after experiment the data and image can be transferred to computer by Fire Wire PCI Upgrade/Expansion Card and corresponding cable.

3.1.4 Burner

The burner, which is made of Stainless steel, provides a diffusion type flame. A sketch of the burner is shown in Figure 3.2. The fuel was injected from a centrally located 0.686 mm diameter fuel nozzle surrounded by a 12.7 mm diameter combustion air nozzle through which the air was allowed to flow. The combustion air could be preheated when it is passed through preheater in the airline. The fuel jet is cooled throughout the entire length of the fuel passage in the burner so that the surrounding preheated combustion air has no effect on the chemical and thermal properties of the fuel prior to its injection into the surrounding combustion air.

3.1.5 Air Preheater

The main body of preheater is the stainless steel tubing, which houses the ceramic tube and the heating element (hot wire).

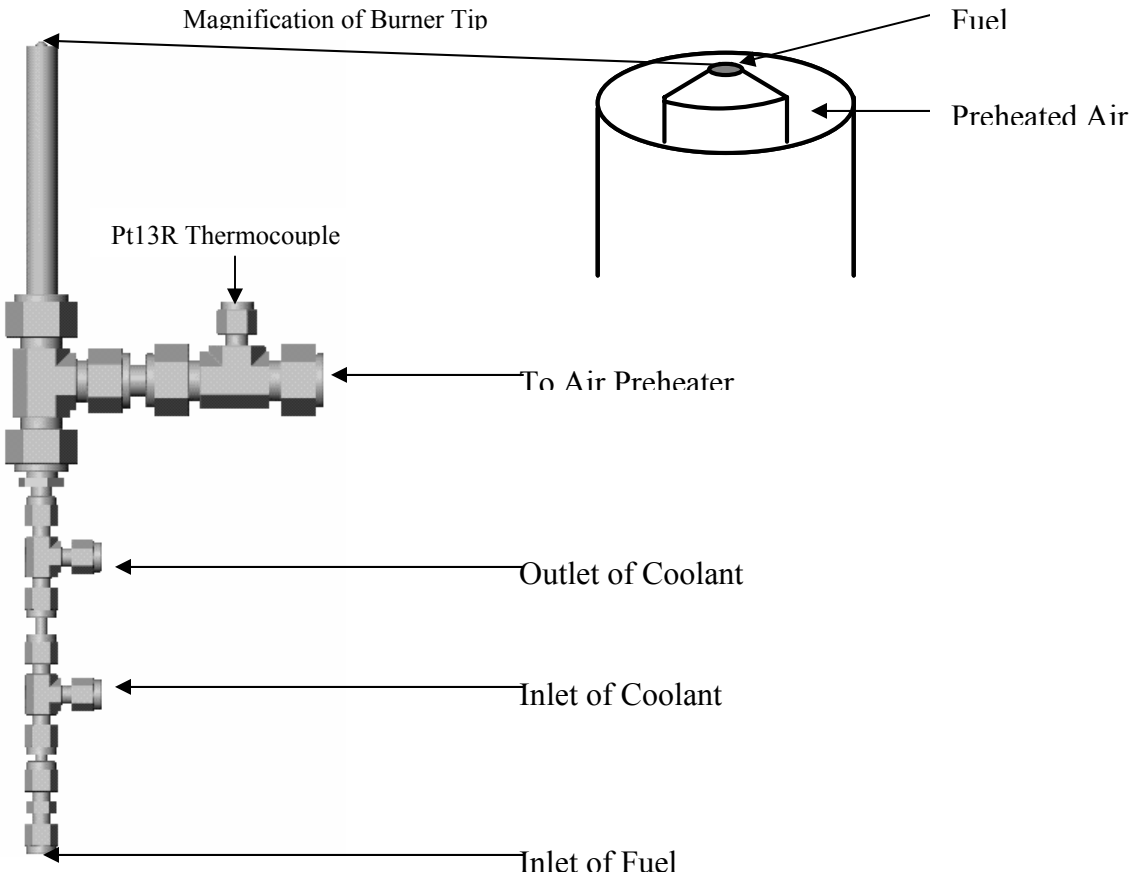

Figure 3.2 Burner

The power supply for heating the air can be varied by a variable converter. The components of the preheater and its section view are shown in Figures 3.3 and 3.4.

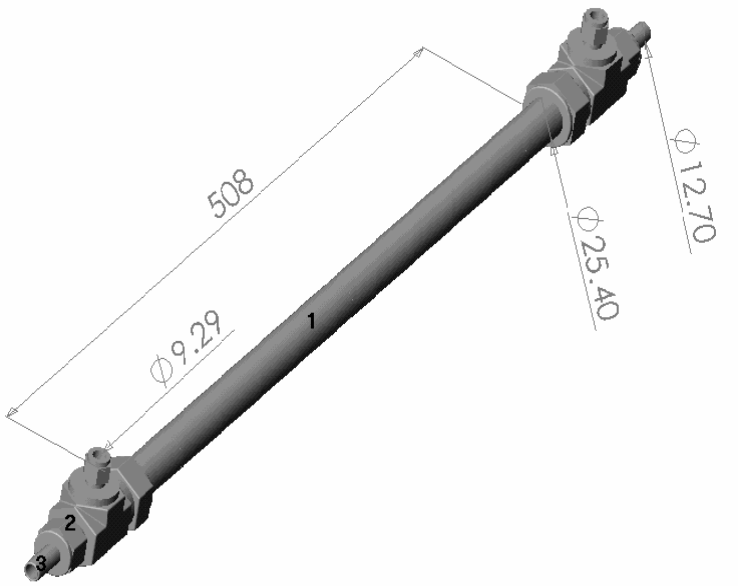

Figure 3.3 View of Air Preheater

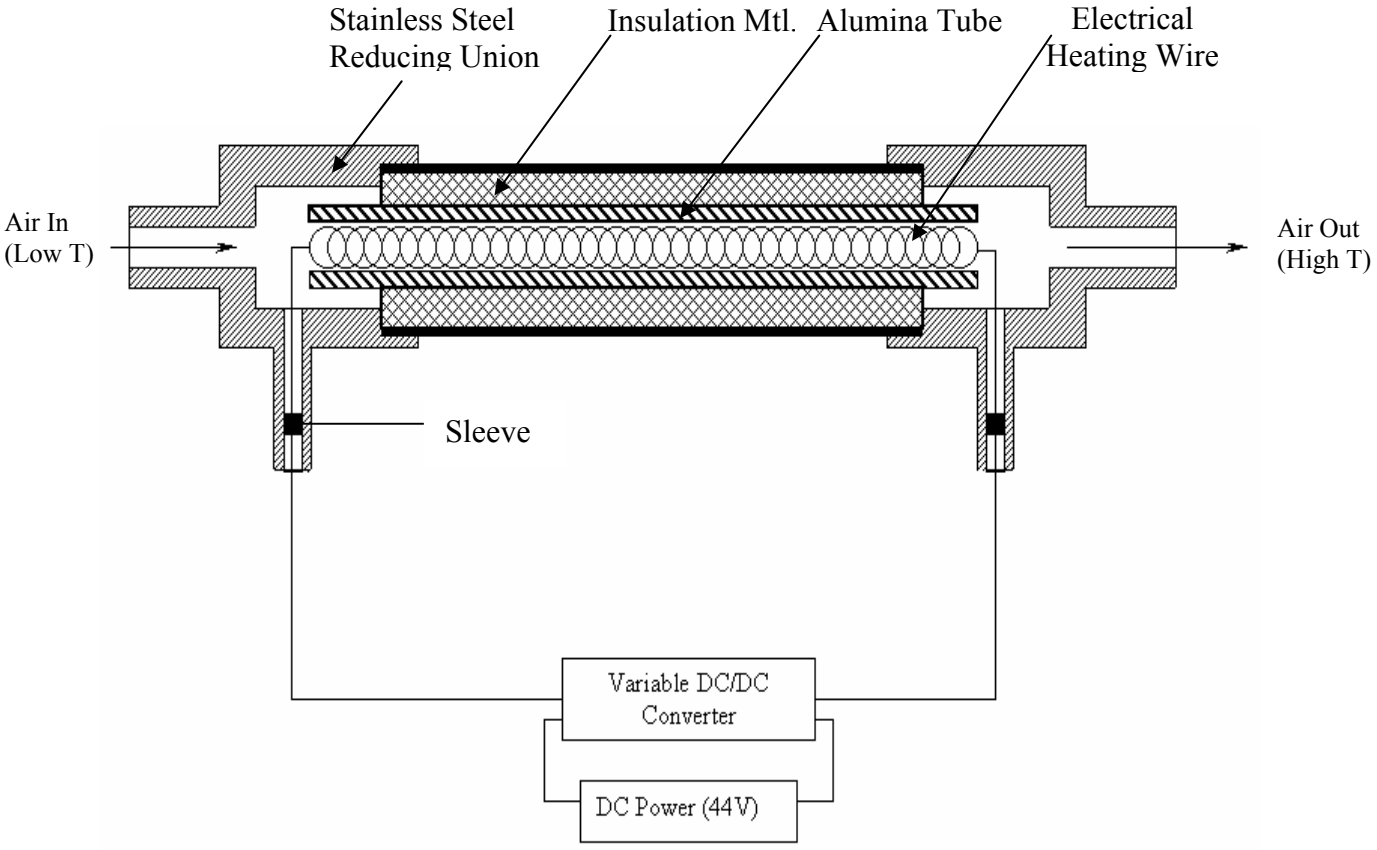

Figure 3.4 Section View of Air Preheater

To control the preheated air temperature, a Watlow Seies 93 temperature controller was used. This temperature controller is a 1/16 DIN microprocessor-based temperature controller. The input can accept J, K, T, N or S thermocouple. The outputs can be dual; the primary output could be heating or cooling while the secondary output could be a control output opposite the primary output (heat or cool), alarm or none.

A mechanical relay is used to open or close the air heating electrical circuit. The preheated combustion air temperature is compared with the arbitrary set point temperature in controller. In case of exceeding the preheated air temperature from set point temperature, a signal is sent to relay to open the circuit. Basically the temperature controller operates based on the results of comparison of temperature set point with the temperature signals, which are sent by thermocouple. Thermocouple measures the output temperature of preheated air.

3.1.6 Experimental Facility Modification for Use in Particle Image Velocimetry

The modified facility consists of a diffusion flame quartz burner, an electrical preheater, a voltage regulator, preheated air temperature controller system, and particle seeder. The purpose of the seeder is to introduce particles into the combustion air flow for PIV diagnostics (see Figure 3.5). The combustion air is preheated using a 5.6-ohm electrical wire at 60 volts AC. The quartz burner is essentially a co-annular burner having a centrally located 0.8 mm diameter fuel nozzle surrounded by a 12.89 mm diameter combustion air flow. In order to trace the motion of the flow, 40-micron glass balloons are introduced into the combustion airflow using a fluidized bed. The

burner and preheater are a single unit in the glass burner design. This ensures a convenient and smooth passage for seeded flow. The maximum combustion air temperature is limited by the softening temperature of the glass microballoons. These balloons become welded to the inner walls of the quartz tube if the preheat temperature exceeds 350 C. The concentration of seed particles entering the flow depends heavily on the amount of seed particles remaining in the seeder. Care must be taken to monitor the amount of seed particles in the seeder in order to obtain uniform seeding concentrations.

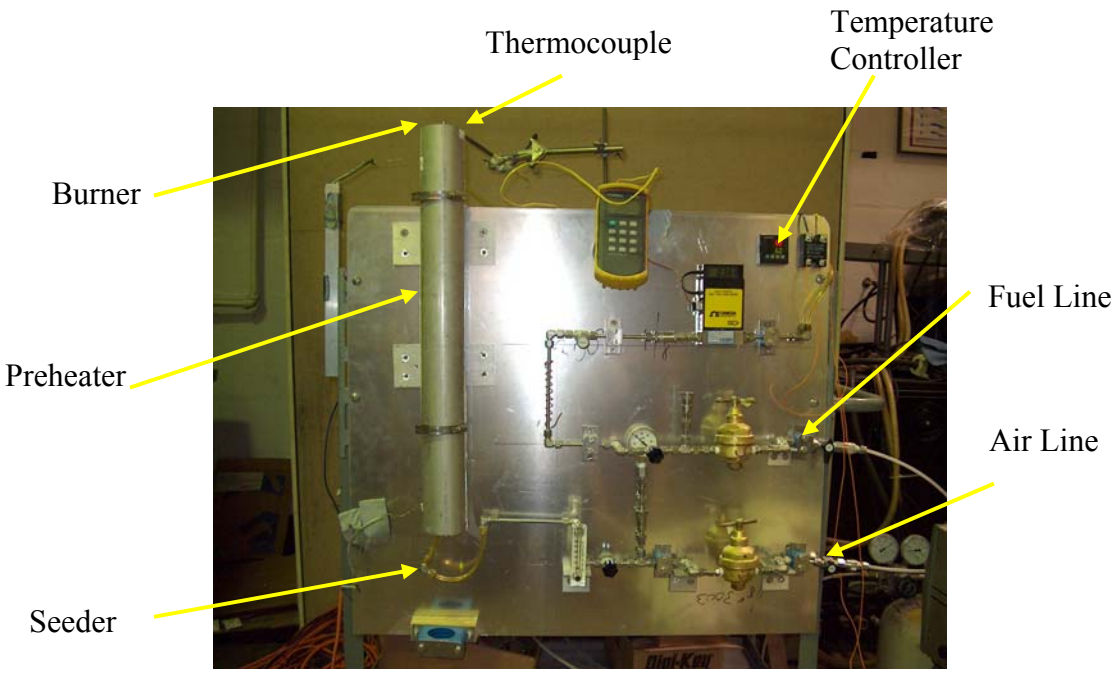

Figure 3.5 A Photograph of the Modified Experimental Facility for Use in PIV Experiments

3.2 Experimental Diagnostics

In this investigation, measurements have been conducted with the goal of providing soma global characteristics as well as some detailed data concerning the effects of preheated combustion air on the laminar coflow diffusion flames flow field, chemistry and dynamics. The specific diagnostics employed are direct flame photography, particle image velocimetry (PIV) and optical emission spectroscopy (OES). In applying optical emission spectroscopy technique, a filtered ICCD camera records two-dimensional images of chemiluminescence from absolute excited state concentration of OH, CH and C2.

3.2.1 Direct Flame Photography

Direct flame photography (see Figure 3.6) is used to provide quantitative information without affecting the combustion flow field or other properties in the flame for normal and low gravity conditions. These informations are the colors, shapes, dimensions, and structures of the diffusion flames. The video data acquisition system includes CCD camera, close focus lens, and Camcorder.

The pictures taken by CCD camera, are recording in the tape. An s-video wire connects the CCD camera to the camcorder. The digital tape is used as recording media, and after experiment the data and images are transferred to computer by Fire Wire PCI Upgrade/Expansion Card and corresponding cable.

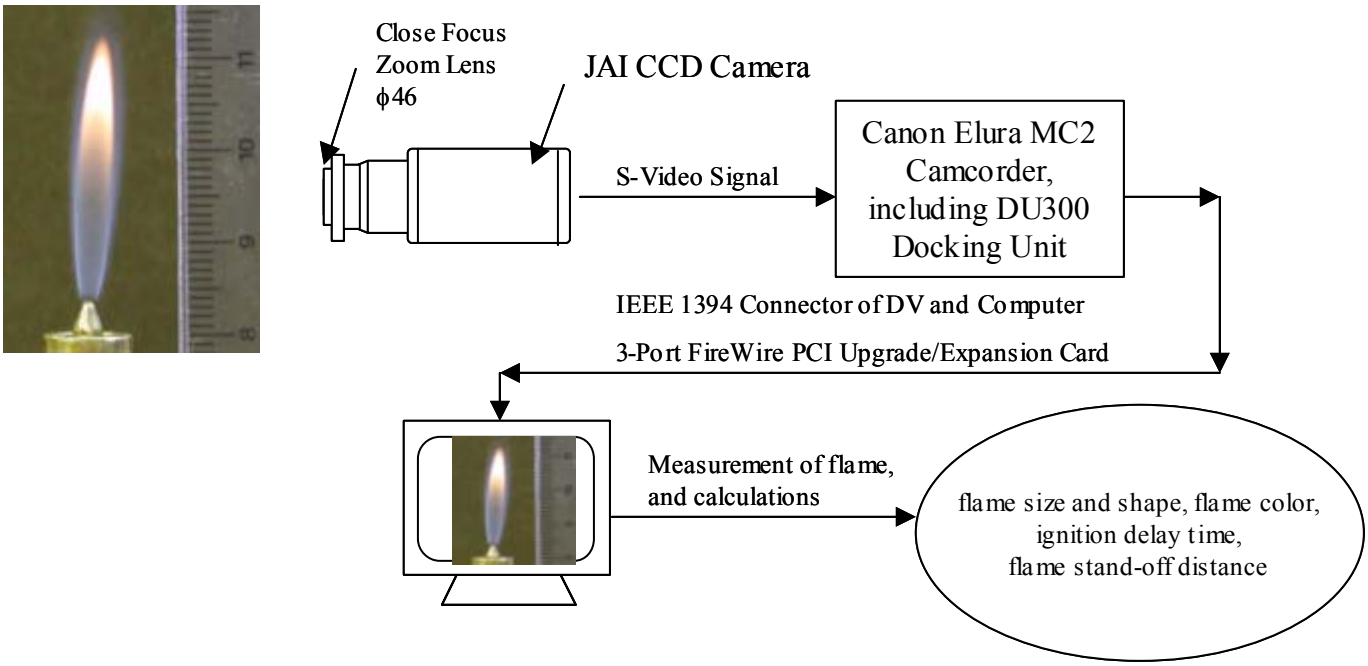

Figure 3.6 Direct Flame Photography

3.2.2 Particle Image Velocimetry (PIV)

In contrast to techniques for the measurement of flow velocities employing probes as pressure tube or hot wires, the PIV techniques being an optical technique works nonintrusively. This allows the application of PIV even in high-speed flows with shocks or in boundary layers close to the wall, where the flow may be distributed by the presence of probes. PIV is a technique, which allows one to record images of large parts of flow fields in a variety of applications in gaseous and liquid media and to extract the velocity information out of these images. This feature is unique to the PIV technique. Except Doppler global velocimetry all other techniques for velocity measurements only allow the measurement of the velocity of the flow at a single point, however in most cases with a high temporal resolution. Instantaneous image

capture and high special resolution at PIV allow the detection of spatial structures even in unsteady flow field [45].

3.2.2.1 Pulsed Light Velocimetry

Pulsed light velocimetry can be classified into two types [46], as illustrated in Figure 3.7. These depends of whether the markers are particles or are molecules mixed with the fluid media that can be made visible by photochromic or fluorescent means.

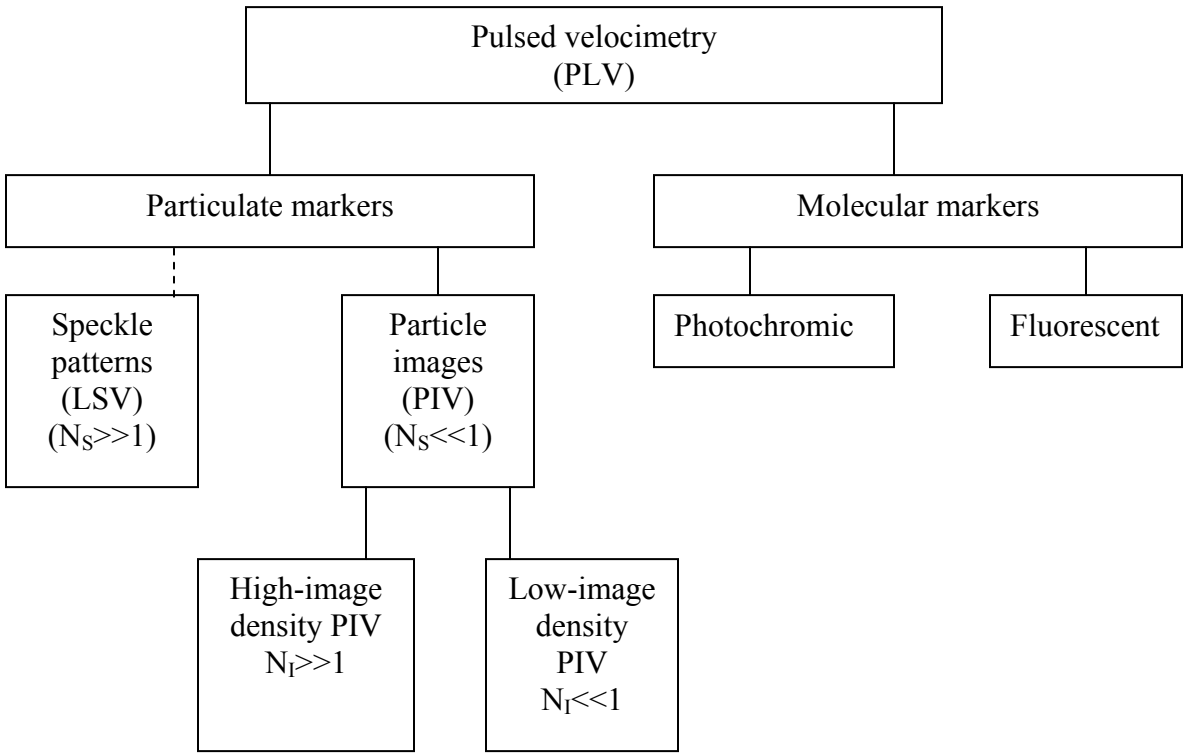

Figure 3.7 Classification of Pulsed Light Velocimetry [47]

Particle methods may be classified further according to what is called their source density, the average number of particles residing in the resolution cell as a given time

$$N_S = C\Delta z_0 \frac{\pi d_i^2}{4M^2} \tag{3.1}$$

where C is the number of particles per unit volume, M is the magnification of the lens, and d_i is the particle image diameter. The latter depends not only on the particle diameter and the lens magnification, but also on the point response function of the lens. The resolution cell is thus the small cylinder formed by the intersection of the circle of diameter d_i / M formed by the projection of the particle image back into the fluid through the light sheet. If the source density is small enough so that images of individual particles can be discerned everywhere in the image plane (i. e., N_S <<1), measuring their displacement over a short time in order to determine the velocity components in the image plane is known as particle image velocimetry (PIV). PIV is now much more commonly used than LSV [46], because in many experiments it is difficult or undesirable to maintain the very high particle concentrations required for LSV.

PIV by itself may be further sub-classified as high image density (HID) or low image density (LID). For HID/PIV there are many particles in an "interrogation cell" at any time, but not enough to cause speckle. An interrogation cell is defined as a sub-region of the recorded field of view over which the post-processing analysis determines the velocity vector. Ruther than attempting to track the motion of all many individual particles in the interrogation cell, for the HID method the displacement of the entire group is determined via a correlation technique. By contrast, for LID/PIV

the particle number density is low enough so that only a few particles are located in the interrogation region at any time, and they are tracked individually to determine the velocity components. LID/PIV is also often called particle-tracking velocimetry (PTV). A measure used to determine which of the PIV modes is present for a given experiment [46] is image density

$$N_I = C\Delta z_0 \frac{\pi d_I^2}{4M^2} \tag{3.2}$$

where d_I is the diameter of an interrogation spot on the image. Projected back through the fluid, it forms a cylindrical cell of diameter d_I / M in the light sheet. $N_I<<1$ corresponds to the low-image-density limit in which the probability of finding more than one particle in the interrogation cell is much less than finding only one particle. At the other extreme, when $N_I>>1$, the probability is high that many particles occupy the interrogation cell at a given time [47].

3.2.2.2 Tracer Particle

PIV is based on the direct determination of the two fundamental dimensions of the velocity: length and time. On the other hand, the technique measures indirectly because it is the particle velocity, which is determined instead of fluid velocity. Therefore, fluid mechanical properties of the particles have to be checked in order to avoid significant discrepancies between fluid and particle motion. A primary source of error is the influence of gravitational forces if the density of the fluid ρ and the tracer particles ρ_p do not match. Even if it can be neglected in many particle situations, we will derive the gravitationally induced velocity U_g from stokes drag law

in order to introduce the particle's behavior under acceleration. Therefore we assume spherical particles in a viscous fluid at a very low Reynolds number. This yields:

$$U_g = d_p^2 \frac{\left(\rho_p - \rho\right)}{18\mu} g \tag{3.3}$$

where g is the acceleration due to gravity, μ the dynamic viscosity of the fluid, and d_p is the diameter of the particle. In analogy to equation 3.3, we can derive an estimate for the velocity lag of a particle in a continuously acceleration fluid:

$$U_S = U_p - U = d_p^2 \frac{\left(\rho_p - \rho\right)}{18\mu} a \tag{3.4}$$

where U_s is velocity lag, U is flow velocity vector and U_p is the particle velocity. The step response of U_p typically follows an exponential law if density of the particle is much greater than the fluid density:

$$U_p(t) = U\left[1 - \exp\left(-\frac{t}{\tau_S}\right)\right] \tag{3.5}$$

with the relaxation time τ_s given by:

$$\tau_s = d_p^2 \frac{\rho_p}{18\mu} \tag{3.6}$$

If the fluid acceleration is not constant or stokes drag does not apply (e. g. at higher flow velocities) the equations of the particle motion become more difficult to solve, and the solution is no longer a simple exponential decay of the velocity. Nevertheless, τ_s remain a convenient measure for the tendency of particles to attain velocity equilibrium with the fluid. From equation (3.4) it can be seen that due to the difference in density between the fluid and the tracer particles, the diameter of the particles should be very small in order to ensure good tracking of the fluid motion. On

the other hand, the particle diameter should not be too small, as light scattering properties have also to be taken into account. Since the obtained particle image intensity and therefore the contrast of the PIV recording is directly proportional to the scattered light power, it is often more effective and economical to increase the image intensity by properly choosing the scattering particles than by increasing the laser power. In general it can be said that the light scattered by small particles is a function of the ratio of the refractive index of the particles to that of the surrounding medium, the particles size, their shape and orientation.

3.2.2.3 Mathematical Background

The accuracy with which the magnitude of the particle displacements in the X-Y image plane

$$\Delta X = U \Delta t M \tag{3.7}$$

$$\Delta Y = V \Delta t M \tag{3.8}$$

can be measured increases with the ratio $\Delta D/d_i$, where U and V are the components of the particle speed in the light sheet focal plane, and $\Delta D = (\Delta X^2+\Delta Y^2)^{1/2}$. Thus, in addition to following the flow better, small particles give greater measurement accuracy. The accuracy with which U and V are determined is greatly affected by the choice of the time interval between pulses Δt, the parameter that is easiest to control in experiments. It should be small enough so that ΔX and ΔY are small compared to the smallest scales to be resolved in the flow, but still large enough to be detected

accurately. In practice, Δt is chosen so that $\Delta D \approx 20$ to 30 times larger than d_i. Laser pulse energies, and film or CCD camera sensitivities is available [48]. Laser pulse durations are typically about 20 ns for airflow (i. e. sharp enough to obtain sharp images even at relatively high speed).

3.2.2.4 Image Shifting

For experiments in which regions of f low reversal occur, there may be a degree of ambiguity in deciding which is the first and which is the second illuminated particle image. To circumvent this problem, technique called image shifting, analogous to frequency shifting in LDV, can be used. Thus, between the two pulses, the image can be shifted a prescribed distance that causes all the displacements to appear to be in one direction only. A sketch of such a shift in the streamwise direction, denoted as ΔX_0, is shown in Figure 3.8.

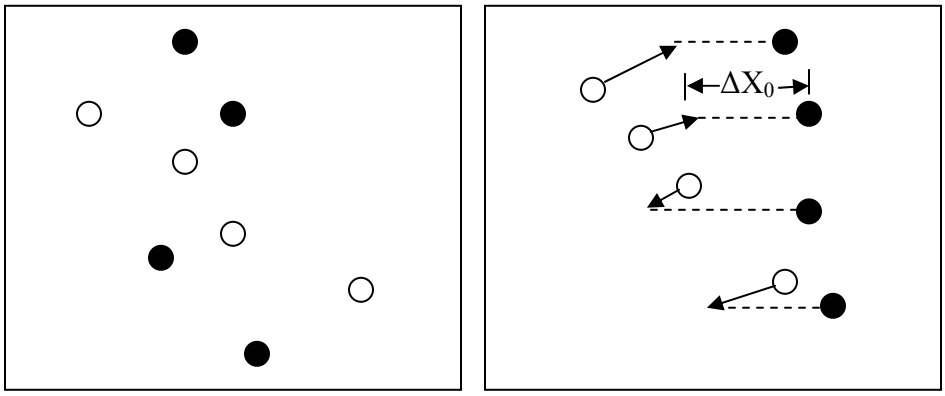

Figure 3.8 Image Shifting to Decide Which is the First and Which is the Second Illuminated Particle Images [49]

For this example, after the images have been analyzed and the velocity components determined, the artificial velocity associated with the shift, $U_S = \Delta X_0/(M \Delta t)$, is subtracted from the streamwise component.

3.2.2.5 Vector Field Operators

In many fluid mechanical applications the velocity information by itself is of secondary interest in the physical description, which is principally due to the lack of simultaneous pressure and density field measurements. In general the pressure, density and velocity fields are required to completely recover all terms in the Navier-Stokes equation:

$$\rho \frac{DU}{Dt} = -\nabla p + \mu \nabla^2 U + F \qquad (3.9)$$

where F represent the contribution of the body forces such as gravity. Clearly, the task of obtaining all of these field quantities simultaneously is unrealistic at present. However, the velocity field obtained by PIV can be used to estimate other fluid mechanically relevant quantities by means of differentiation or integration. Of the differential quantities the vorticity field is of special interest because this quantity, unlike the velocity, is independent of the frame of reference. In particular, if it is resolved temporally, the vorticity field can be much more useful in the study of flow phenomena than the velocity field by itself, especially in high vortical flow phenomena than the velocity field by itself, especially in highly vortical flows such as turbulent boundary layers, wake vortices and complex vortical flows. For incompressible flow the Navier-Stokes equation can actually be written in terms of the vorticity, that is the vorticity equation:

$$\frac{\partial \omega}{\partial t} + U.\nabla \omega = \omega.\nabla U + \nu \nabla^2 \omega \qquad (3.10)$$

which expresses the rate of change of vorticity of a fluid element (for simplicity, F = 0). Although the pressure term has been eliminated from this expression, the estimation of the last term is difficult from actual PIV data. Because of its frequent use in fluid dynamical descriptions the estimation of vorticity from PIV data will serve as an example for the available differentiation scheme given in the following sections.

Integral quantities can also be obtained from the velocity field. The instantaneous velocity field obtained by PIV can also be integrated yielding either single values through path integrals or another field quantity such as the stream function. Analogous to the vorticity field, the circulation, which is obtained through path integration, is also of special interest in the study of vortex dynamics, mainly because it is also independent of the reference frame. Other PIV applications may require the calculation of mass flow rates in a control volume type of analysis.

3.2.2.6 Estimation of Differential Quantities

The terms can actually be calculated from the planar velocity field are determined based on following scheme. Standard PIV data provide only the two components of the three-dimensional vector field while more advanced PIV methods like stereoscopic PIV provide three-component velocity data. Unless several light sheet planes are recorded simultaneously the PIV method can only provide a single plane of velocity data thereby excluding all possibilities of calculating gradients normal to the light sheet. In order to see which differential terms actually can be

calculated, the full velocity gradient tensor or deformation tensor, dU/dX, will be given first:

$$\frac{dU}{dX}=\begin{bmatrix} \frac{\partial U}{\partial X} & \frac{\partial V}{\partial X} & \frac{\partial W}{\partial X} \\ \frac{\partial U}{\partial Y} & \frac{\partial V}{\partial Y} & \frac{\partial W}{\partial Y} \\ \frac{\partial U}{\partial Z} & \frac{\partial V}{\partial Z} & \frac{\partial W}{\partial Z} \end{bmatrix} \tag{3.11}$$

this deformation tensor can be decomposed into a symmetric part an antisymmetric part:

$$\frac{dU}{dX}=\begin{bmatrix} \frac{\partial U}{\partial X} & \frac{1}{2}\left(\frac{\partial V}{\partial X}+\frac{\partial U}{\partial Y}\right) & \frac{1}{2}\left(\frac{\partial W}{\partial X}+\frac{\partial U}{\partial Z}\right) \\ \frac{1}{2}\left(\frac{\partial U}{\partial Y}+\frac{\partial V}{\partial X}\right) & \frac{\partial V}{\partial Y} & \frac{1}{2}\left(\frac{\partial W}{\partial Y}+\frac{\partial V}{\partial Z}\right) \\ \frac{1}{2}\left(\frac{\partial U}{\partial Z}+\frac{\partial W}{\partial X}\right) & \frac{1}{2}\left(\frac{\partial V}{\partial Z}+\frac{\partial W}{\partial Y}\right) & \frac{\partial W}{\partial Z} \end{bmatrix} \tag{3.12}$$

$$+\begin{bmatrix} 0 & \frac{1}{2}\left(\frac{\partial V}{\partial X}-\frac{\partial U}{\partial Y}\right) & \frac{1}{2}\left(\frac{\partial W}{\partial X}-\frac{\partial U}{\partial Z}\right) \\ \frac{1}{2}\left(\frac{\partial U}{\partial Y}-\frac{\partial V}{\partial X}\right) & 0 & \frac{1}{2}\left(\frac{\partial W}{\partial Y}-\frac{\partial V}{\partial Z}\right) \\ \frac{1}{2}\left(\frac{\partial U}{\partial Z}-\frac{\partial W}{\partial X}\right) & \frac{1}{2}\left(\frac{\partial V}{\partial Z}-\frac{\partial W}{\partial Y}\right) & 0 \end{bmatrix}$$

A substitution of the strain and vorticity components yields:

$$\frac{dU}{dX}=\begin{bmatrix} \varepsilon_{XX} & \frac{1}{2}\varepsilon_{XY} & \frac{1}{2}\varepsilon_{XY} \\ \frac{1}{2}\varepsilon_{YX} & \varepsilon_{YY} & \frac{1}{2}\varepsilon_{YZ} \\ \frac{1}{2}\varepsilon_{ZX} & \frac{1}{2}\varepsilon_{ZY} & \varepsilon_{ZZ} \end{bmatrix}+\begin{bmatrix} 0 & \frac{1}{2}\omega_Z & -\frac{1}{2}\omega_Z \\ -\frac{1}{2}\omega_Z & 0 & \frac{1}{2}\omega_Y \\ -\frac{1}{2}\omega_X & \frac{1}{2}\omega_Y & 0 \end{bmatrix} \tag{3.13}$$

thus the symmetric tensor represents the strain tensor with the elongational strain on the diagonal and the shearing strains on the off-diagonal, whereas the antisymmetric part contains only the vorticity components.

Given that standard PIV data provides only the U and V velocity components and that this data can only be differentiated in the X and Y directions, only a few terms of the deformation tensor, dU/dX, can be estimated with PIV:

$$\omega_Z=\frac{\partial V}{\partial X}-\frac{\partial U}{\partial Y} \tag{3.14}$$

$$\varepsilon_{XY}=\frac{\partial U}{\partial Y}+\frac{\partial V}{\partial X} \tag{3.15}$$

$$\eta=\varepsilon_{XX}+\varepsilon_{YY}=\frac{\partial U}{\partial X}+\frac{\partial V}{\partial Y} \tag{3.16}$$

therefore only the vorticity component normal to the light sheet can be determined, along with the in-plane shearing and extensional strains. In this regard it is interesting to note that the additional availability of the third velocity component, W, by more advanced PIV methods, does not yield any additional strains or vorticity components.

Assuming incompressibility, the sum of the in-plane extensional strains in equation (3.16) can be used to estimate the out-of-plane strain ε_{ZZ}:

$$\varepsilon_{ZZ}=\frac{\partial W}{\partial Z}=-\frac{\partial U}{\partial X}-\frac{\partial V}{\partial Y}=-\eta \tag{3.17}$$

however the quantity η only indicates the presence of out-of-plane flow; it does not recover the out-of-plane velocity.

3.2.2.7 Particle Image Velocimetry Experimental Set Up

Particle image velocimetry (PIV) has been used to determine the features associated with the flow field under different conditions. A typical simple PIV image has shown in Figure 3.9. A control module was used to operate the camera for image acquisitions. The system used for the particular measurements was an Integrated Design Tools (IDT) PIV system for 3-D data acquisition. IDT-1000 and an IDT-2000 control module were used to operate the camera for image acquisition.

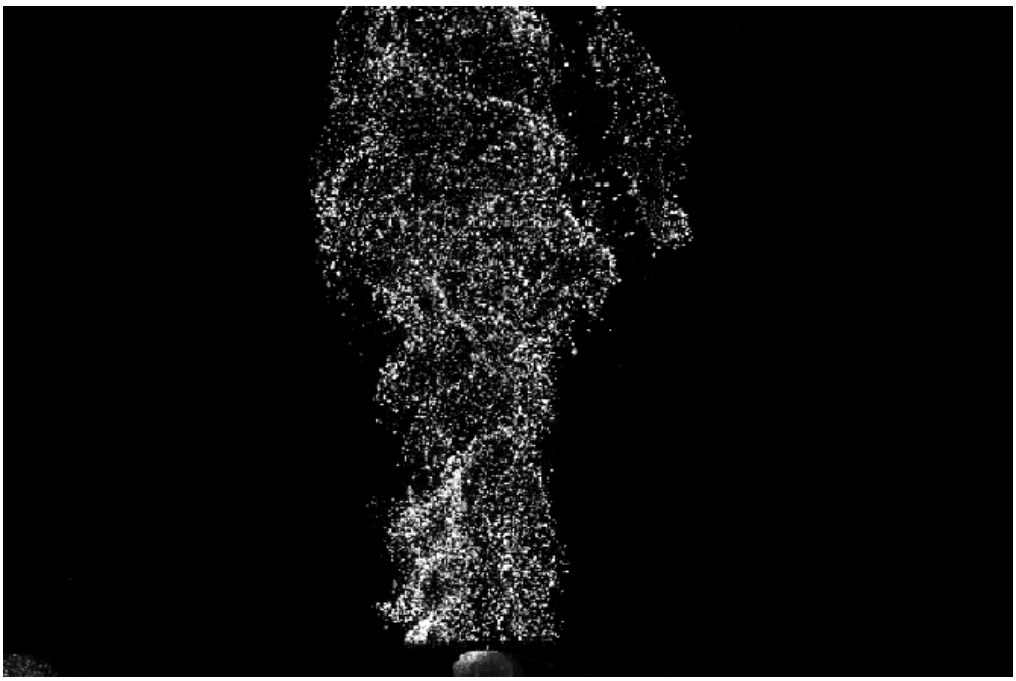

Figure 3.9 A Typical Sample PIV Image

A SoloPIV Nd: YAG laser was used as the light source for illuminating the test section. Gupta et al [50] provide details on the development of the system for use in combustion studies that often have high background flame radiation. A CCD camera with an active pixel array of 1360 x 1024 was used. The CCD camera has a pixel size of 4.65 μm x 4.65 μm and a sensor area of 7.6 mm x 6.2 mm (sharpVISION^{TM} 1400-DE, model Sony ICX205AL CCD). The camera was equipped with mechanical shutter and a narrow band pass filter (0.87nm) at center wavelength of 532nm to allow for maximum transmission of signal. The system runs with proVISION^{TM} software. In order to trace the motion of flow, 40-micron glass balloons particles were introduced into the combustion airflow. A glass particle seeder is used to seed air streams sufficiently using fluidized bed. The dispersion of small size particles uniformly into the flow is a challenge so that care must be exercised to seed the particles into the flow.

A thin laser sheet beam was used to illuminate the seeded particles in the flow. In the experiments the laser frequency was set at 5 Hz, which was also synchronized with the camera frequency. The particles present in the flow scattered the incident laser sheet light. The camera, placed normal to the laser sheet beam, was used to detect the particle in the flow. Two images acquired were the first initial position of the seeded particles and second image position of the particles after a known time interval. The measured area in the test section was 57 x 85 mm (x * y). when a large number of images pairs had been acquired, the images were then processed with the proVISION^{TM} software to determine the mean motion of the flow field. Tecplot^{TM} software was used to present the graphical data.

3.2.2.8 Error in the Particle Image Velocimetry Technique

The error in the PIV results can be divided into the generic error originating from the experiment itself, such as particle lag or thermophoresis, and the errors from the image-processing procedure, especially for digital PIV, such as the sub-pixel-accuracy issue. PIV methods measure the Lagrangian velocities of particles and therefore, are based upon the assumption that the particles follow the surrounding fluid motion. According to the analysis of the Raffel et al. [45], the relaxation time of the particle to step change in the fluid velocity is given in equation (3.6). If the relaxation time is computed assuming a particle size of 40 μm, a particle density of 500 kg/m^3, and a temperatures of 1700 K, it is ~192 μs. The smallest time-scale of the current experimental system obtained is 5 ms. the centerline nozzle exit velocity is 1 m/sec, and the spatial resolution of the experimental system is 5 mm. The calculated relaxation times illustrate adequate fast particle response to gas velocity changes. Therefore, the error from the particle lag is not significant for the current experimental solution. A cross-correlation function is used to process the captured particle images. The interrogation window size is 24 x 24 pixels with a 50% overlap in each direction. The resulting spatial resolution is approximately 5 x 5 mm.

3.2.3 Optical Emission Spectroscopy

3.2.3.1 Optical Emission Spectroscopy Technique

The important difference between combustion and chemical reactions is it's visible flame that is the emission of lights. Therefore the investigations of the quality and quantity of light emitted by flame will form an important role of the study of

combustion process. The great advances in the knowledge of the structure of molecular spectra, mostly made in the decade between 1920 and 1930, enabled us to assign most of the bands found in flame spectra to define emitting species, especially to free radicals such as OH, CH, C_2, and HCO whose presence in combustion process, or even whose existence, had been unsuspected before these advances in molecular spectroscopy. One of the main objects of the study of flame spectra, both in emission and in absorption, has therefore been to identify the intermediate chemical species taking part in the reaction. Optical spectroscopy is one of the best methods for detecting many of the simpler free radicals and there is the great advantage that spectroscopic studies do not interfere with the flame processes [51]. By combination of optical spectroscopy and other evidence like flow field through Particle image velocity technique, the complexities of combustion process can be unraveled.

3.2.3.2 Background

Kitagawa and co-worker [52] and Ishiguro and co-workers [53] studied the effect of preheated air on the inverse concentric diffusion flame. They obtained spectrally and temporally resolved images of flames using a spectral video camera that incorporated a monochromator and high speed UV video camera. The spatial distribution of flame temperature was determined from the conventional two-line method, using C2 vibrational bands. Konishi and co-workers [54] also applied this technique to study the highly preheated flame generated by the regenerative test facility, designed and fabricated by Nippon Furnace Koygo (NFK). They obtained the emission results of the intensity level of OH, CH, and C_2 radicals in the flame with

highly preheated air. The distribution of the inside flame temperature measured from the ratio of the emission intensities. Ghaderi and Gupta [55] used this technique to obtain the temperature distribution inside the coflow diffusion flame in presence of high temperature combustion air.

Han and Mungal [56] explained different views in interpreting the CH distribution in a diffusion flame. They showed that CH, OH and HCO are useful indicators of the reaction zone of a flame and the CH distribution was considered as the flame surface in their study. They noticed OH stays closer to the oxidizer side compared to the other species (see Figure 3.10). Donbar et al. [57] reported similar results for their diluted methane-air diffusion flame. The temperature profile in Figure 3.11 shows that peaks of CH and HCO correspond well with the peak of the temperature profile. Furthermore, Watson et al. [58] performed simulations CH and OH PLIF, and confirmed that CH exists when the reaction is sustained, or the OH exists, even though the concentration can be significantly reduced.

3.2.3.3 Vibrational Temperature of C_2 Emission

The spatial distribution of vibrational temperature as measured from the distribution of C_2 species from within the flames is determined by comparing the emission intensities at two vibrational bands. A typical spectrum of C_2 emission bands (Swan band) observed from a propane-air flame is shown in Figure 3.12 In this figure, two major peaks centered around 470 nm and 515 nm can be observed. The integrated intensity at these two bands is denoted as S_1 and S_2, respectively.

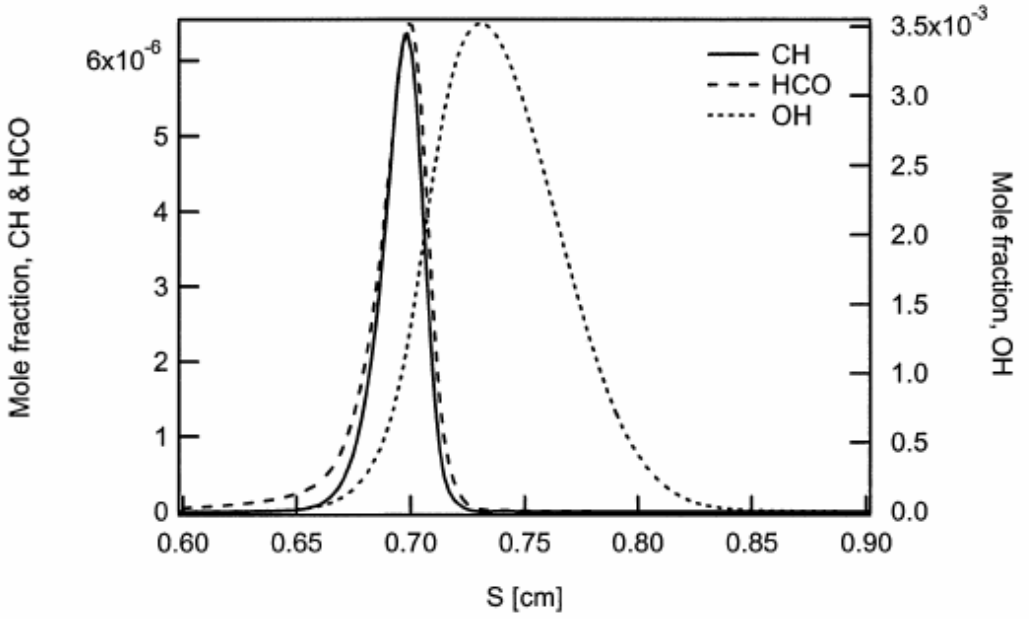

Figure 3.10 Spatial Representation of Flame Zone Markers (OH, CH, HCO) [56]

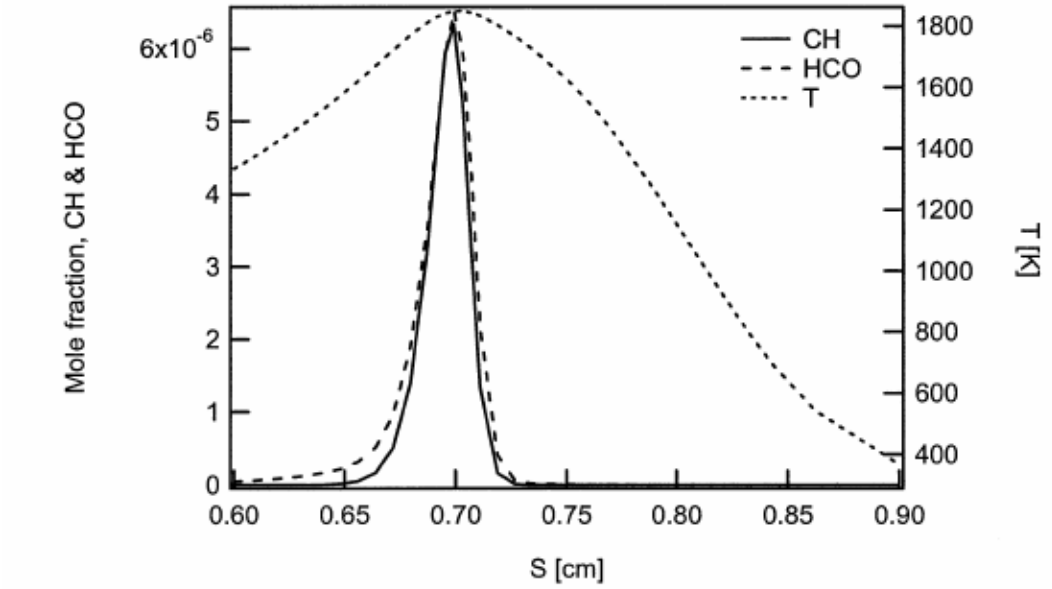

Figure 3.11 Spatial Profile for an Opposed-Flow Diffusion Flame, Between a Fuel (C_2H_2) and Air, Computed by the OPPDIF Code [56]

The ratio of the peak intensity at these two wavelengths is a function of the local gas temperature. The only assumption made here is that the two wavelengths are close to each other, so that the emissivity of the gas does not differ significantly at these two wavelengths.

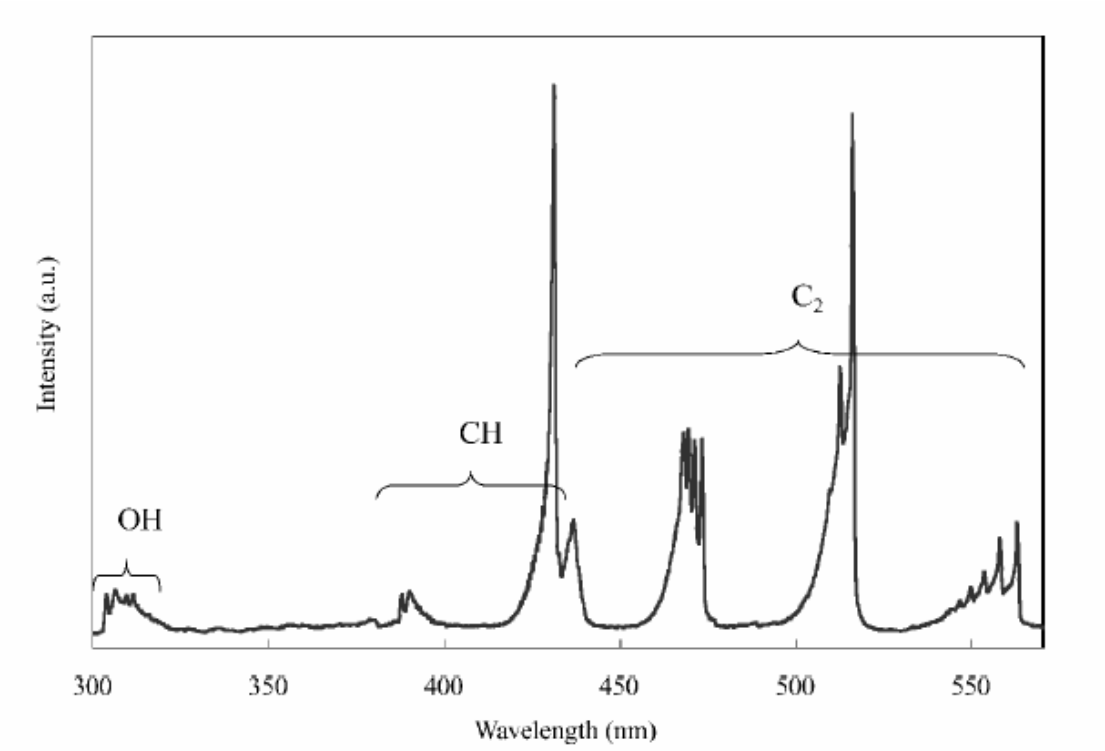

Figure 3.12 Typical Spectrum of Propane-Air Flame [53]

This principle is used in the two color optical pyrometry to determine the flame temperature. It is to be noted that the difference in wavelength between the peak at S_1 and S_2 results from the difference in transition between the vibrational levels. In general, the emission intensity, I , of a component line is given by [53].

$$I = h\nu AN^* \tag{3.18}$$

where h is Plank's constant, ν is the frequency, A is Einstein's coefficient for spontaneous emission, and N^* is population in the exited state. In this study, band-

pass filters were used to isolate the band emission. The band emission intensity, S, measured with these filters can be described by the following expression that is based on the Boltzman distribution law

$$S = \sum_i h\nu_i A_i N_i^* \tag{3.19}$$

The population in an excited state, N^*, is expressed as

$$N^* = N_{total}\, g \exp(-E^*/kT)/Q(T) \tag{3.20}$$

Where g is the degeneracy in the excited state, E^* is the excitation energy, k is Boltzman's constant, N_{total} is the total number of species, T is the excitation temperature, and Q(T) is the partition function. The ratio of emission intensity from different transitions (i and j) depends only on the temperature, since h, g, A, and k are constant, and N_{total} and Q(T) are omitted as seen from the following equation:

$$\frac{S_1}{S_2} = \frac{\sum_i \nu_i A_i \exp(-E_i/kT)}{\sum_i \nu_j A_j \exp(-E_j/kT)} \tag{3.21}$$

The vibrational energy for the vibrational quantum number $\nu', E_{\nu'}$ is given by the following [58]

$$E_{\nu'} = \frac{1}{2}h\nu_0\left[\left(\nu' + \frac{1}{2}\right) - \chi_c\left(\nu' + \frac{1}{2}\right)^2\right] \tag{3.22}$$

Where h is Plank's constant, ν_0 the fundamental vibration quantum number, and χ_c the anharmonic constant. A in equation (3.21) is calculated as the ratio of $A_{\nu',\nu''}$ to $A_{0,0}$, [55].

The temperature calculated from Equation (3.21) using the ratio of C_2 peaks shows the vibrational temperature this temperature is not consistent with the more

traditional temperature obtained from a thermocouple. Likely causes include the overpopulation of the higher vibrational levels on the excited electronic state due to the excess energy generated through chemical reactions, as well as the long vibrational relaxation time. A calibration is necessary to provide a relationship between the temperature determined from the ratio of the C_2 peaks and that measured with a thermocouple.

3.2.3.4 Abel Inversion

To estimate the three-dimensional density distribution of C_2 species and other species in the flame, the Abel transform technique is used. Abel transformation gives the projection of a two-dimensional distribution with circular symmetry (Figure 3.13). A source with a cylindrically symmetric distribution *F(r)*, as shown in Figure 3.13, is projected onto the screen. The projection profile *P(y)* is given by

$$P(y) = 2\int_0^Z F(r).dz \tag{3.23}$$

Where *F(r).dz* is the part of the source located at a radial distance *r* from the axis. In Equation (3.23) the integral is taken along a strip at constant *z*, and the variables have the relationship $y^2 + z^2 = r^2$, $Z^2 = R^2 - y^2$, and *R* is the radius beyond which *F(r)* is zero. Hence, the equation can be written as

$$P(y) = 2\int_y^R \frac{F(r).r.dr}{\sqrt{r^2 - y^2}} = 2\int_y^\infty \frac{F(r).r.dr}{\sqrt{r^2 - y^2}} \tag{3.24}$$

Equation (3.24) is one form of Abel's integral equation. Then the Abel analytic inversion of the projection *P(y)* to the source *F(r)* is given by [60].

$$F(r) = -\frac{1}{\pi}.\int_{r}^{\infty} \frac{1}{\sqrt{y^2 - r^2}} \frac{dP(y)}{dy}.dy \qquad (3.25)$$

The data *P(y)* is obtained as a set of numbers rather than as an analytical function. The inversion integral is difficult to evaluate for discrete data because the derivative of *P(y)* is required and this is subject to large errors when the data is noisy. The noise on the data is amplified, and the integral diverges at $y = r$. Since there is a large data array (320×320), on which this inversion integral is needed to perform an efficient numerical algorithm is required. An algorithm introduced by Cameron J. Dasch [60] has been chosen.

This Abel inversion technique is not restricted to a specific source distribution. It assumes that the line of sight integrated projection data is taken at equally spaced intervals Δy. A linear operator can represent the inversion integral. Data $P(y_j)$ at spacing Δy can be inverted to give the source distribution $F(r_i)$ by

$$F(r_i) = \frac{1}{\Delta x} \sum_{j=0}^{\infty} D_{ij} P(y_j) \qquad (3.26)$$

Where $y_i = i\Delta y$ is the distance from the center of the object. The linear operator coefficient D_{ij} is independent of the data spacing Δy. Once the D_{ij} coefficients are calculated, they can be applied to any form of the projection data.

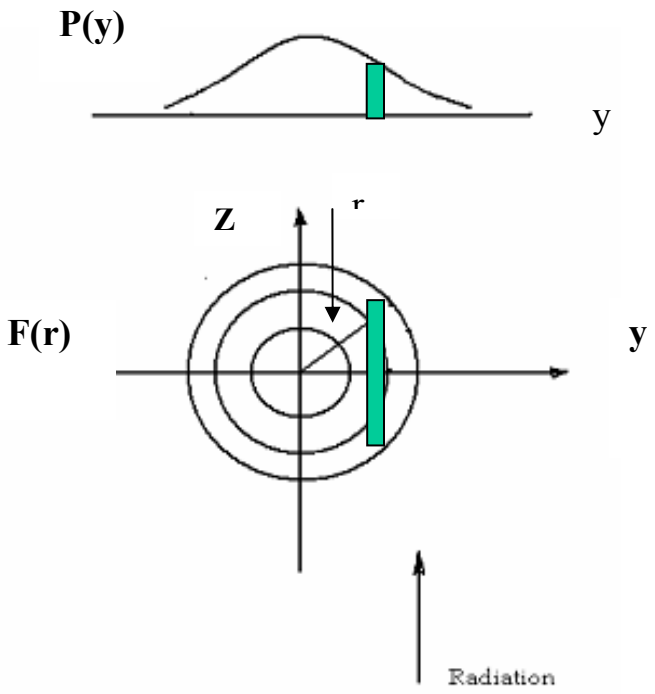

Figure 3.13 A Schematic Diagram of the Abel Transformation and Inversion Technique

3.2.3.5 Optical Emission Spectroscopy Experimental Set Up

Data has been obtained on the spatial distribution of emission intensity from selected radicals. The diagnostics used included an ICCD (image Intensified Charge Coupled Device) (see Figure 3.14). In ICCD the image intensifier detects and amplifies the light, and the CCD is used for readout. The ICCD equipped with proximity-focused microchannel plate (MCP) image intensifier fiber-optically coupled to the CCD array. The proximity–focused MCP has PMT-like UV-NIR response, linear geometric accuracy and can be gated in less than 5 nanosec with an

exceptionally high on/off shutter ratio. A Peltier effect thermoelectric cooler is used to cool the camera. Water is used to carry away the heat generated by the thermoelectric cooler. The detector is being cooled using nitrogen.

The ICCD camera fitted with appropriate narrow band filter, is used to record the emission intensity for a given species of interest. The light signal, after passing through an interference filter, is detected by ICCD camera. Three interference filters are used to detect OH (306 nm), CH (430 nm), C_2 (470 nm) and C_2 (515 nm). Spontaneous emission radicals have been measured over very narrow wavelength (10 nm) bands. These chemical species are amongst the important radicals that provide a key role during the combustion process. The two C_2 bands were used to calculate the viberational temperature. WinView software was used to determine the spatial intensity distribution of these radicals. The ICCD camera is operated in shutter mode, which allows for exposure times of milliseconds or longer. The UV Nikkon lens used with the ICCD camera is operated at an aperture of 11 for all data.

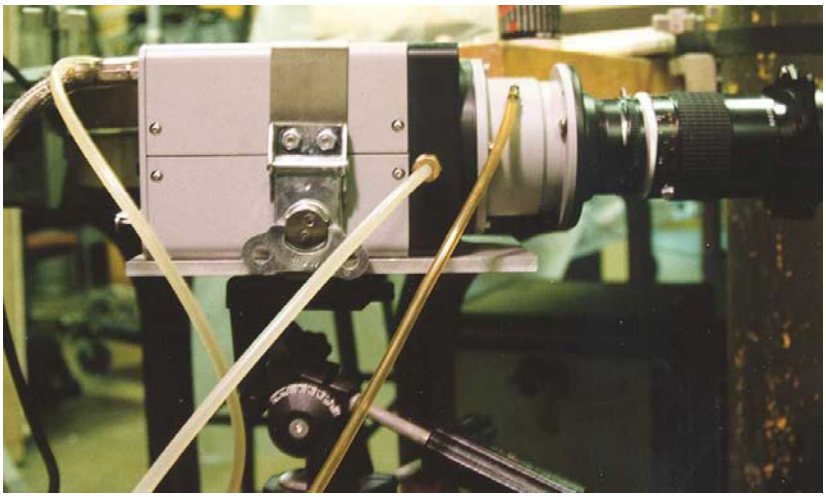

Figure 3.14 ICCD (Image Intensified Charge Coupled Device)

3.3 Experimental Method

3.3.1 Experiments Under Low Gravity Conditions

The characteristics of gaseous diffusion flames have been obtained using preheated temperature combustion air under microgravity. The experiments were conducted using a 1 sec drop tower facility. The time resolved flame images under free fall microgravity conditions were obtained from the video images obtained. The tests were conducted using propane as the fuel at 700^{o}C and 900^{o}C combustion air. The experimental burner consisted of a 0.686 mm diameter fuel jet that was centrally located in a 12.7 mm diameter air jet. The combustion air in the outer jet could be maintained at any temperature, up to 1000^{o}C using electrical heating. The fuel jet exit Reynolds number was 50. The experiment test rig consisted of burner, voltage regulator, electrical air preheater, combustion chamber, color CCD camera and digital camcorder, and gas cylinders for fuel, combustion air and burner cooling. The flame images were captured using a CCD camera in the emission mode at a framing rate of 30 frames per second and then recorded onto a digital camcorder.

Five sets of experiments were conducted under microgravity conditions at normal pressure and normal oxygen concentration air using propane as the fuel at a flow rate 0.02 SCFH. The flame photographs, recorded with the color CCD camera and camcorder, were analyzed to determine the flame shape (length and width) and color. The change in gravity with time during the drop was calculated by balancing the force on the entire drop package (i.e., drag and gravity = mass x acceleration). The results are given in Figure 3.15. The flow rates of fuel and air at different experimental conditions of temperature examined are shown in Table 3.1.

Table 3.1 The Experimental Cases Under Low Gravity Conditions

Preheated Air Temperature K	Fuel Jet Gas	Fuel Flow Rate cc/min	Preheated Air Flow rate (SCFH)
973	Propane	7.8	0.2
1073	Propane	7.8	0.2

3.3.2 PIV Experiments Under Normal Gravity Conditions

A schematic diagram of the experimental apparatus used is shown in Figure 3.16. The dynamics of flow associated with preheated combustion air temperature condition, such as, mean and rms velocity, strain rate and vorticity were obtained in 2-D using Particle Image Velocimetry (PIV) diagnostics. The facility consists of a diffusion flame quartz burner, an electrical preheater, a voltage regulator, preheated air temperature controller system, and particle seeder into the combustion air flow for PIV diagnostics.

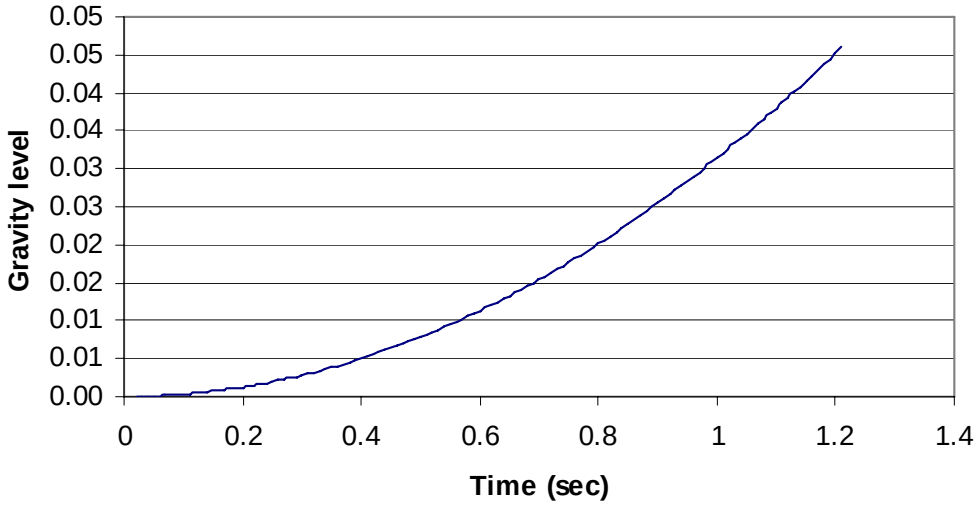

Figure 3.15 Calculated Gravity Level from the Time of Release of the Drop Package

The combustion air was preheated to 353 K using a 5.6-ohm electrical wire at 60 volts AC. The quartz burner was essentially a co-annular burner having a centrally located 0.8 mm diameter fuel nozzle surrounded by a 12.89 mm diameter combustion air flow.

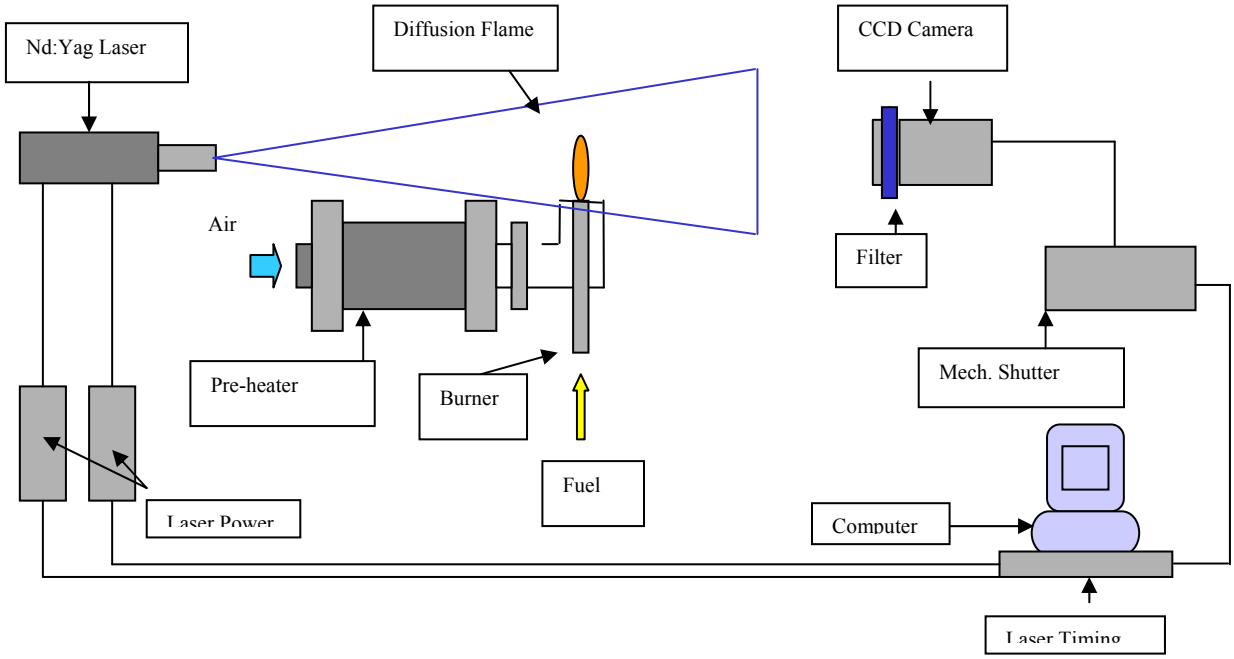

Figure 3.16 Schematic Diagram of the Experimental Apparatus Used in PIV Experiments

The flow rates of fuel and air at different experimental conditions of temperature examined are shown in Table 3.2. The overall equivalence ratio, ϕ, was 0.523. Normal oxygen concentration air (21% by volume) was used in all the experiments reported here. The momentum flux ratio of the preheated combustion air jet to fuel jet between various cases was maintained constant, thus providing similarity in mixing between the various fuel and air flow conditions.

The ratio of preheated combustion air momentum to fuel jet momentum was 4 and this ratio was held constant during tests. The fuel flow rate was 79 ml/min, the velocity of fuel flow at the burner tip was 0.8 m/s. The flame length with normal temperature air with aforementioned flow rate was 32 mm. Data acquisitions were conducted from 250 images pairs of the flow field, from which mean and turbulence characteristics of the flow were determined.

The measurements were carried out under both non-burning (no flame) and burning (with flame) conditions using normal air at normal temperature and preheated air temperatures up to 353 K (80^{o}C). The measurements were performed with a fixed gas jet flow rate in a fixed coflow air velocity. The momentum flux ratio between the gas jet and coflow air jet was maintained constant, thus providing similarity in mixing between the fuel and air for different cases.

Table 3.2 The Experimental Cases Under Normal Gravity Conditions

Preheated Air Temperature (K)	Fuel Jet Gas	Fuel Flow Rate cc/min	Preheated Air Flow Rate (SCFH)
298	Propane	79	5
338	Propane	79	4.8
353	Propane	79	4.7

3.3.3 Optical Emission Spectroscopy Experiments

A schematic diagram of the experimental apparatus used is shown in Figure 3.17. The facility consists of an electrical preheater, a voltage regulator, a diffusion flame burner, gas cylinders for fuel combustion air and burner cooling gases. The

combustion air was preheated to high temperature using a 5-ohm electrical wire at 80 volts. The fuel was injected from a 0.686 mm diameter nozzle that was centrally located in a 12.7 mm diameter air tube, through which the combustion air was allowed to flow. In this study the oxygen concentration in air was regulated at 21% (which provide the equivalence ratio of $\phi = 0.312$). The momentum flux ratio of the preheated combustion air jet versus fuel jet was maintained constant, thus providing similarity in the mixing between the fuel and air under different test conditions. The ratio of preheated combustion air momentum to fuel jet momentum was 5 and during the preheating process this ratio was held constant.

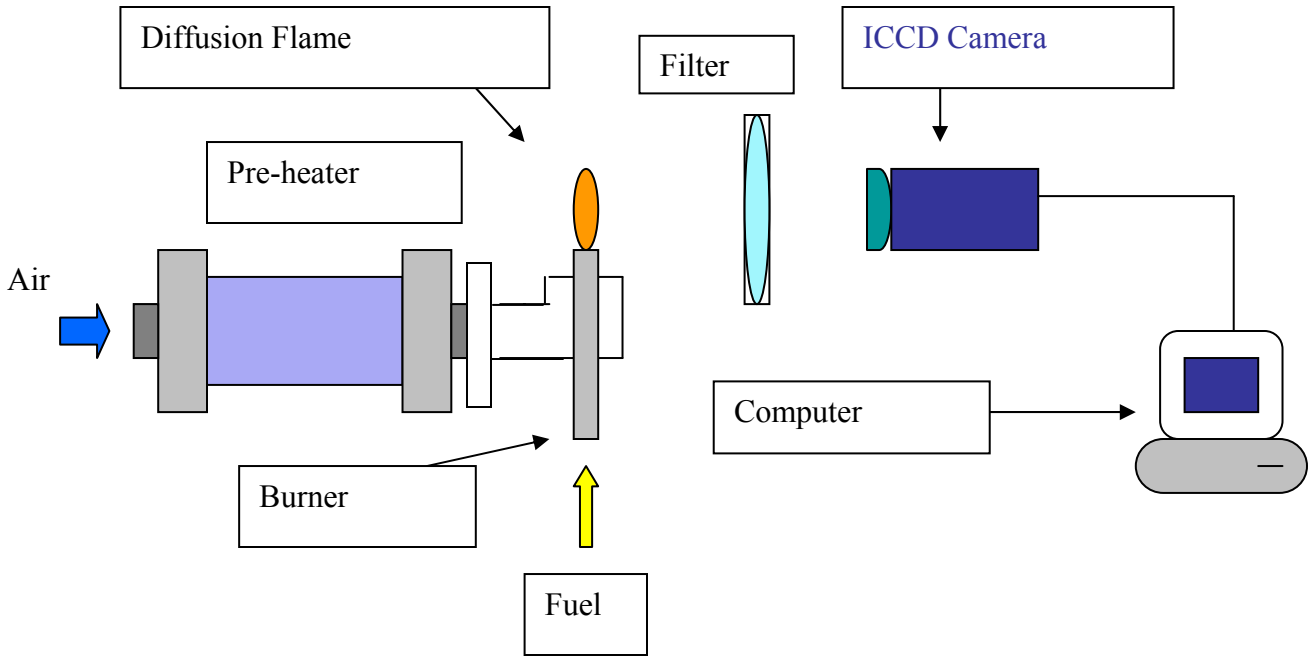

Figure 3.17 Schematic of Optical Emission Spectroscopy Experiments Test Facility

The air and fuel flow rate and velocity at different temperature are shown in Table 3.3. The fuel flow rate was 170 cc/min, and the flame length with normal temperature air with aforementioned flow rate was 32 mm. The ICCD camera, fitted with appropriate narrow band filters**,** was used to record the emission intensity for a given species of interest. The light signal, after passing through an interference filter, was detected by ICCD camera. Three interference filters have been used to detect OH (306 nm), CH (430 nm), C_2 (470 nm) and C_2 (515 nm). Spontaneous emission radicals have been measured over very narrow wavelength (10 nm) bands.

Table 3.3 The Experimental Cases Under Normal Gravity Conditions

Preheated air Temperature (C)	Preheated air Temperature (K)	Preheated air Velocity (m/s)	Preheated air Flow rate (SCFH)
25	298	1.96	17.965
77	350	1.8	16.567
127	400	1.69	15.5
227	500	1.51	13.86
277	550	1.44	13.21
377	650	1.326	12.155
527	800	1.196	10.96

4 Results and Discussion

4.1 Introduction

Measurements and analysis of the effect of preheated combustion air on the structure and shapes of laminar coflow diffusion flames in this study have resulted in significant insight into the behavior of diffusion flames due to preheated combustion air. Direct flame photography, particle image velocimetry (PIV) and optical emission spectroscopy diagnostics were applied to take measurements of laminar coflow diffusion flames. This was followed by the application of the normal and preheated combustion air under normal and low gravity conditions. The measurements agree reasonably well with other studies, which will be discussed in detail below; however, comparison is limited due to the deficit in available data for preheated combustion air laminar coflow diffusion flames. The detailed measurements obtained in these experiments provide new insights into general preheated combustion air flame characteristics and validate some previous modeling. In fact, developing an understanding of the mechanisms behind the effects of combustion air preheating on diffusion flame characteristics is a critical issue in the development of cost-effective high efficiency and low emissions combustors.

4.2 Preheating and Gravity Effects

Measurements and analysis of laminar coflow diffusion flames were conducted to gain a better understanding of their behavior in the presence of preheated combustion air and low gravity environment. Laminar coflow diffusion

flames were examined under four experimental conditions: normal-temperature/normal-gravity (case I), preheated-temperature/normal-gravity (case II), normal-temperature/low-gravity (case III), and preheated-temperature/low-gravity (case IV) (see Table 4.1). Comparisons between these four cases yield significant insights.

Table 4.1 Four Experimental Conditions to Examine Laminar Coflow Diffusion Flame

	Normal Gravity	Microgravity
Normal Temperature	**Case I**	**Case III**
Preheated Temperature	**Case II**	**Case IV**

First, comparing case I with case II, reveals the effect of preheating the combustion air under normal-gravity conditions. The results thus obtained are then used to form the basis for comparison with the corresponding results obtained under low-gravity conditions. In both cases I and II, direct flame photography, particle image velocimetry (PIV) and optical-emission spectroscopy diagnostics are all employed to examine the laminar coflow diffusion flames. Direct flame photography is applied to acquire information about the global flame structure, shape and intensity. PIV diagnostics are used to provide a better understanding of the effects of preheated

combustion air upon the flowfield. The PIV data provides detailed information on the dynamics of the flow associated with high-temperature combustion air conditions, two components of its mean and rms velocity, its strain rate and 2-D vorticity. The experiments also serve to validate and further develop the model of combustion under technologically important conditions for which data does not currently exist in the literature.

The effect of preheated air upon the propane-air diffusion flame is measured by optical-emission spectroscopy. In these experiments, the spatial distributions of flame temperature are determined from the conventional two– line method, using C_2 vibrational bands. An Abel transformation is applied to create a three-dimensional, spatial distribution of selected radicals within the flame.

The next case involves analyzing the effects of low gravity on laminar coflow diffusion flames at normal inlet air temperature. Many investigators have examined flame shape and appearance under normal and low-gravity conditions and using different fuel types and different techniques to reduce the effects of gravity (see chapter 2 for more details). Much work has also been performed on comparing case I and III. The motivation of these studies has been theoretical; although microgravity combustion has few real-world applications, it is easier to model.

Our work is the first to consider case IV, preheated-temperature/low-gravity laminar diffusion flames. Comparing cases II and IV involves the effects of low gravity on laminar coflow diffusion flame at preheated combustion air temperature. The experimental facility used for low gravity is the same as that used for normal gravity conditions. This facility is modified to accommodate PIV data in normal-

gravity conditions, requiring accessories, such as a flow seeder. Measurements of laminar jet diffusion flame shapes under low gravity conditions are carried out using a 1 second free-fall drop tower. Direct flame photography is the only diagnostic that applied in order to obtain the global characteristics of the flame.

Finally, comparing case III and IV, involves the effects of preheating combustion air on laminar coflow diffusion flame under microgravity conditions. For comparing, Lin and Faeth correlations [12] are used to obtain flame length and width for normal temperature combustion air under low gravity conditions.

4.3 Comparison of Case I with case II

In this case an evaluation of the effects of preheated combustion air on laminar coflowing jet diffusion flame under normal gravity conditions was conducted using direct photography, PIV and optical spectroscopy diagnostics. The data collected reveal important information that is needed to determine preheated-air effects on the global and chemical behavior of laminar coflow diffusion flames under normal gravity.

4.3.1 Direct Flame Photography

Experiments are performed with normal-temperature and preheated combustion air. The temperature of the combustion air examined here is either room temperature (approximately 298 K) or preheated to a temperature of roughly 973 K. This temperature was obtained using an electrical preheater (3.5 Ω wire at 50 volts).

The global flame photographs are analyzed for the total flame length and width at normal gravity conditions. Figure 4.1 reveals that, at higher air preheat temperature; the flame becomes shorter, as compared to normal-temperature combustion air. CH filters were used in these photographs to provide a more distinct view of the flame shape (only wavelengths associated with CH radical radiation are allowed to pass through this filter).

Figure 4.1 Comparison of Laminar Coflow Diffusion Flame Length in Normal-Gravity with Normal (Left) and Preheated Combustion Air (Right) Using CH Filter

By increasing the air preheat temperature the complex combustion reaction is enhanced so that combustion completes within a smaller domain and results in a shorter and narrower flame size. Thus the combustion process takes place in a shorter time domain. Buoyancy accelerates the flow and causes a narrowing of the flame, since conservation of mass requires the streamlines to move closer to each other as velocity increases. However, the role of buoyancy becomes less important if the temperature of the preheated combustion air causes a considerable decrease in difference in density between the hot combustion products and the preheated inlet air.

Different regions of the flame are characterized by different colors. A yellow-colored flame region follows the initial blue-color flame region immediately downstream of the burner. The length of the yellow region is higher at higher air preheat temperatures. It has been observed that the heat release improves with preheated combustion air. Thus heat release improvement widens the fuel conversion region and causes the centerline fuel to react and decompose faster and earlier in the preheated combustion air diffusion flame. Soot inception and growth time increases and results in an increase of the soot yield. Therefore, it can be concluded that air preheats using normal combustion air results in significantly increased soot production.

The flame color results from the radiation of different wavelengths that occurs during the combustion process. The bluish-white and blue color of the high calorific fuels (such as propane) with higher-oxygen-concentration air is due to the combustion of atomic carbon to carbon monoxide and subsequently carbon dioxide, which results in the release of large amounts of chemical energy. Significant amounts of soot are generated in the lower portion of the flame when preheated air is used. Figure 4.2 shows photographs of the luminous flame shape under preheated conditions. This figure indicates that using preheated combustion air causes a more luminous flame. Preheated combustion air generates more soot as well as increases the temperature of the flame. Our evidence suggests that this increased luminosity is the cause of these soot particles under preheated conditions, as shown in Figure 4.2. This result may appear counterintuitive initially, but will be explained in detail below.

Figure 4.2 Normal Temperature (Left) and Preheated, T = 673 K, (Right) Combustion Air Flame

4.3.2 Optical-Emission Spectroscopy

The optical-emission signatures from combustion experiments provide information on the chemical behavior of flames. Optical flame emissions are the result of specific molecular electronic transitions from excited states produced in non-equilibrium concentrations by specific chemical reactions. Thus the resulting chemiluminescence is a marker for this particular chemistry, and only optical detection equipment is required. OH, CH and C_2, which are important reactive radicals present in the flame, create the strongest bands. These bands can be detected by chemiluminescence with the use of ICCD camera and narrow bandpass filters.

Experiments are performed with normal and preheated air in order to determine the effect of preheated air on the behavior of diffusion flames formed by fuel injection into a surrounding environment of co-flowing combustion air. The measurements were made with the ICCD camera having an interface filter designed to pass light signal for the species to be detected. The momentum flux ratio of the preheated combustion air jet versus fuel jet was maintained constant, thus providing

similarity in the mixing between the fuel and air under different test conditions. The ratio of preheated combustion air momentum to fuel jet momentum is maintained of a constant value of 5 during the preheating process. The air and fuel flow rate and velocity at different temperatures are shown in table 3.2. The fuel flow rate is 60 cc/min and the flame length at normal temperature air is 32 mm.

4.3.2.1 CH Emission Intensity Profiles

Figure 4.3 shows the two-dimensional distribution of CH at different air preheat temperatures. The color bar in this figure is a scale of photon energy concentration of the radical species. The higher energy concentration of the radical is represented by the brighter colors. The measurements were made with an ICCD camera fitted with an interference filter for passing only the light signal of the CH radical. Different approaches to interpreting the CH distribution in a diffusion flame have been presented [56]. CH along with OH and HCO are known to be useful indicators of the reaction zone of a flame. It has also been observed that CH concentration corresponds very closely with the peak of the temperature profile [57]. Figure 4.3 reveals that the area over which the CH species are distributed in the flame becomes narrower at higher air preheats, and the flame size diminishes as well. The results at higher air preheat temperatures also show a shorter flame when compared to normal temperature combustion air results. Reduction in the flame length, resulting from an increase in the oxidizer temperature, is shown in Figure 4.4. The results show that an increase in preheated combustion air temperature by about 400 K, causes a 37.1% reduction in the flame length.

Applying Abel inversion, three-dimensional spatial distributions of CH radicals (as indicator of the flame surface based on Han and Mungal [56] studies) were obtained (see Figure 4.5). The three axes in figure 4.5 corresponds the three dimensional position, in pixels. Abel inversion assumes that one begins with a side view of a cylindrical object. In the case of a flame, the geometry is not quite cylindrical. This introduces certain nonidealities into the Abel analysis. Essentially, the 2-D vertical image is integrated to produce a 2-D top-down projection showing contours of the variable of interest within the cylindrical object.

This top-down projection is then confined with the side-view image to produce the 3-D projection shown in Figure 4.5. the "hole" in the top-down projection is an artifact of the technique, arising from very low emission intensity values near the bottom of the flame, coupled with the non-cylindrical character of the flame. The conical shape of the surface seen in figure 4.5 is also an artifact of the technique.

Slight asymmetries in the flame, coupled with the non-cylindrical character of the flame, cause the projection to be somewhat distorted. However, general trends obtained from these images are still useful. Information can be obtained regarding temperature and radical species distribution within the flame.

Although the 2-D images of species distribution used for Abel inversion are obtained by averaging of flame images, fluctuations of the flame during the imaging process caused a loss of axisymmetry in some 3-D images. The 3-D images in Figure 4.5 show the effect of preheated combustion air on flame structure and are represented by the CH radical distribution.

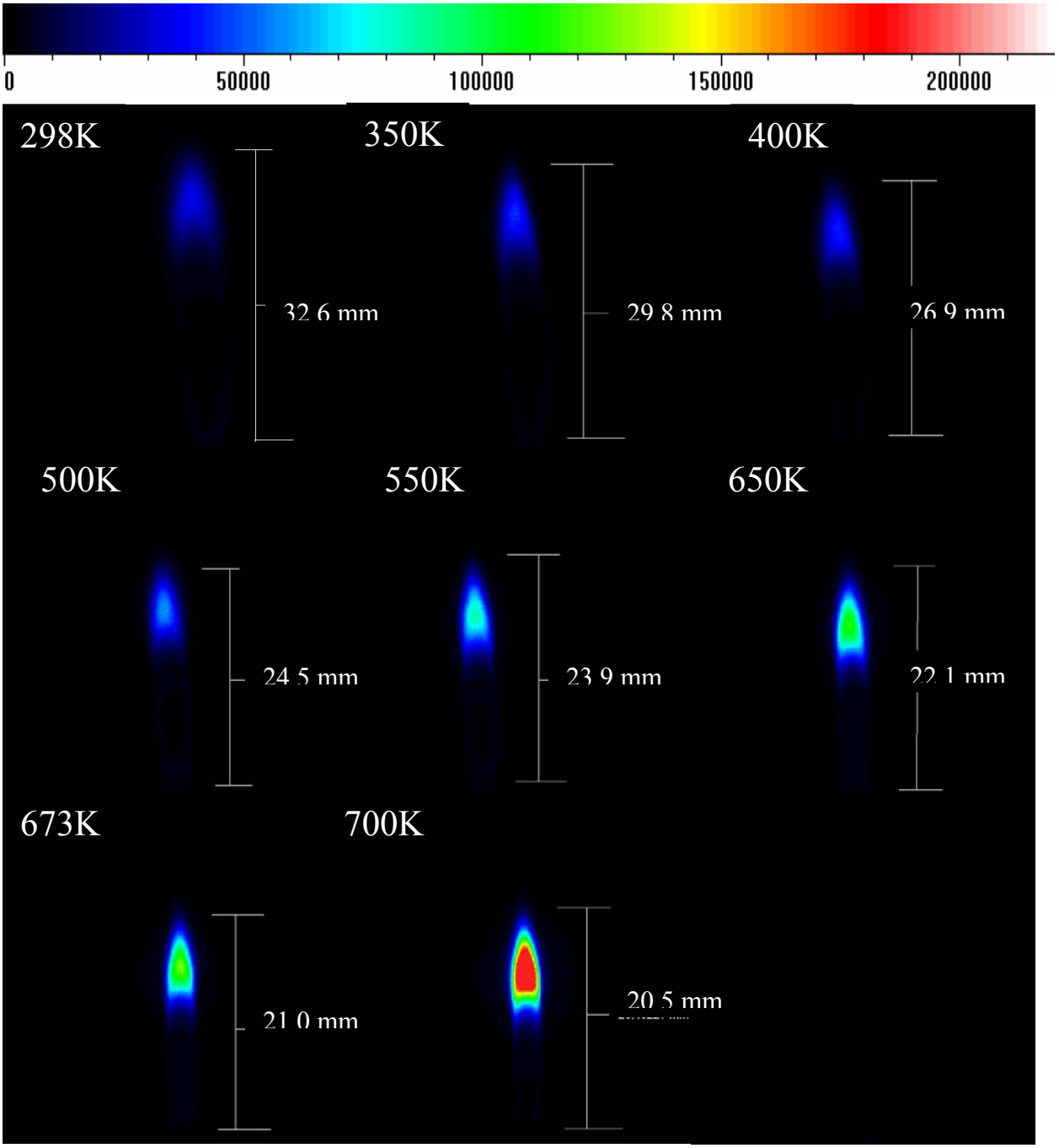

Figure 4.3 Emission Intensity Profiles of CH Radicals in the Flame for Air Temperatures 298K, 350K, 400K, 500K, 550K, 650K, 673K, 700K

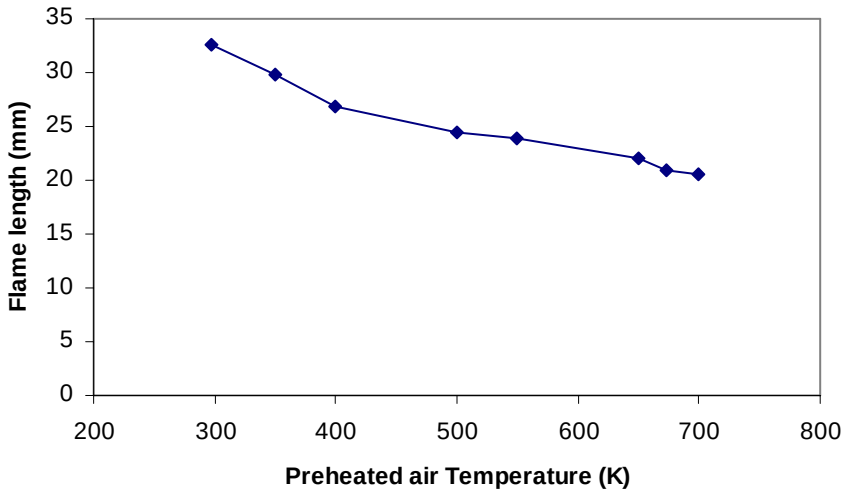

Figure 4.4 Length of the Preheated Combustion Air Laminar Flame as a Function of Preheated Air Temperature

The preheated combustion air brings the high-radical luminous intensity region (representing the stoichiometric flame front) closer to the center of the flame volume. Although the volume over which the CH radical is distributed in the flame becomes smaller at higher air preheat temperatures, the CH radical intensity significantly increases and shows that the location of maximum flame temperature is at the center and downstream of the preheated combustion air flame. Figure 4.6 gives the maximum CH intensity inside the flame versus the preheated combustion air temperature. It can be observed that increasing combustion air temperature has a significant effect on CH production inside the flame.

Figure 4.6 shows that a 400K increase in preheated air temperature increases the CH concentration of the flame by ~83.3%. This change is because the increase in preheated combustion air temperature causes an increase in chemical reaction rate and a decrease in flame volume.

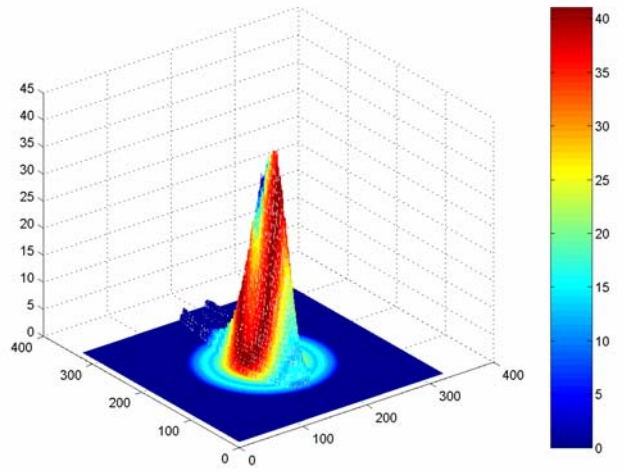

298K

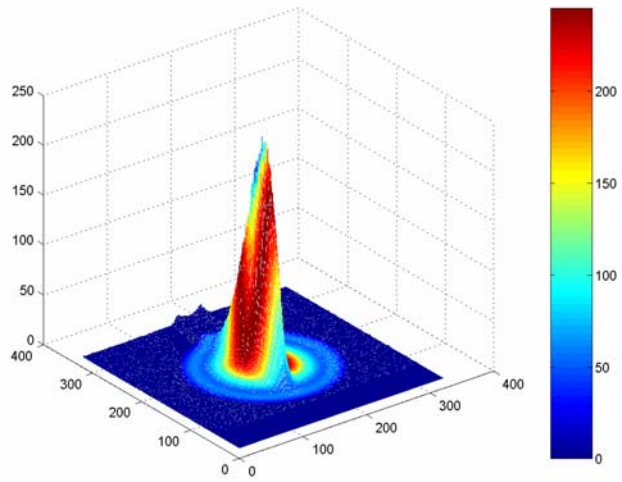

350K

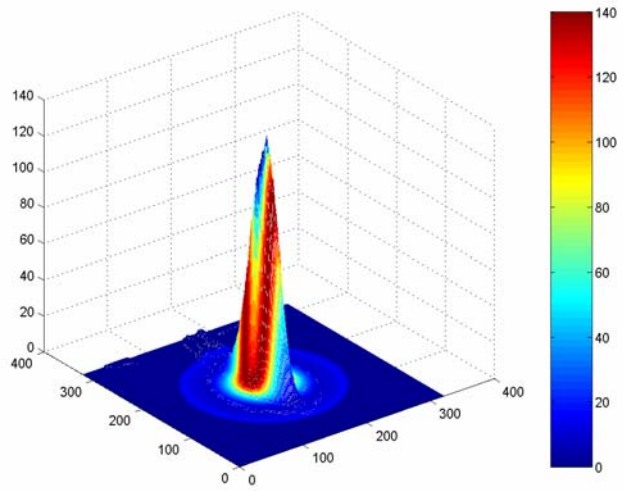

650K

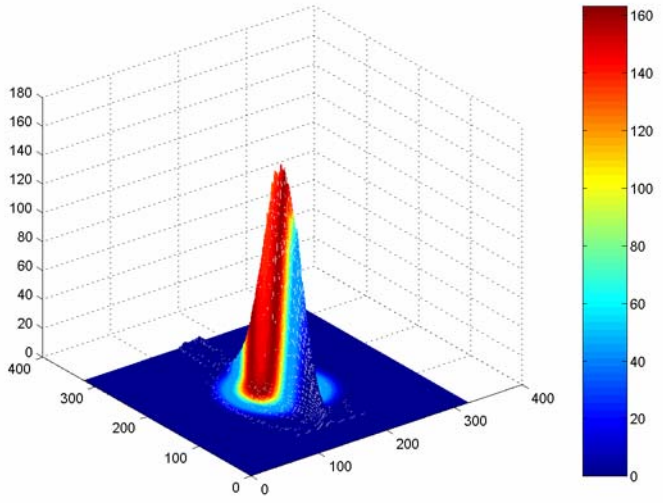

750K

Figure 4.5 Representation of the Three-Dimensional Intensity of CH Radiation for Different Preheated Air Temperature

Comparison of the CH radical intensities, as a marker of the heat release zone, shows that the higher preheated combustion air flames have higher CH emission intensities. The increase in the intensity of the CH distribution shows that the preheated combustion air increases the rate of chemical reaction. The direct photography data showed that using preheated combustion air causes a more luminous flame. In agreement with the three-dimensional data obtained by Abel inversion analysis, direct photography data implies that higher combustion air temperature causes more soot as well as increases the temperature of the flame.

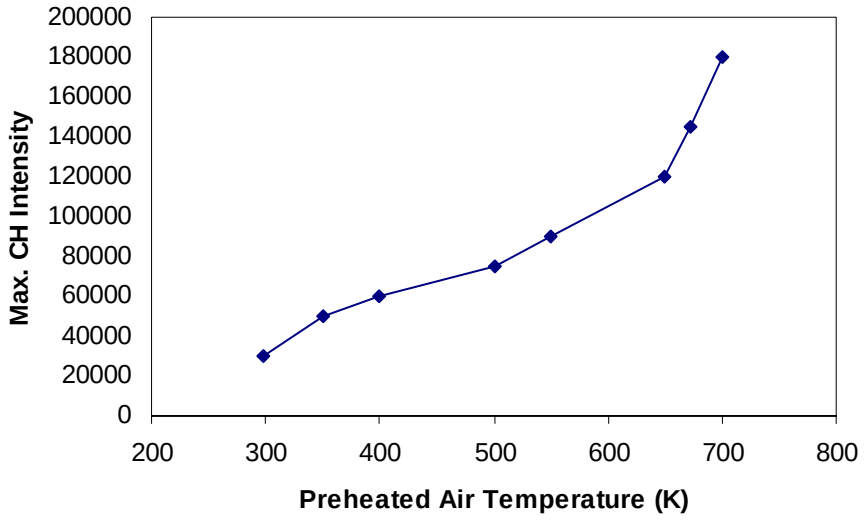

Figure 4.6 Maximum CH Intensity in the Flame as a Function of Preheated Air Temperature

4.3.2.2 C_2 Emission Intensity Profiles

The yellow portion of the flame results from the incomplete combustion of carbon within the fuel; this yellow region is associated with the production of soot

and carbonaceous material. Figure 4.7 shows the C_2 distribution and intensity for different preheated air temperatures. The effects of preheated air temperatures on the distribution and intensity of C_2 can be seen through a comparison of flames at different preheated air temperatures. Figure 4.8 shows the maximum C_2 intensity inside the flame, as a function of the preheated combustion air temperature. It can be observed that increasing combustion air temperature has a significant effect on C_2 production within the flame. The results show that a 352K increase in preheated air temperature increases the C_2 content of the flame by ~60%.

The three-dimensional density distribution of C_2 in the flame was obtained using Abel inversion (Figure 4.9). Abel inversion was also used to generate top-down images of C_2 distribution showing the radial distribution of C_2 radiation intensity (see Figure 4.10). The results in 3-D and 2-D images show that the concentration of C_2 increases at higher air preheats. Furthermore, as seen from the 2-D images in Figure 4.10, the area over which the C_2 species are distributed in the flame becomes narrower because the flame itself is narrower and smaller. This suggests that a high temperature air produces a higher local C_2 concentration near the center of the flame. Under certain conditions some polymerization of C_2 may also occur to form solid carbon that is responsible for the yellowish visible radiation that is attributed to the presence of carbonaceous particles.

Experimental studies have revealed that nucleation occurs first, followed by surface growth, followed by oxidation [61]. Surface growth is the dominant soot formation mechanism (more important than nucleation) for laminar coflowing diffusion flames.

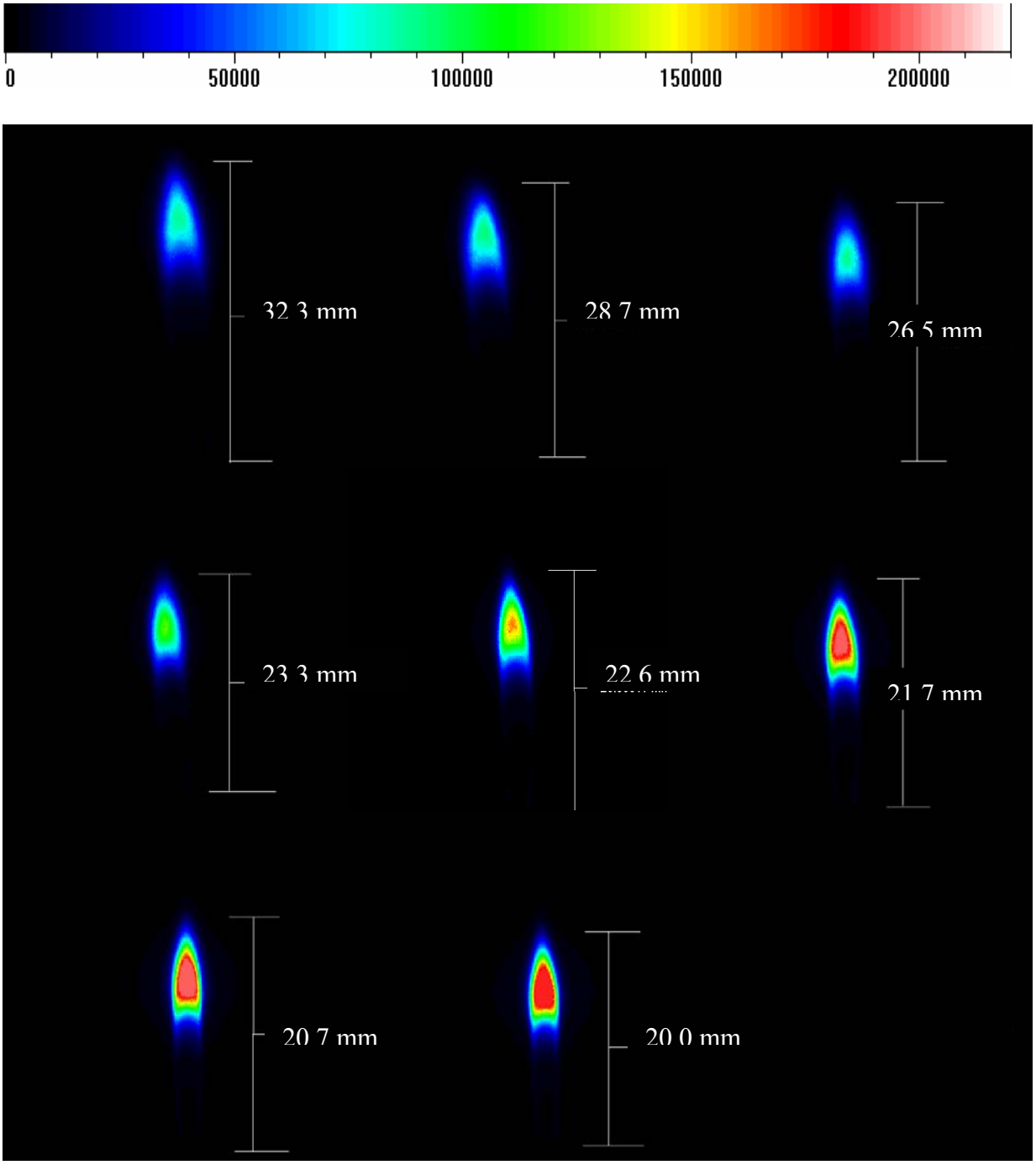

Figure 4.7 Emission Intensity Profiles of C_2 Radicals in the Flame for Air Temperatures 298K, 350K, 400K, 500K, 550K, 650K, 673K, 700K

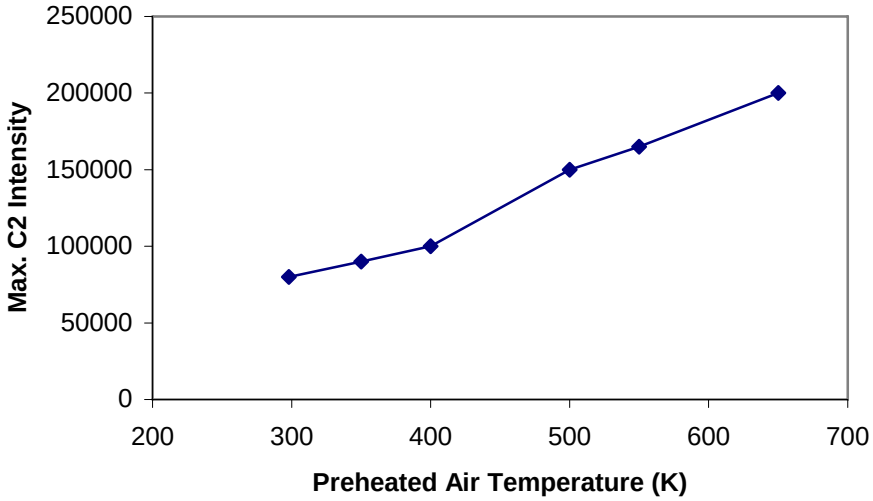

Figure 4.8 Maximum CH Intensity in the Flame as a Function of Preheated Air Temperature

The oxidation of soot occurs primarily as a result of attack by molecular oxygen and OH radicals, which increases with air preheat temperatures. Kaplan et al. [40] conclude that the dominant soot-oxidizing species is OH in normal diffusion flames, and is more effective than O_2. They show that a larger fuel-air velocity ratio results in a longer residence time to transition from nucleation to the oxidation stage, thus allowing for more soot particle growth.

Since velocity affects the residence time, different velocity profiles between the two normal and preheated air cases affect the flame temperature and soot concentration. In the present experiments, the fuel/air stream velocity ratio increases with increased air temperature at a constant momentum ratio. Thus more time is available for soot surface growth and these soot particles cross the flame sheet, thereby increasing the soot volume fraction of the flame.

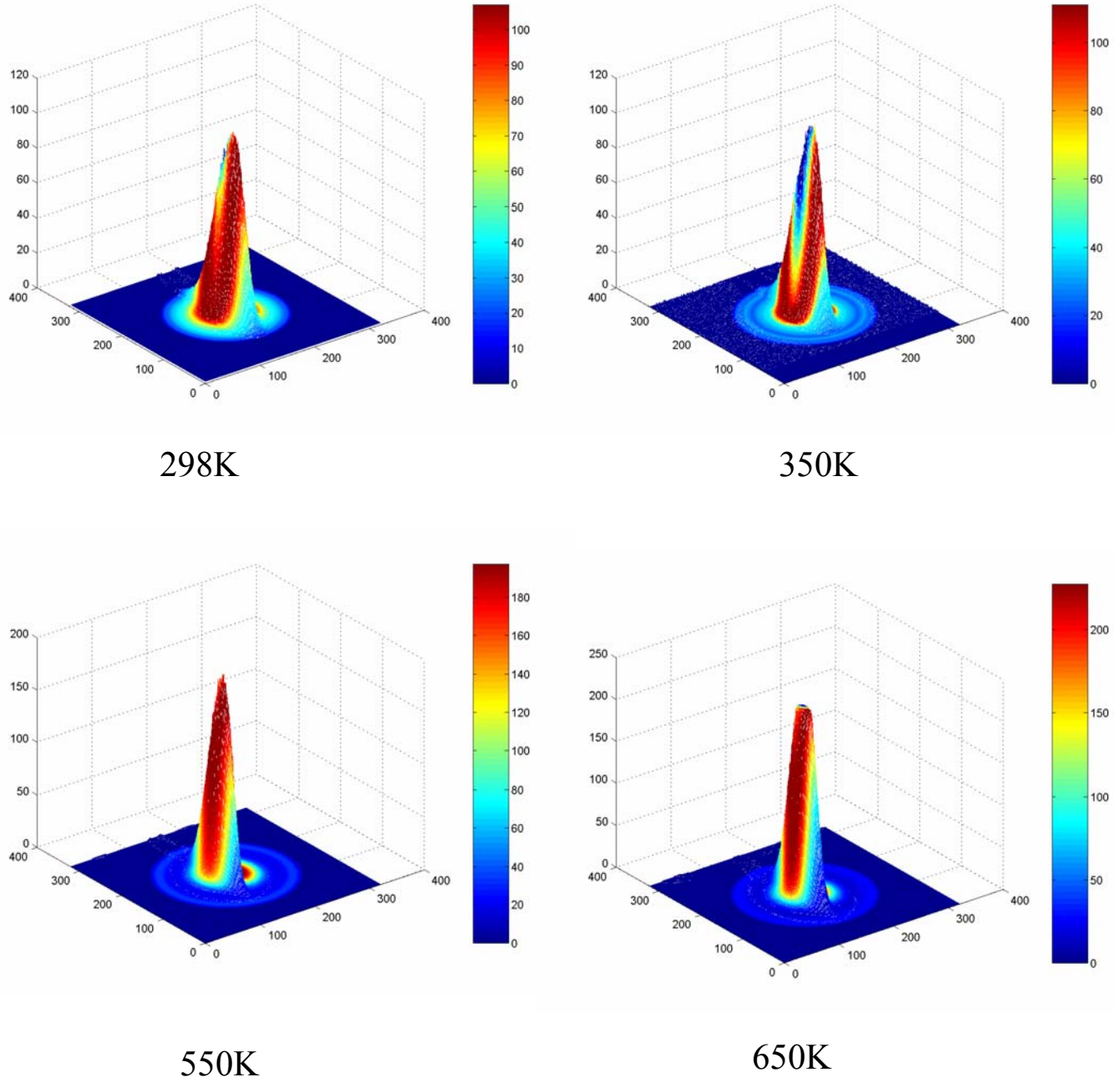

Figure 4.9 Representation of the Three-Dimensional Intensity of C_2 Specie for Different Preheated Air Temperatures (Showing Radial Spreading)

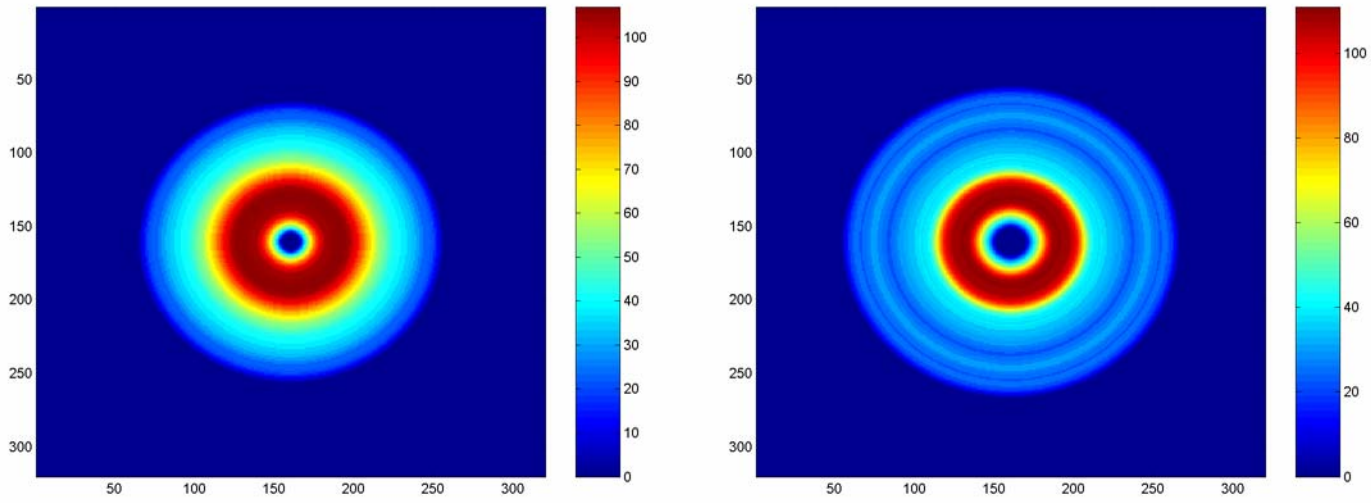

298K

350K

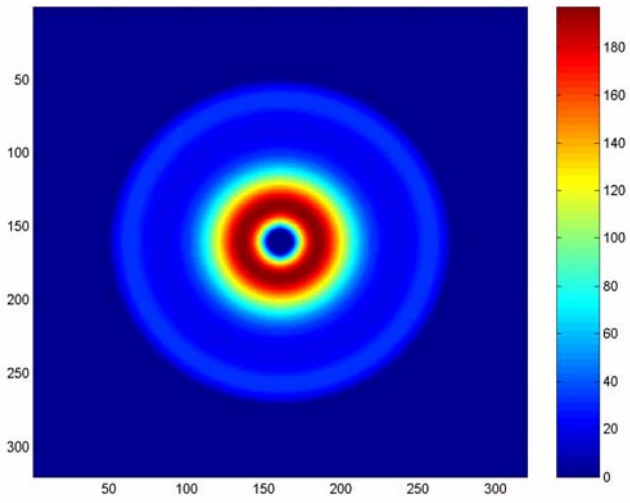

550K

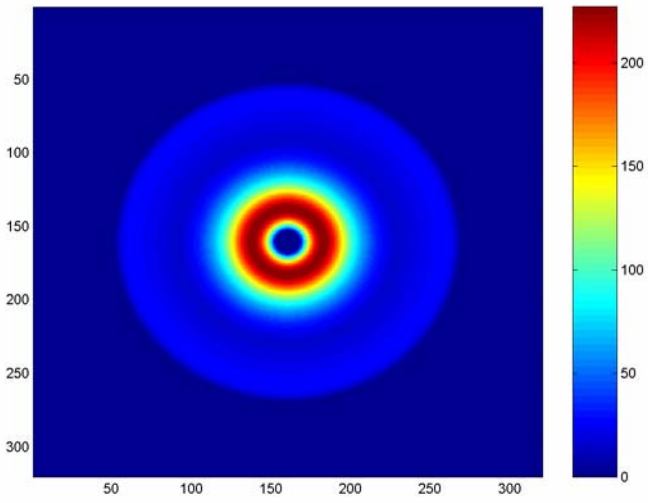

650K

Figure 4.10 Cross-sectional View of the Intensity of C_2 Specie Images in the Flame at Different Preheated Air Temperatures

Although air preheating increases the concentration of OH in the flame, the rate of soot production through surface growth is dominant (Figure 4.11). It has been observed that the peak soot volume fraction in the laminar diffusion flame occurs when the mixture fraction is 0.08 – 0.09, and the temperature is 1870 – 1920K [40]. Therefore, it can be expected that the soot volume will attain its peak value in the lower part of the flame and that a significant amount of soot will be generated in the upper part of the flame. The images in Figures 4.5 and 4.6 exhibit similar tendencies for the C_2 intensity profiles (i. e., the maximum C_2 intensity is at downstream of the flame).

4.3.2.3 Vibrational Temperature Distributions in the Flame

It is clear from photographs that increasing luminosity of the flame at preheated combustion air temperatures results from increased soot generation and higher flame temperatures. Three-dimensional spatial distribution of CH radicals also supports this observation. CH as an indicator of heat release rate increases significantly with preheated air temperature, implying that the flame temperature increases with increasing preheated air temperature. To examine this phenomenon, the vibrational temperature of C2 within the flame has been determined by comparing the emission intensities at two vibrational bands, which occur from the same electronic transition. The ratio of the peak intensity at these two wavelengths is a function of the gas temperature.

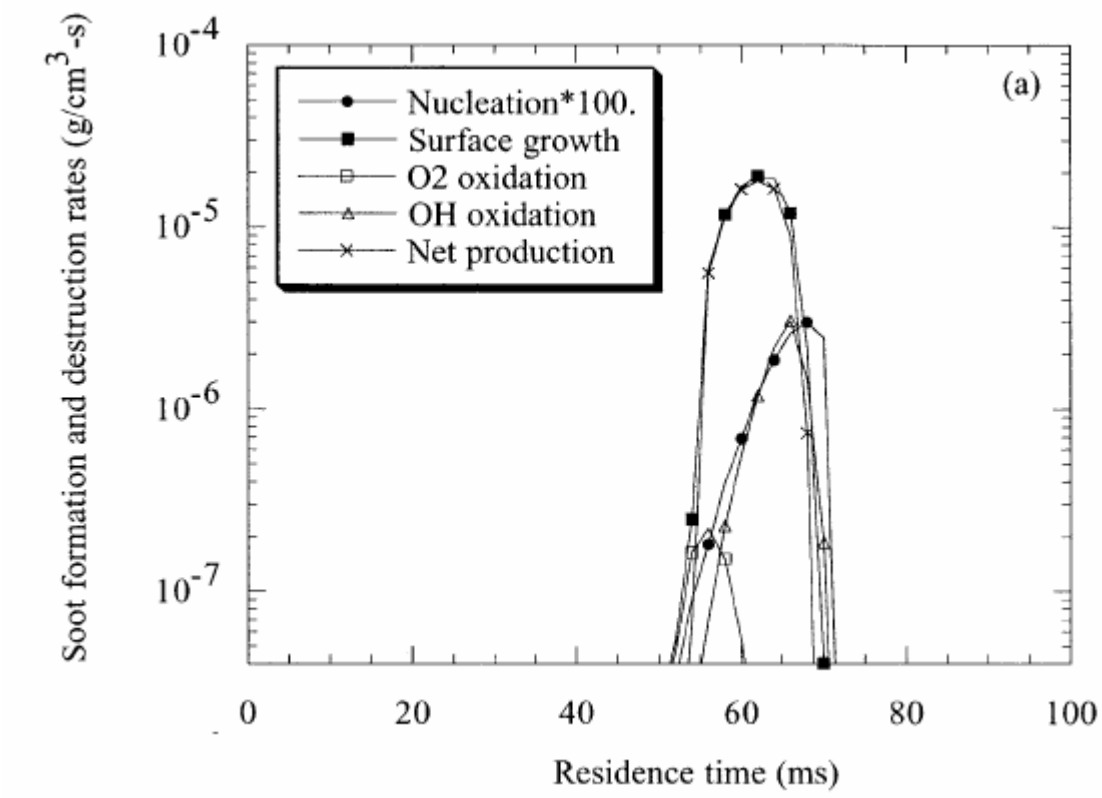

Figure 4.11 Soot Creation and Destruction Processes Along the Path Line Going Through the Maximum Sooting Region for the Laminar Coflowing Diffusion Flame [40]

In this study, the relationship between the temperature measured with a thermocouple and the spectral intensity ratio of the C_2 bands that reflects the vibrational temperature has been determined experimentally. A calibration curve is obtained by comparing thermocouple measurements and spectral intensities at certain points in the flame. With this calibration curve, the spectral intensity ratios at the ICCD pixels are converted into thermocouple equivalent temperature. Therefore, many systematic errors are eliminated by converting the spectroscopically-measured temperatures to the temperatures measured with thermocouples. The errors associated

with the vibrational temperature are mainly due to the thermocouple temperature measurement and C_2 emission intensity ratio. A length of 50 μm platinum – platinum/rhodium 13% type R thermocouple wire having a precision welded junctionwas used for the thermocouple probe. The company correlations curve for the thermocouple is advertised to be accurate within ±3 K in the temperature range of interest. The main source of error results from the intensity ratio measurements, arising from distortions of the initial emission intensity images of flame radicals. These are integrated images; the effect of integration can distort the comparison of relative intensity for images. Therefore the distortion of images can be a source of inaccuracy in obtaining a flame-temperature profile. The largest error in a C2 intensity ratio measurement is ± 2.3%. This error in intensity ratio measurement causes ± 3.7% uncertainty in the vibrational temperature calculation.

Figure 4.12 shows the vibrational temperature distributions of the C2 vibrational bands of the propane flames at different preheated combustion air temperatures. The temperature distribution images at higher air preheat temperatures suggest that enhanced reaction rate in the flame zones takes place in the presence of preheated combustion air, thus making the reaction region small. However, the temperature distributions for the flame at higher combustion air temperature increases. The temperature distributions also show that higher preheated combustion air increases the temperature of the flame close to the burner exit. This is the reason for the increased flammability limit of preheated flames.

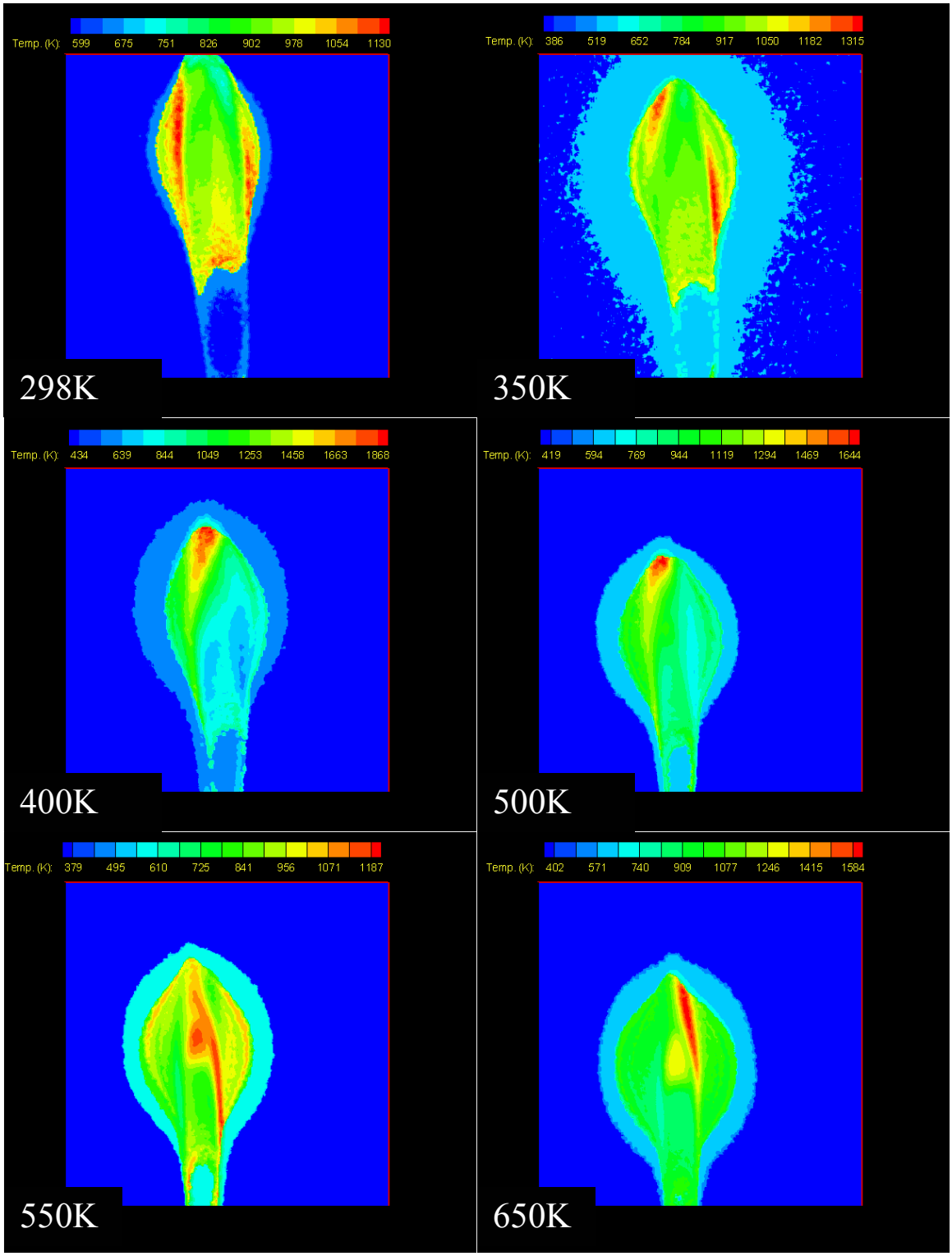

Figure 4.12 Vibrational Temperature Profiles Calculated from the Ratio of C_2 Emission Intensities in the Flame for Air Temperatures 298K, 350K, 400K, 500K, 550K, 650K, Under Normal Gravity

The higher temperature of the flame close to burner exit causes the centerline fuel to react and decompose faster and earlier. As seen in the images, the maximum temperature therefore occurs further downstream for all flames. This is consistent with the results that have been obtained by analyzing the direct photography data and the CH and C2 emission intensity profiles. The effects of preheated air on the temperature distribution inside the diffusion flame are identified as an increase in temperature distribution and more homogeneity. This homogeneity can be attributed to higher stability in the flowfield characteristics for preheated combustion air diffusion flame.

Changes in the peak temperature, relative to changes in the preheated combustion air temperature, are shown in Figure 4.13. The results in this study show that a 352K increase in preheated air temperature improves the heat release rate and increases the peak temperature of the flame by ~24.6%.

4.3.2.4 OH Emission Intensity Profile

The OH radicals provide a marker for the flame reaction zone. Figure 4.14 shows the OH emission of the flame at different air preheat temperatures. It can be seen that the preheated combustion air increases the intensity of the OH distribution in the flame. OH intensity reaches its peak value near the top as well as at the edge of the lower elevations of the flame. The advection of surrounding air to the centerline region of the flame is responsible for increasing OH emission at the front edge of the flame.

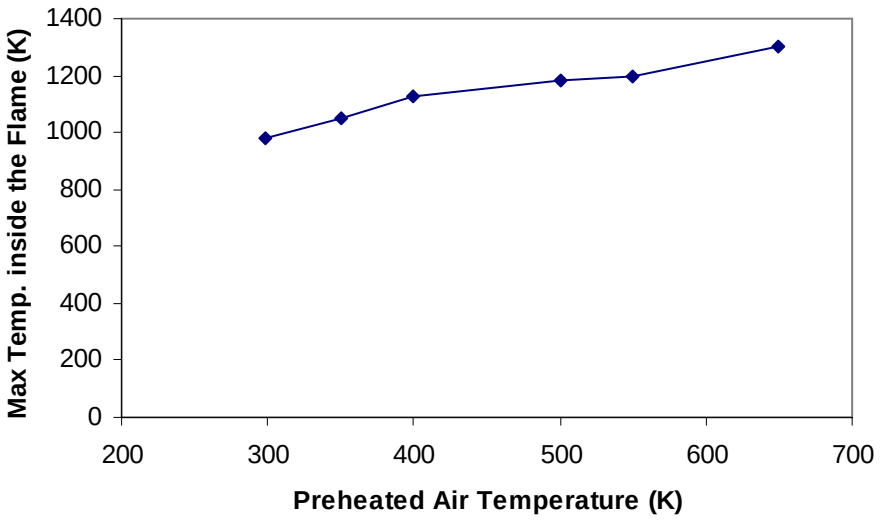

Figure 4.13 Flame Maximum Temperatures versus Preheated Combustion Air Temperature

This advection of air causes the OH radicals to be transported toward the central axis of the flame, an effect that becomes more noticeable at higher preheat temperatures due to the enhanced mixing around the flame. Friedman and Burke [64] suggest that the propane-air flame consists of a two-stage reaction zone. The first stage is the conversion of C_3H_8 to CO and H_2O, and the second is conversion of CO to CO_2. Numerical modeling results of 2-D methane-air laminar coflow diffusion flames, obtained by Smooke [65] show the location of CO and CO_2 region inside the flame (see Figure 4.15 and 4.16). Lim et al [66] study the effect of preheated air on flame structure in counterflow methane-air diffusion flames using sampling and gas chromatography. They determined that the molar concentrations of CO, OH and H all increase with an increase in preheated air temperature.

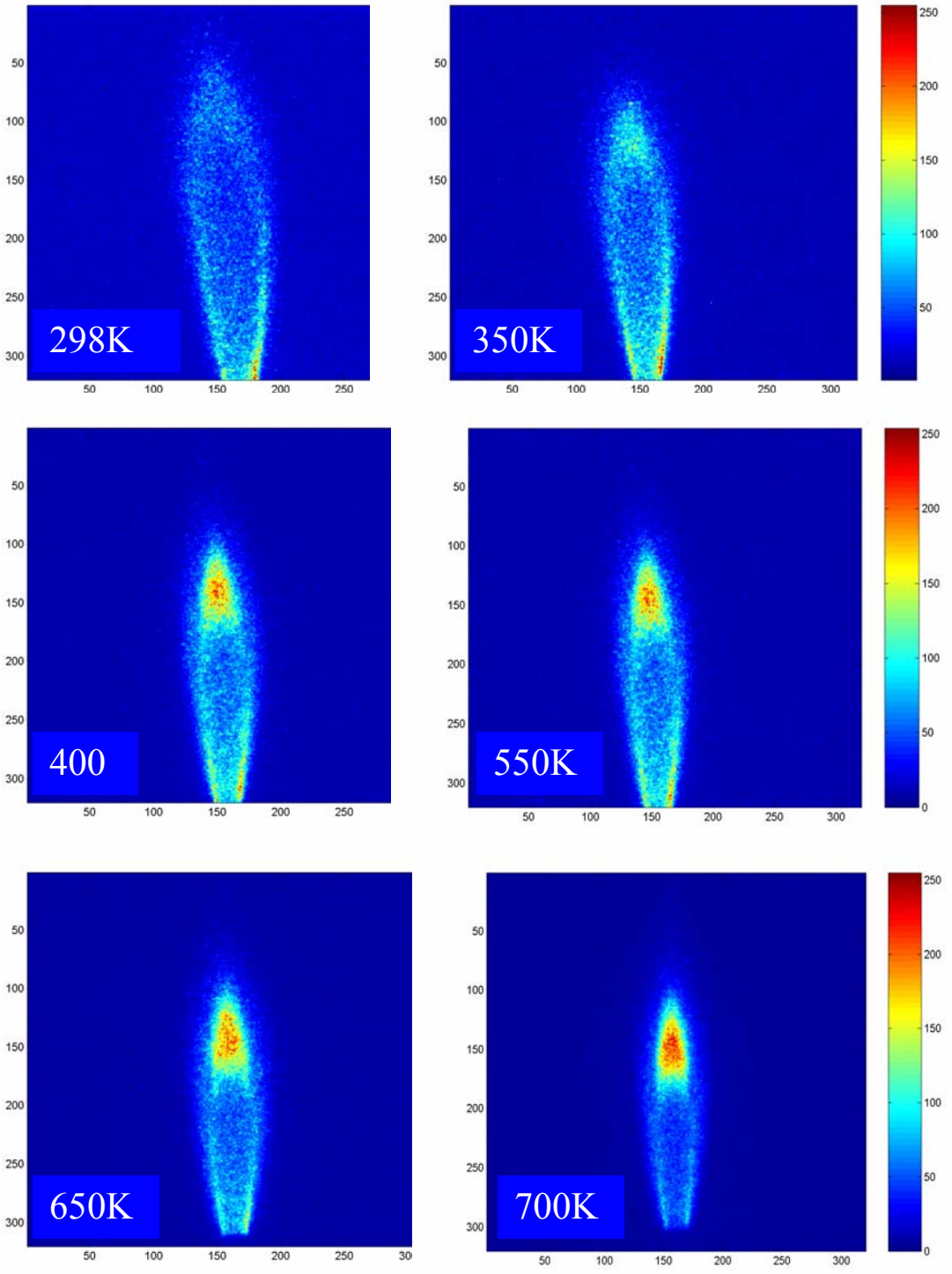

Figure 4.14 Emission Intensity Profile of OH Radical in the Flame for Air Temperatures 298K, 350K, 550K, 650K, 700K

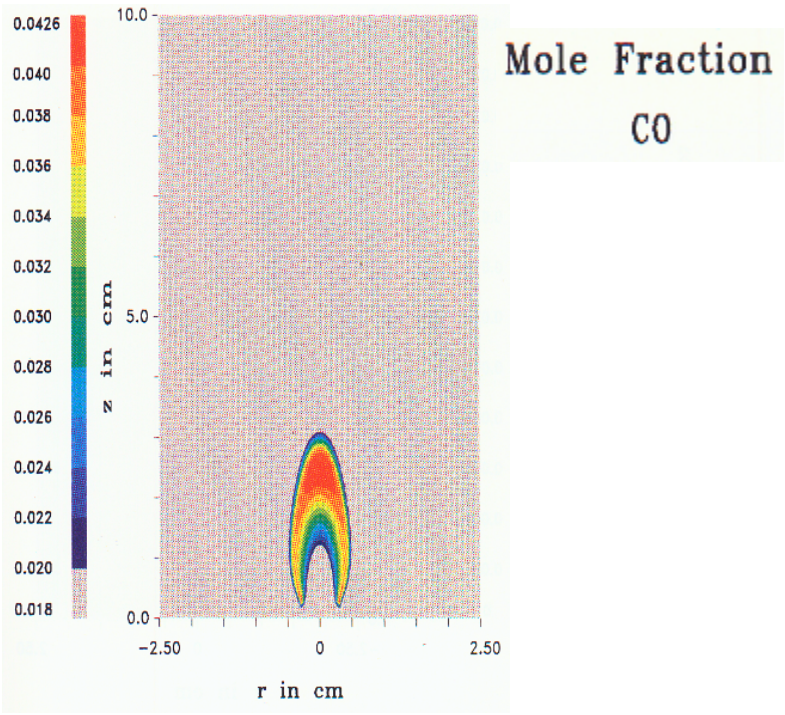

Figure 4.15 Calculated Carbon Monoxide (CO) for the Methane-Air Diffusion Flame at Normal Air Temperature [63]

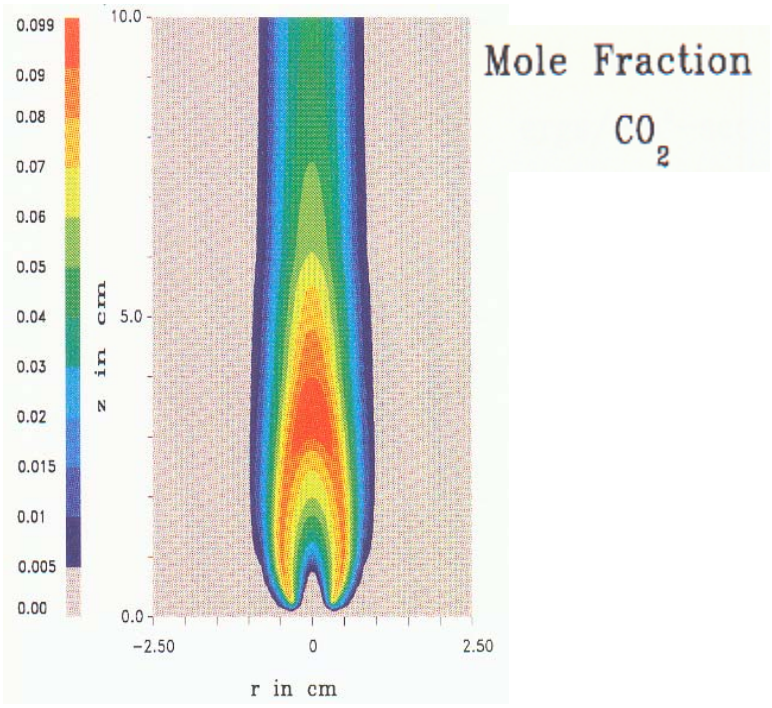

Figure 4.16 Calculated Carbon Dioxide (CO_2) for the Methane-Air Diffusion Flame at Normal Air Temperature [63]

The rates of CO+OH<=>CO_2+H reaction (W_{99} in the Figure 4.17) in both the forward and the reverse directions increase, as a result. However, the increase in the reverse reaction rate is higher than that for the forward reaction rate, causing an overall increase in the CO and OH concentrations at the top of the flame, further contributing to OH radical production in this area (see Figure 4.17).

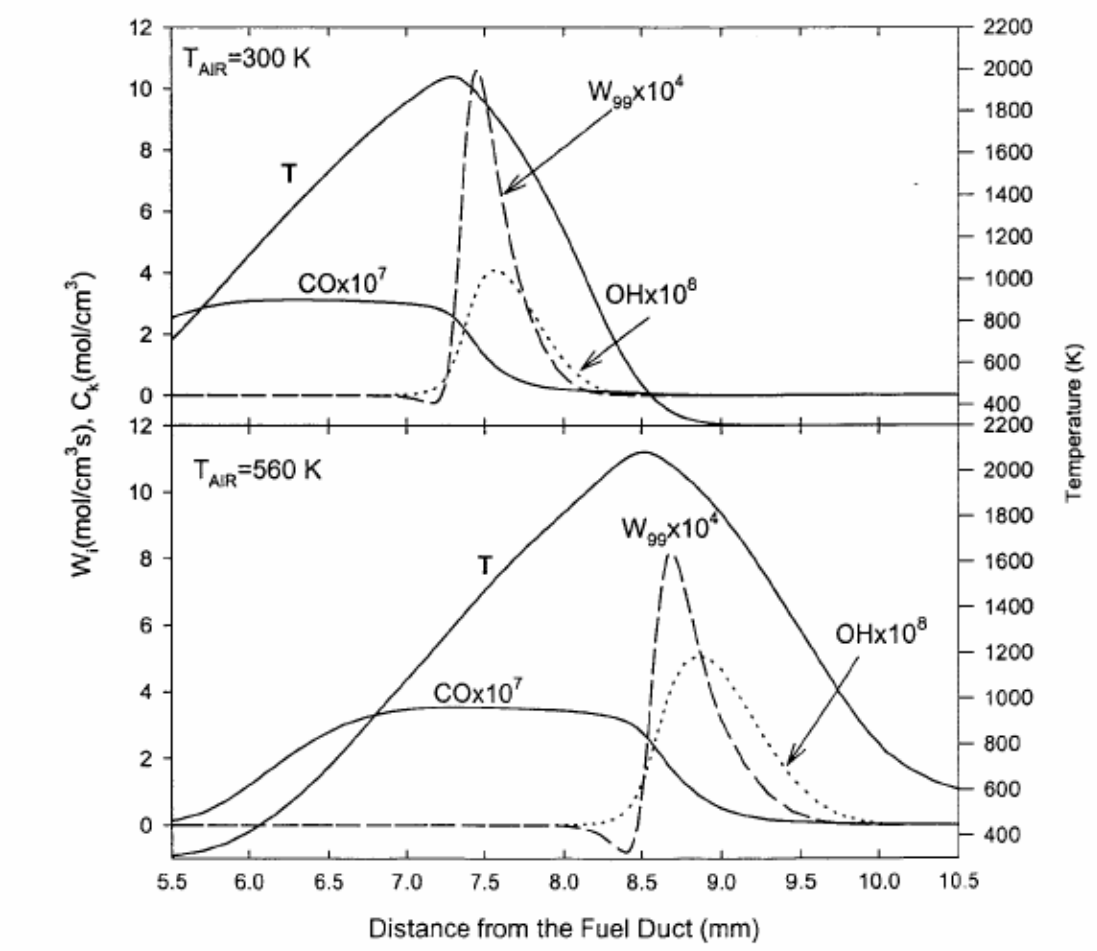

Figure 4.17 Temperature, CO and OH Profiles and the W_{99} (CO + OH → H + CO_2) Reaction Rate Profile for Two Preheat Temperatures [64]

The experimental results in Figure 4.14 show the same behavior. The peak value of OH concentration is near the top of the laminar coflow diffusion flame and

results from the effects of the preheated air on the CO2 conversion region. Increases in the reverse reaction rate become higher than that for the forward reaction rate, causing an increase in the CO and OH concentrations at the top of the flame. The percentage of increase of OH radical concentration in the diffusion flame is due to the preheated combustion air temperature increase is shown in Figure 4.18. The results show that a 350 K increase in preheated air temperature increases the maximum OH radical concentration of the flame by ~38.5%.

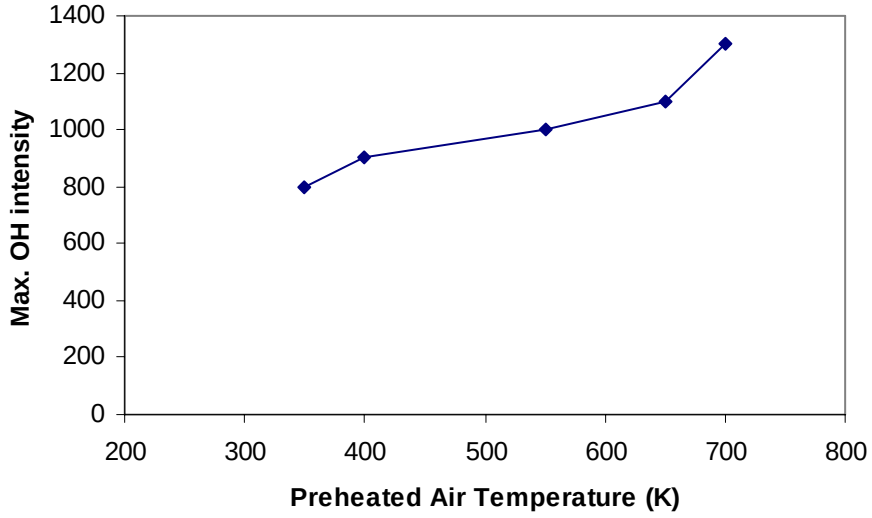

Figure 4.18 Maximum OH Intensity in the Flame as a Function of Preheated Air Temperature

4.3.3 Particle Image Velocimetry (PIV)

Data acquisitions are conducted from 250 image pairs of the flow field, from which the characteristics of the flow are determined. The momentum-flux ratio of the preheated combustion air jet to that of the fuel jet for different temperatures of combustion air has been maintained as a constant. The ratio of preheated combustion

air momentum to fuel jet momentum is 4 in these experiments (due to seeding restrictions) and this ratio has been held constant during tests. The fuel flow rate is 79 ml/min; average velocity of fuel flow at the burner tip is 0.8 m/sec. The flame length with normal temperature air is 32 mm. Measurements are carried out under both non-burning and burning conditions using normal air at normal temperature and preheated air temperatures up to 353 K (80° C). The temperature of combustion air examined was 298 K (25° C), 338 K (65° C), and 353 K (80° C).

The collected data provides important insights on the flow dynamics and strain associated with the coflow jet under preheated temperature combustion air conditions. This data also provides critical information on the dynamics of the flow and mixing associated with the flow under non-burning and burning conditions. In the present study, the gas jets are quantified by the jets Reynolds number and by the momentum ratio between the fuel jet and the air jet. For the present PIV experiments, the fuel flow Reynolds number is 256. The PIV data provide two components of the velocity vector field in our experiments. This data can be differentiated in the X and Y directions. The full velocity gradient tensor is the deformation tensor, which can be decomposed into a symmetric part and an anti-symmetric part. Thus the symmetric tensor represents the strain tensor with the elongational strains on the diagonal and the shearing strains on the off-diagonal, whereas the anti-symmetric part contains only the vorticity components. From the acquired data mean and turbulence characteristics, as well as the 2-D vorticity and axial strain are calculated. In the obtained plots, the vector length provides information on the total velocity (i.e., the resultant velocity component of axial and radial velocity). The direction of the vector

gives information on the direction of the flow field. The color-coded information in bar above the flow field images gives information on the velocity magnitude of the particular component.

Figures 4.19 and 4.20 provide the axial velocity distribution with normal temperature combustion air for the case of non-burning (no flame) flows. The non-burning case shows several essential features of the fuel jet issuing from a nozzle into the coflowing air jet. The velocity and fuel concentration decreases in the region between the potential core and the jet edge. Throughout the entire flow field, the initial momentum is conserved. As the coflowing air jet issues into the surrounding air, some of its momentum is transferred to the air. Thus, the velocity of the coflowing air jet decreases, while greater and greater quantities of air are entrained into the jet as it proceeds downstream from the burner. It can be observed in Figure 4.20 that the axial velocity profile is highly asymmetric initially. The fuel tubing, which is located horizontally in front of the inlet air passage, inside the burner, is responsible for this asymmetric behavior of axial velocity profile at the burner tip.

Figures 4.21 and 4.22 provide the axial velocity distribution with normal temperature combustion air for the case of burning flows (i.e., with flame). The burning case causes the release of chemical energy inside the flow. Therefore, for the normal air diffusion flame, the axial velocity increases with increasing height due to buoyant acceleration. As the fuel flows along the flame axis, it diffuses radially outwards, while the air diffuses radially inwards. The flame surface is where the fuel and oxidizer meet in the flammability limits of the mixture.

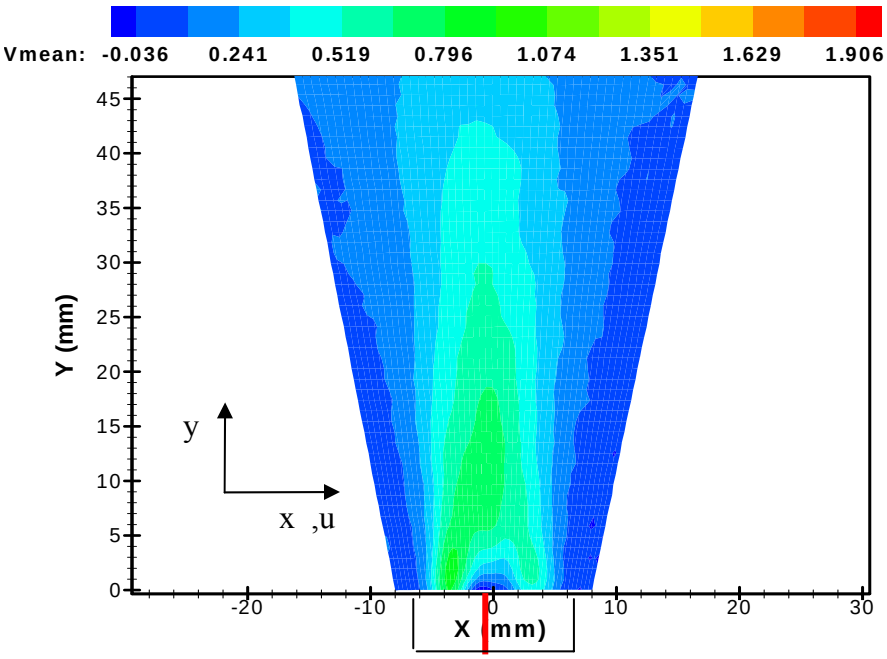

Figure 4.19 Axial Velocity Distribution with Normal Air Temperature Non-Burning Case

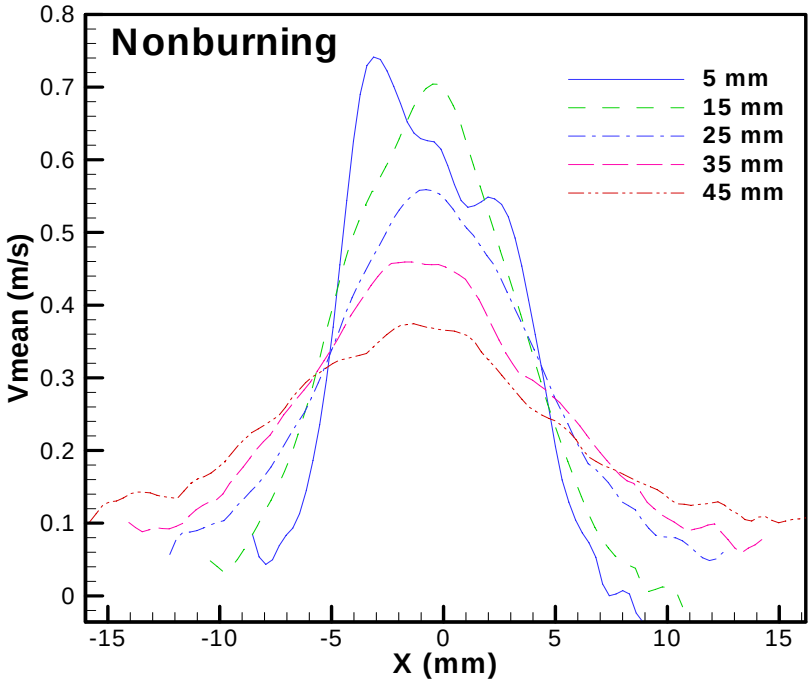

Figure 4.20 Mean Velocity Profile in Non-Burning Laminar Fuel Jet Issuing into on Laminar Air Jet at Different Distance Above Burner Tip

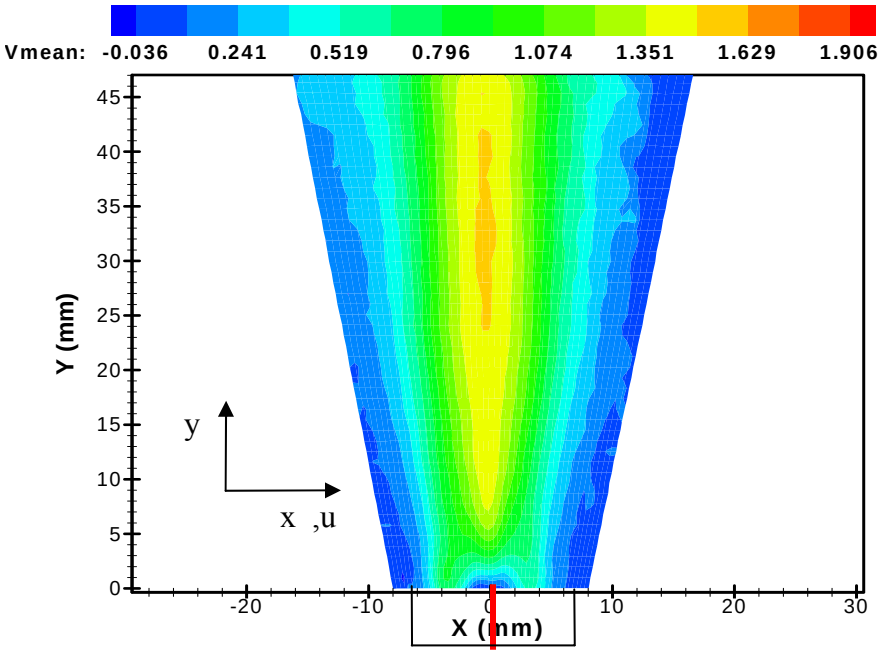

Figure 4.21 Axial Velocity Distributions with Normal Air Temperature Burning Case

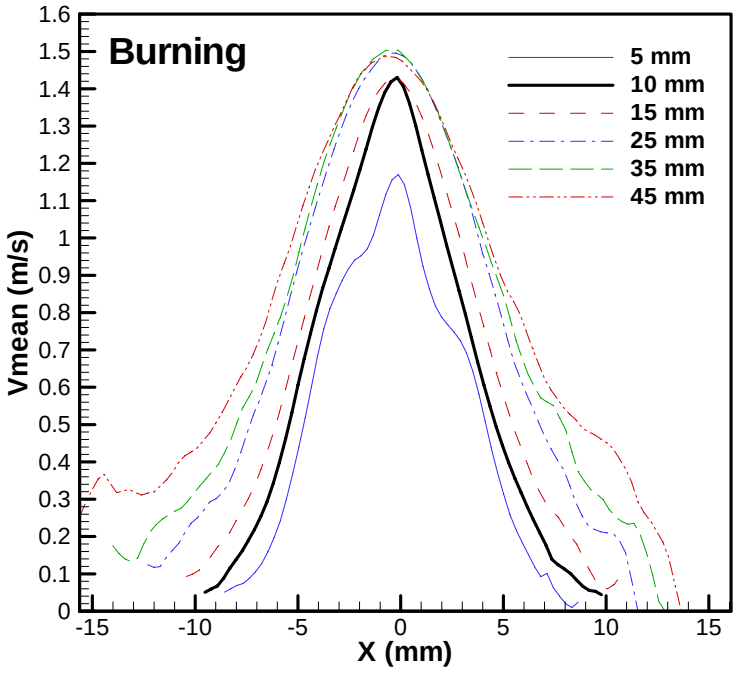

Figure 4.22 Mean Velocity Profile in Burning Laminar Fuel Jet Issuing into on Laminar Air Jet at Different Distance above Burner Tip

The region where chemical reactions take place correspond the highest temperature zone in the flow, as well as to the peak in axial velocity in the flow. A high velocity region can be seen in the downstream regions of the flame in the figures. There appears to be a sufficient quantity of hot gases in this area to cause the buoyant forces become important. Buoyancy accelerates the flow and causes a narrowing of the flame, since conservation of mass requires the streamlines to come closer when velocity increases.

Figure 4.23 shows the effects of a 338 K (65° C) air preheat temperature upon mean axial flow velocity. The velocity profile of a burning jet with air preheated to 338 K (65° C) is also shown in Figure 4.24. Figure 4.25 reveals the effects of 353 K (80° C) air preheat on mean axial flow velocity. The velocity profile of the burning jet with air preheated to 353 K (80° C) is also shown in Figure 4.26. Figure 4.27 compares maximum axial velocity inside the flame as a function of preheated combustion air temperature. By increasing the preheated combustion air from 298 to 353 K, the maximum velocity in the flame increases by about 26%.

Figures 4.23 and 4.25 also indicate that the axial velocities become higher with increases in combustion air temperature. This suggests that with preheated combustion air, the combustion efficiency improves, so that the heat release improves and fuel jet velocity distribution increases, as compared to normal-temperature combustion air. These effects are to be expected, since the velocity profiles have a maximum in the vicinity of the flame tip - at about 32 mm height above the fuel nozzle exit, using normal temperature air.

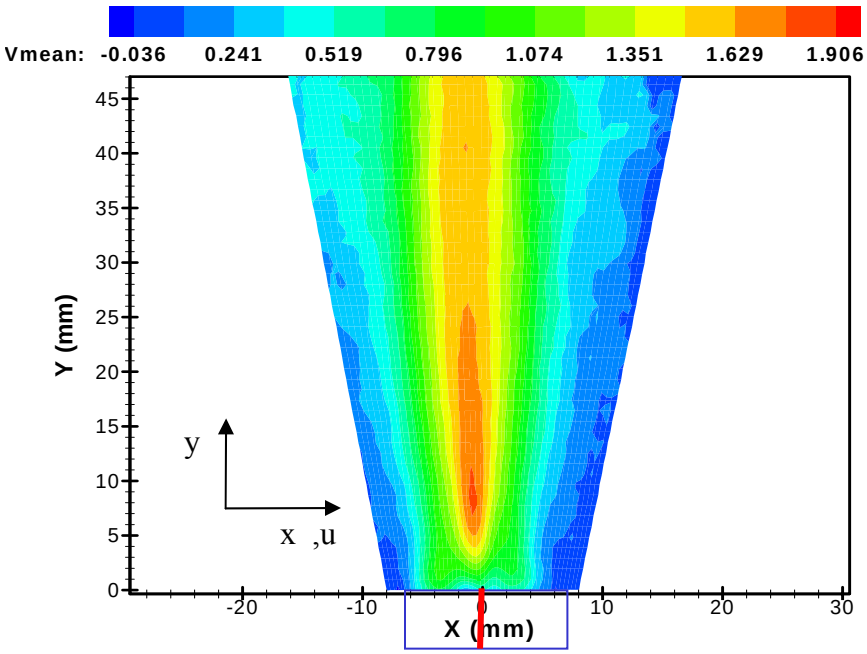

Figure 4.23 Axial Velocity Distributions with 338 K (65° C) Preheated Air Coflowing with the Burning Jet of Fuel Flow

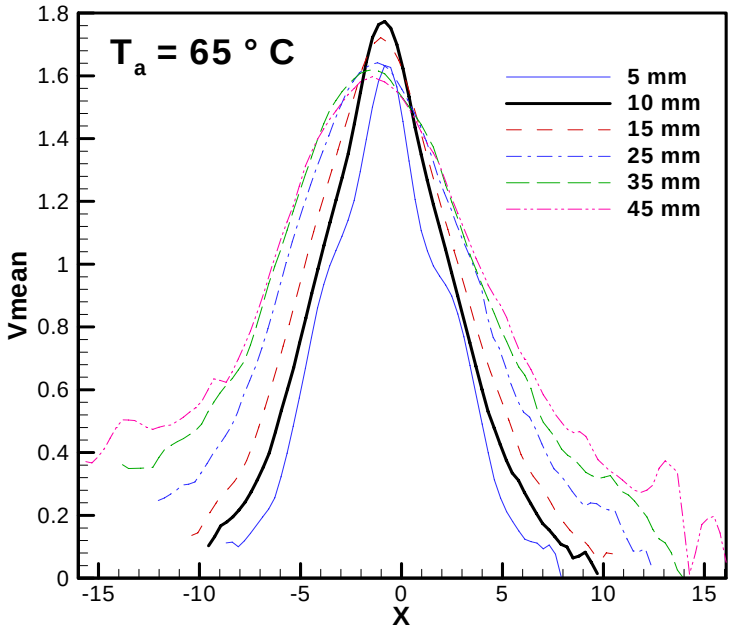

Figure 4.24 Mean Velocity Profile Using 338 K (65° C) Preheated Air Coflowing with the Burning Jet of Fuel Flow

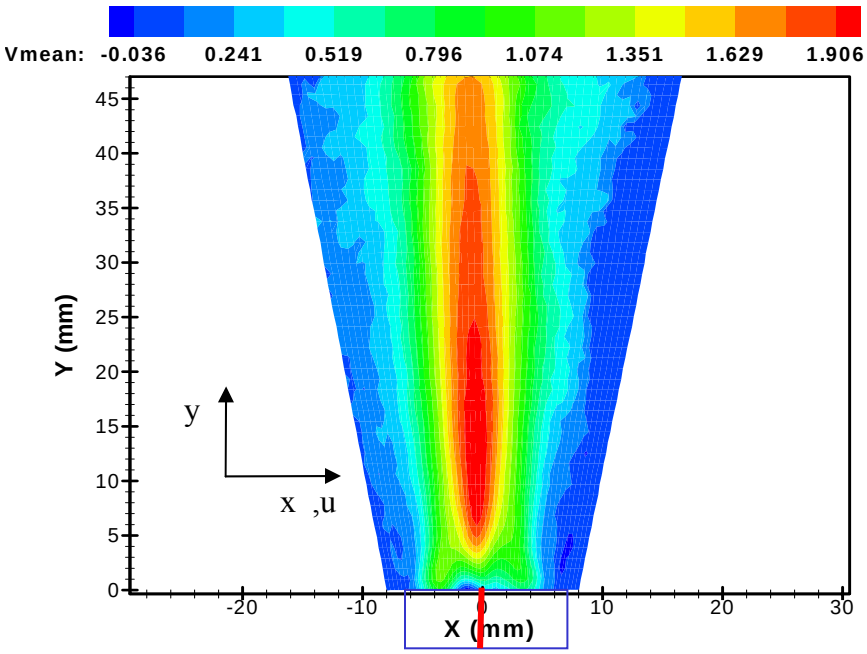

Figure 4.25 Axial Velocity Distributions with 353 K (80 ° C) Preheated Air Coflowing with the Burning Jet of Fuel Flow

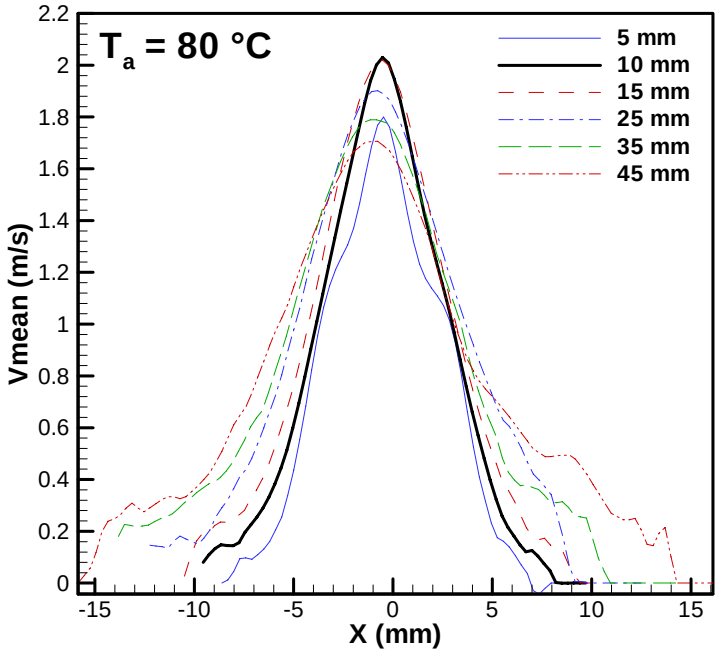

Figure 4.26 Mean Velocity Profile Using 353 K (80 ° C) Preheated Air Coflowing with the Burning Jet of Fuel Flow

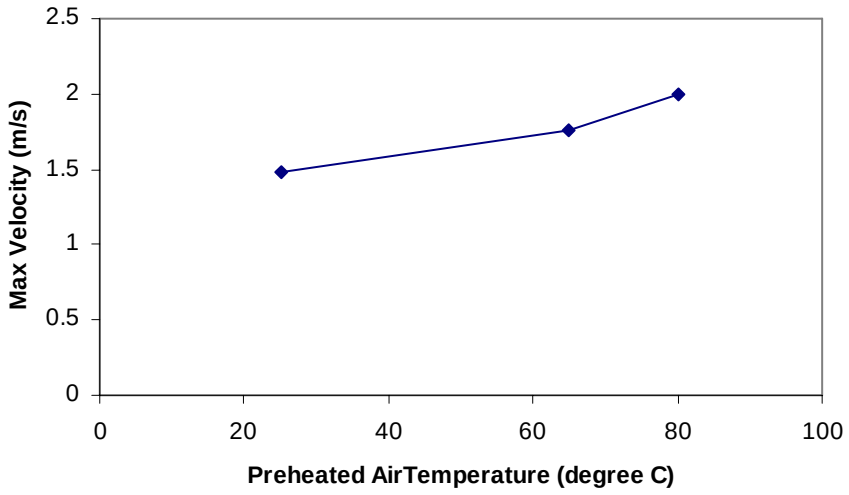

Figure 4.27 Maximum Axial Velocities within the Flame as a Function of Preheated Combustion Air Temperature

Increases in the air temperature cause the peak of maximum velocity to move upstream to lower heights above the burner (to a height of 10 mm above the fuel nozzle exit at 353 K (80° C)). The maximum axial velocity, which represents the location of maximum temperature inside the flame, increases due to the higher temperature of the preheated air (see Figure 4.25). Unlike the case of the diffusion flame with normal-temperature combustion air, the temperature profiles in the flame zone using preheated combustion air have a peak in the lower portion of the flame region. A comparison of the axial velocities for normal and preheated combustion air flames reveals that the temperature in the upper regions along the centerline of the flame increase with air preheat temperature. This causes the centerline fuel to react and decompose faster and earlier in preheated the combustion air diffusion flame cases. Meanwhile, at the flame base, since the reaction zone in the upper region moves radially away from the centerline, the fuel conversion region becomes wider.

Consequently, soot inception and growth time increases resulting in higher soot production. It can be therefore, concluded that using normal (21% oxygen content) air preheating as the combustion air results in significant increases in soot yields. This result is in agreement with our direct photographs that reveal increases in the yellow portion of the flame with preheated combustion air. Furthermore, increases in C_2 concentrations in the preheated combustion air cases examined via optical emission spectroscopy support these PIV observations.

Lim et al. [64] concluded that as the air temperature becomes higher, the rates of some elementary reaction steps increase while those of other elementary reaction steps decrease. These changes affect the flame structure. The effects of air preheat on many species and reaction rates manifest themselves through an increase in H atom concentrations. High flame temperature increased soot precursor concentrations and the incipient soot formation rate. Our results support this observation. The fuel/air stream velocity ratio affects soot formation in diffusion flames. Larger fuel/air velocity ratio results in a longer residence time to transition from nucleation to the oxidation stage, thus allowing for more soot particle growth. Since velocity affects the residence time, the difference of velocity profiles between two normal and preheated air cases will affect the flame temperature and soot concentration.

In the present experiments, the fuel/air stream velocity ratio increases with increase in air temperature at constant momentum ratio. More time is therefore available for soot surface growth and these soot particles cross the flame sheet to result in an increased soot volume fraction from the flame. This increase of the soot volume fraction has been observed in C_2 emission intensity profiles obtained by

optical emission spectroscopy (see Figure 4.5). The same result also has been obtained through observation of more luminous flame images of direct flame photography in the presence of preheated combustion air. Through optical emission spectroscopic measurements it has been found that although the air preheats increases OH species the rate of soot production through surface growth is dominant (see Figure 4.8). It has also been observed that the peak soot volume fraction in the laminar diffusion flame occurs when the mixture fraction is 0.08 – 0.09 and the temperature is 1870 – 1920K [40]. Therefore, it can be expected that soot volume attain its peak value in a lower portion of the flame for cases using preheated combustion air. The results obtained from the PIV experiments can thus be seen to support the results that were obtained from C2 emissions spectroscopy, as previously described in section 4.3.2.2. The temperature profile shows a maximum in the annular region located at the upper portion of the flame. These maximum temperature contours do not converge to the axis in the upper portion of the flame. This is due to the radiation cooling by soot, since a significant amount of soot exist in the upper flame region. Numerical simulations by Guo [65] exhibit similar tendencies (see Figure 4.28) for the temperature profiles (i.e. maximum temperature to shift to lower portion of the flame). The investigated flame in his study was a coflow, laminar ethylene – air diffusion flame in which a cylindrical fuel stream was surrounded by a 327 K preheated coflowing air jet.

The above observations are also confirmed by the stronger 2-D vorticity observed for the high temperature air case. Figures 4.29 and 4.30 reveal that an increase in velocity profile in the chemical reaction region increases the radial

velocity gradient and consequently the entrainment inside the flame with the result that vorticity increases in the burning case. The effect of high temperature air can be seen from Figures 4.31 and 4.32, which show higher vorticity for the preheated inlet air cases. The figure also shows two well-defined regions of vorticity that are the result of the jet trajectory. There is a region of negative rotation above the fuel jet and a region of positive rotation under the fuel jet.

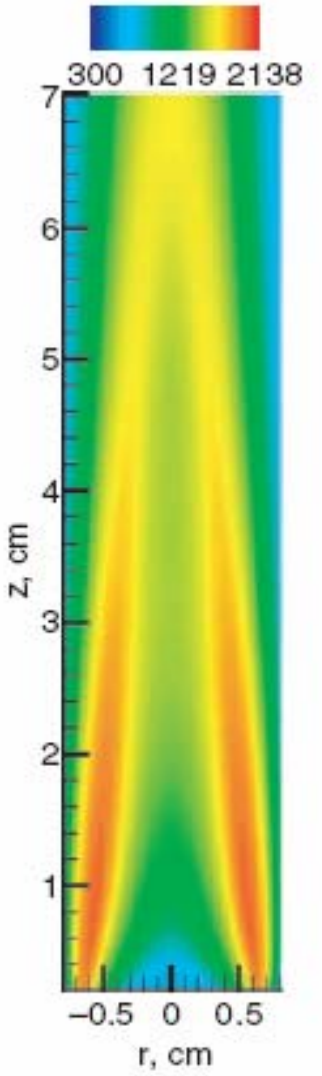

Figure 4.28 Flame Temperature (K) Contour Obtained by Numerical Simulation [65]

These results reveal that a larger region of mixing takes place around the propane fuel jet for the higher temperature air preheat case 353 K (80 °C) as compared to the 338 K (65 °C) preheated air case. The magnitude of the rotation for different cases at different levels above the burner tip can be seen in Figures 4.33 to 4.35. Generally, at all levels the magnitude of the rotation is seen to be greater for the high temperature air case. The peak in vorticity occurs 5 mm above the burner tip. A strong entrainment of the surrounding fluid can be seen in the preheated cases as compared to the normal temperature case, and is a direct result of the higher velocity of the entraining fuel jet.

The effect of preheating on radial strain rate has been seen in Figures 4.29 to 4.32: more highly preheated air causes not only increases in axial but also radial strain rate. Buoyancy effects and the diffusion of air into the flame are responsible for increasing radial strain resulting in an increased fuel-air mixing rate.

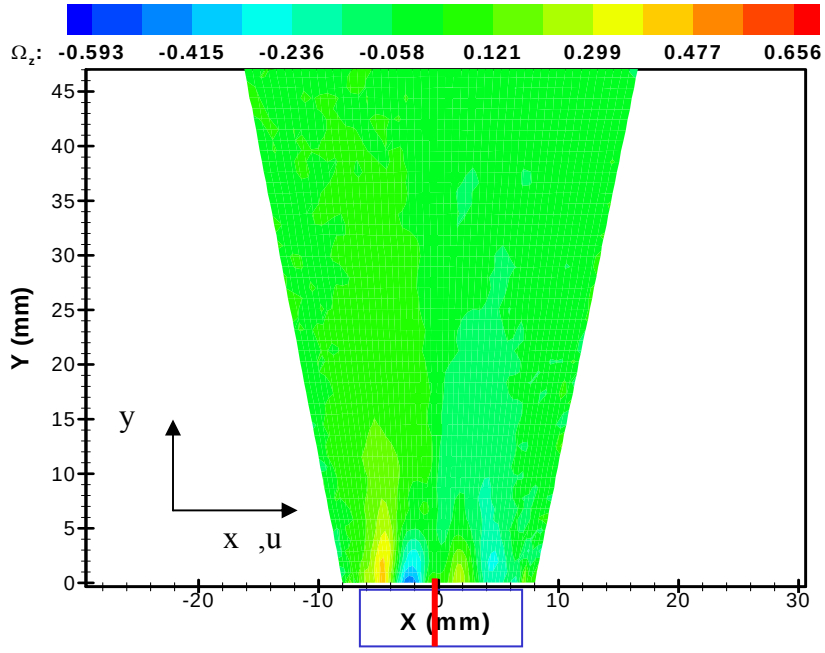

Figure 4.29 2D-Vorticity, Non-Burning Case

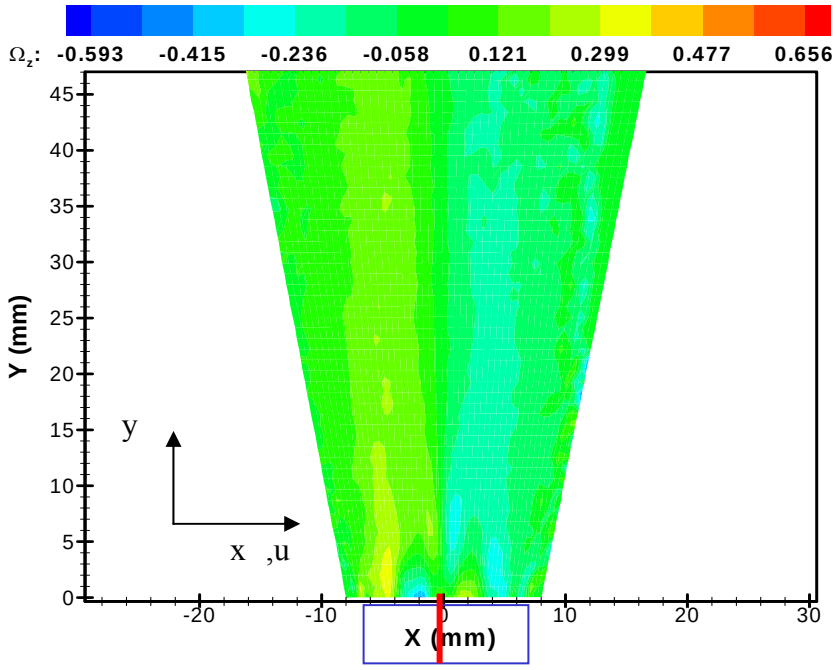

Figure 4.30 2D-Vorticity, Burning Case

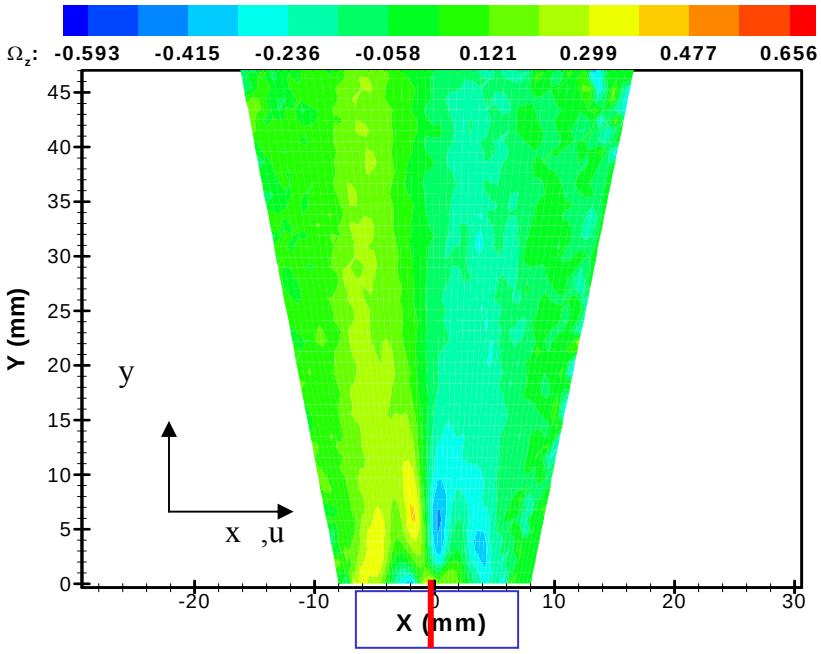

Figure 4.31 2D-Vorticity, Burning Case, T_{air} = 338 K (65°C)

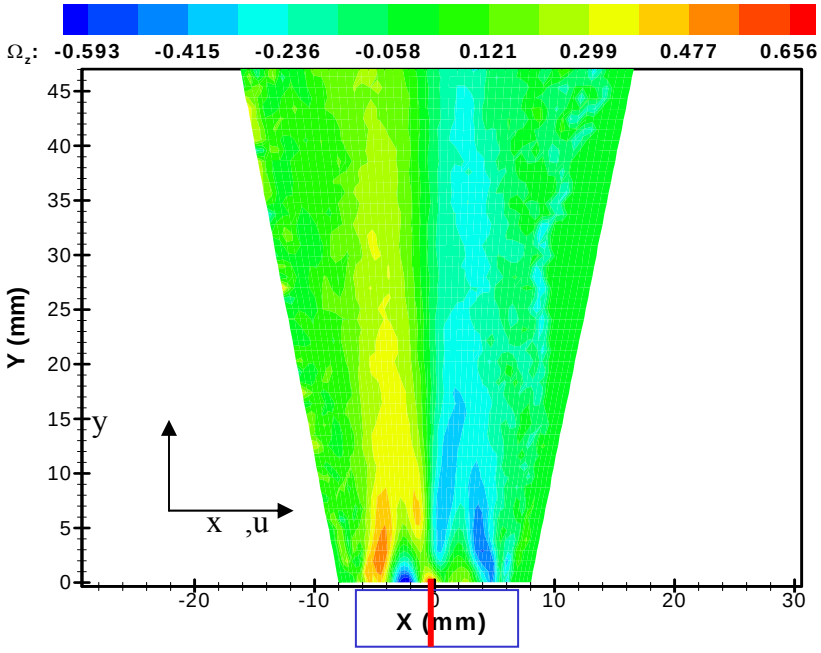

Figure 4.32 2D-Vorticity, Burning Case, T_{air} = 353 K (80°C)

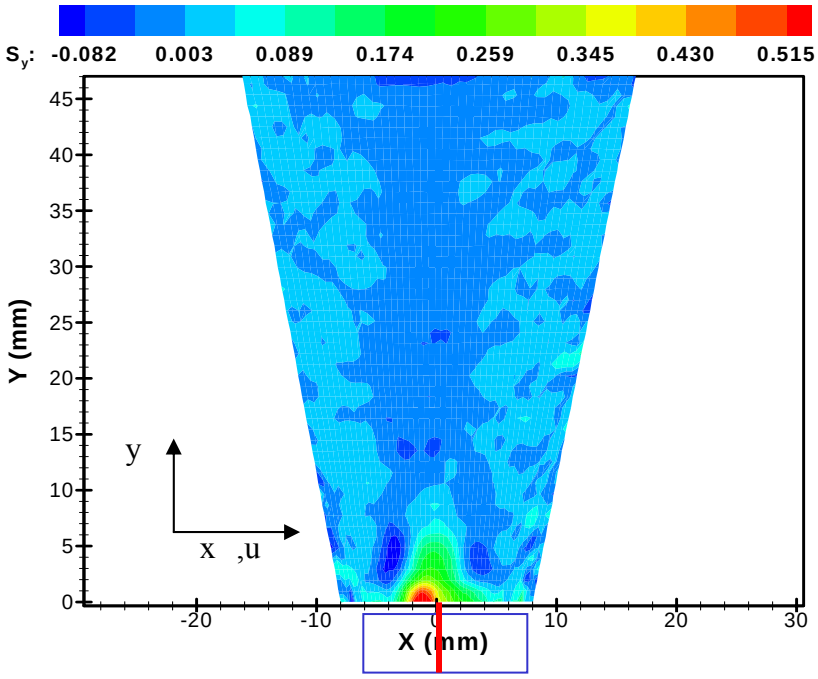

Figure 4.33 Axial Strain Rate, Non-Burning Case

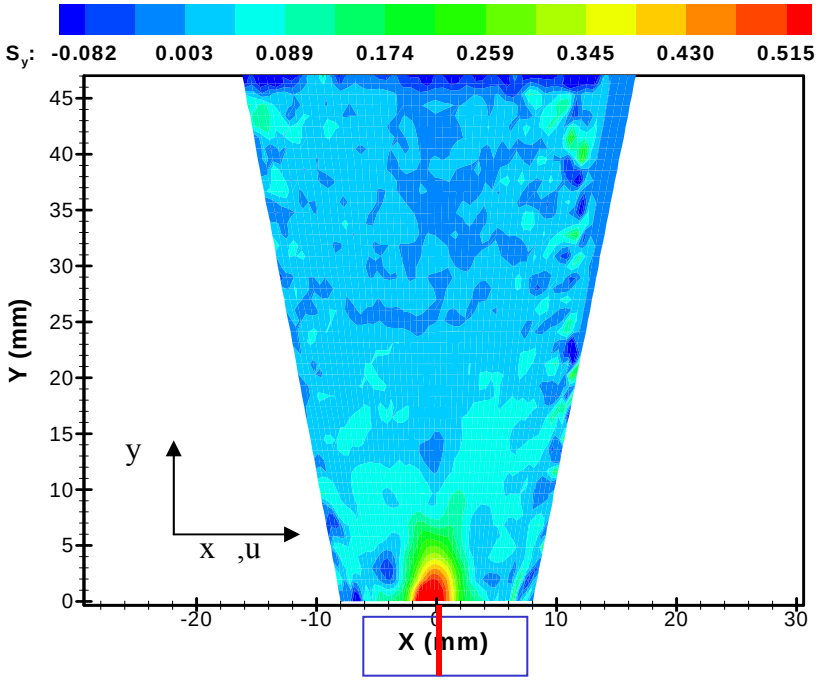

Figure 4.34 Axial Strain Rate, Burning Case

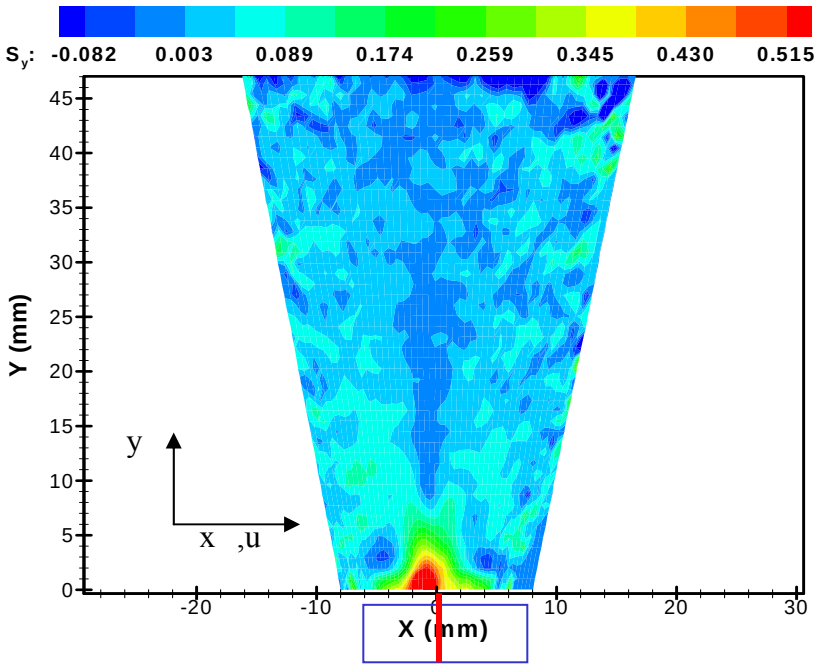

Figure 4.35 Axial Strain Rate, Burning Case, T_{air} = 338 K (65°C)

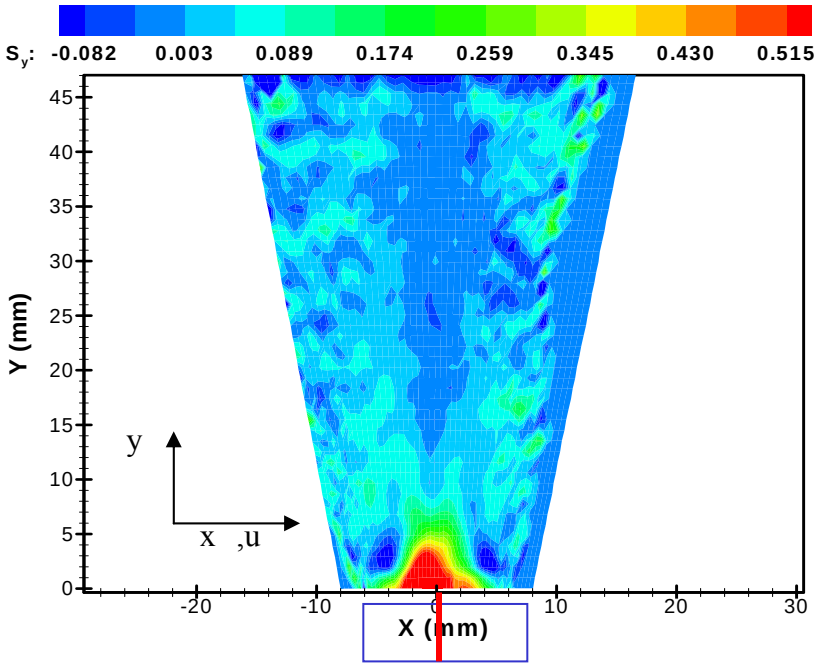

Figure 4.36 Axial Strain Rate, Burning Case, T_{air} = 353 K (80°C)

4.4 Comparison of Case I with Case III

Many investigators have studied the Effects of Low Gravity on Laminar Coflow Diffusion Flame at Normal Temperature. Figure 4.37 shows measurements of flame length for CH_4 flames. The measured flame lengths have been normalized by jet diameter, as a function of the jet's Reynolds number at normal and microgravity conditions. Compiling laminar flame data from a variety of sources shows a nearly linear relationship between flame length and Reynolds number, with significantly longer flame lengths in microgravity, due to the difference between residence times between buoyancy-driven and momentum-driven residence times.

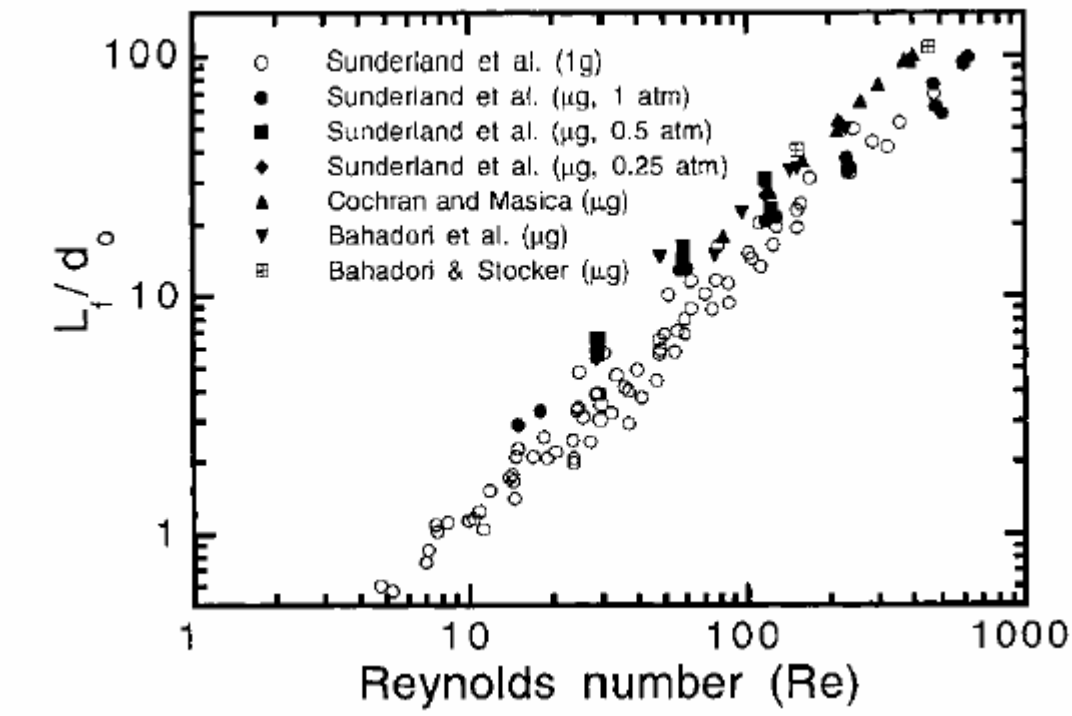

Figure 4.37 Measurements of Flame Length under Normal and Microgravity Conditions at Normal Air Temperature (reproduced from [16])

All microgravity studies show a larger flame width in microgravity than in normal-gravity conditions, due to the lower axial velocity and longer residence times. Because the flame width depends on whether axial velocity is accelerating (buoyant jets under normal-gravity conditions), constant (nonbuoyant Burke-Schumann flames), or decelerating (nonbuoyant jets under microgravity conditions), flame width is more difficult to predict than is flame length. The difference between normal and microgravity widths decreases as the Reynolds number increases and the difference between normal-gravity and microgravity width decreases as the Reynolds number increases (see Figure 4.38).

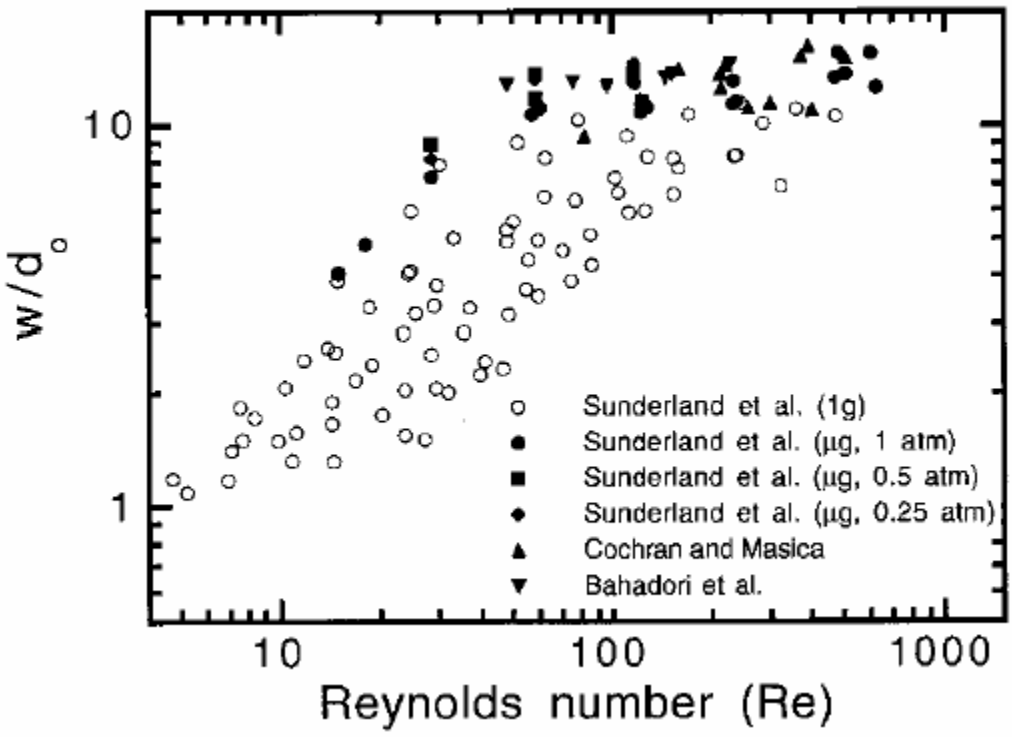

Figure 4.38 Measurements of Flame Width under Normal and Microgravity Conditions at Normal Air Temperature (reproduced from [16])

The data show that, consistent with theoretical predictions, the width is nearly independent of Reynolds number for nonbuoyant conditions, except at low Reynolds numbers, where boundary-layer approximations are invalid. The nonbuoyant width increases slightly with Reynolds number, whereas all aforementioned models predict self-similar flame shapes with no effect from the Reynolds number. This may be due to axial diffusion, not considered in these models, which increases mixing over that seen from radial diffusion alone [66]. This suggestion is supported by the results shown in Figure 4.38, which indicate that the lowest normalized width corresponds to the jet with the lowest Reynolds number, where axial diffusion is most significant. As Reynolds number increases, the normalized width rises asymptotically to a fixed value.

Compared to, normal-gravity flames, that are yellow, microgravity gas jet flames are more red [16, 32], indicating lower blackbody soot temperatures and presumably lower maximum flame temperatures. This occurs because the residence time is larger at microgravity and thus radiative loss effects are greater. Drop tower [22] and space [32] experiments indicate surprisingly large and consistent radiative loss fractions (0.45 – 0.6) under microgravity, as compared to 0.07 – 0.09 at normal gravity, for various fuels, pressures, O2 mole fractions, and flow rates. Thus, the differences in residence time between normal gravity and microgravity result in widely varying characteristics even for flames having nearly the same length.

Lin et al. [64] obtain and analyze the flame length in still gases according to a simple Spalding analysis [11]; their results overproduced in Figure 2.4. Flames in still gases represent near-laminar smoke-point conditions and yield a reasonable

correlation with relatively small scatter effects. Lin and Faeth [12] obtained correlations for coflowing jet flames with air-to-fuel velocities greater than one. This correlation can predict experimental data reasonably well, as shown by the graph in Figure 2.4. They concluded that flame lengths for flames in still and coflowing gases have roughly the ratio of 3/2, with this ratio being relatively independent of the air-to-fuel velocity ratio and the Reynolds number, in accordance with simplified theories. They also presented results for small coflow velocities with air-to-fuel velocity ratios between 0.22 and 0.5 (also shown in Figure 2.4). This figure exhibits strong agreement with earlier measurements for slow, coflowing diffusion flames.

4.5 Comparison of Case II with Case VI

Further experiments are conducted with combustion air preheated to temperatures in the range of 973 K (700^{o}C) to 1073 K (900^{o}C), at a propane-gas flow rate of 0.02 SCFH using a 1-second drop tower. Preparations for the experiments involved turning on the air preheater to generate the desired air-preheat temperature also making a flame at steady state conditions. Results from two specific experiments are reported, providing information on the effect of the temperature of the preheated air upon flame size, shape and color, under both microgravity and normal-gravity conditions. Before dropping the combustion chamber, the video camera was turned on so as to record the flame features in a normal-gravity environment, for comparison. Results are presented for preheated combustion air temperatures of both 700^{o}C and 900^{o}C, under low gravity conditions. These results are presented as sequences of diffusion flame photographs, as shown in Figures 4.39 and 4.40.

The time-sequence photos of the flame during the drop were obtained from video, recorded at 30 frames/sec. The results show that, in both cases, the flames exhibit clear color regions, consisting of an initial blue-colored flame region, followed by a yellow-colored flame region downstream of the burner. The length of the yellow-colored flame region is shown to increase with increasing preheated air temperature – being higher in the 900^{o}C case than in the 700^{o}C case (as can be seen by comparing Figures 4.39 and 4.40). Not only is the yellow region of the flame longer in Figure 4.41, but also a close examination of the entire flame length (blue and yellow regions) reveals that this length is also greater for our 900^{o}C air preheat temperature experiment than it is in the 700^{o}C experiment.

These flame photographs are further analyzed with respect to the total length and width as well as to the length and width of the blue and yellow regions of the flames, across the entire time duration in the microgravity environment. The results for the total length are shown in Figure 4.41. Comparing the flame lengths for the experiments with 700^{o}C and 900^{o}C air preheat in a time range from 0 second to 0.1 second reveals the longer flame at the higher air-preheat temperature. The photographs in Figure 4.42 show the length increase of the flame at 900^{o}C under microgravity conditions. The results for the total width are shown in Figure 4.43. Comparing the flame width for experiments with 700^{o}C and 900^{o}C air preheat over the same time range (0 sec – 0.1 sec) reveals the wider flame at the higher air-preheat temperature.

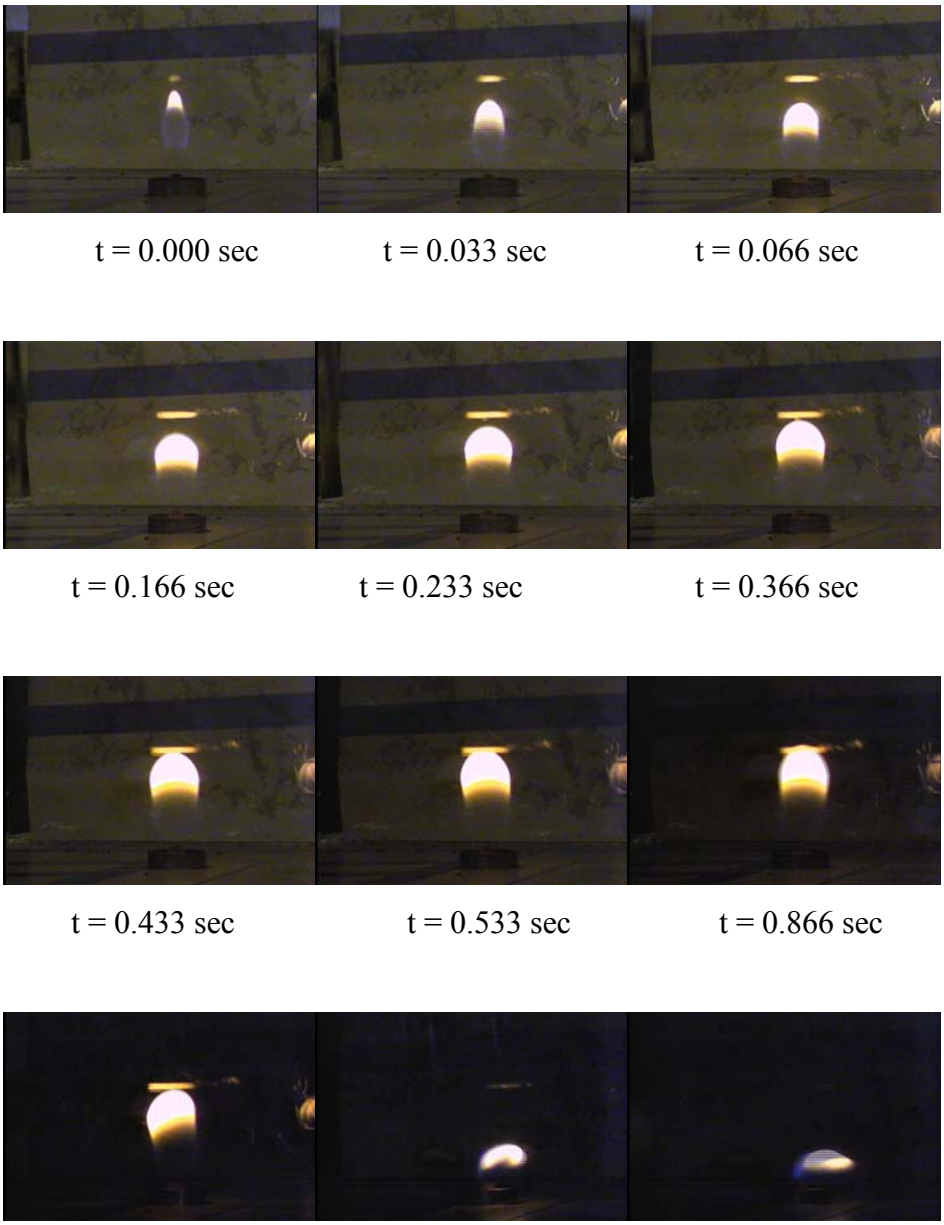

Figure 4.39 Evolutionary Behavior of Flames with 700^{o}C Temperature Combustion Air in Microgravity Condition

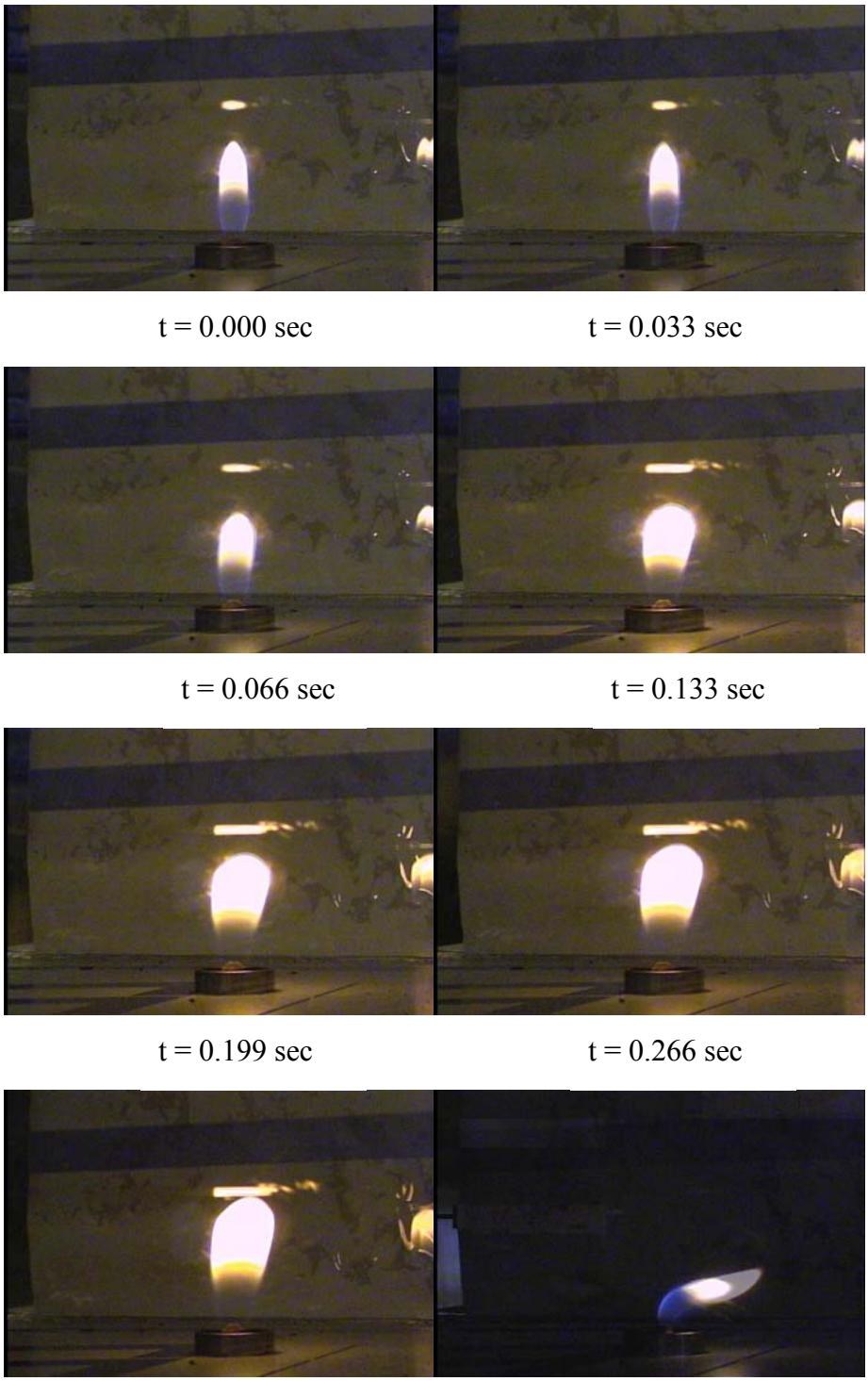

Figure 4.40 Evolutionary Behavior of Flames with 900^{o}C Temperature Combustion Air in Microgravity Condition

The photographs in Figure 4.44 show the width increase of the flame at 900°C under microgravity conditions.

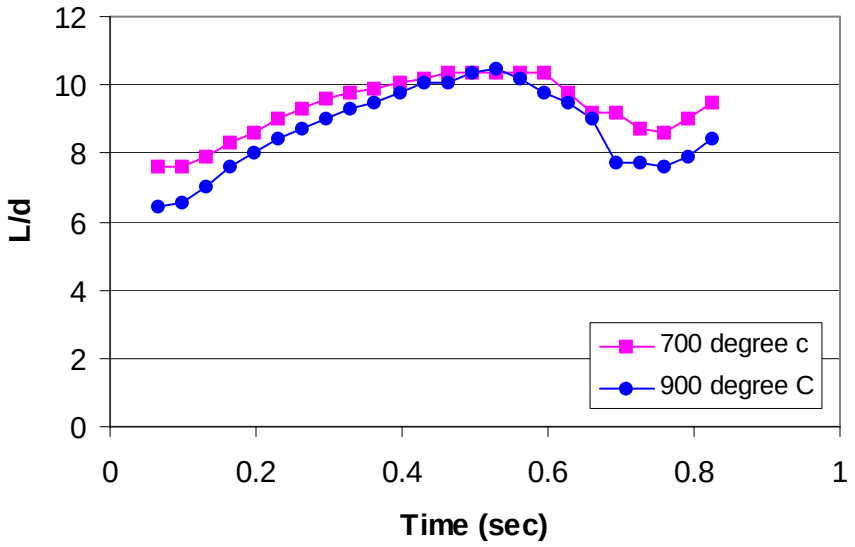

Figure 4.41 Normalized Flame Length Variation during the Microgravity Time Duration

t = 0.000 sec t = 0.233 sec

Figure 4.42 Increase of Flame Length Under Microgravity

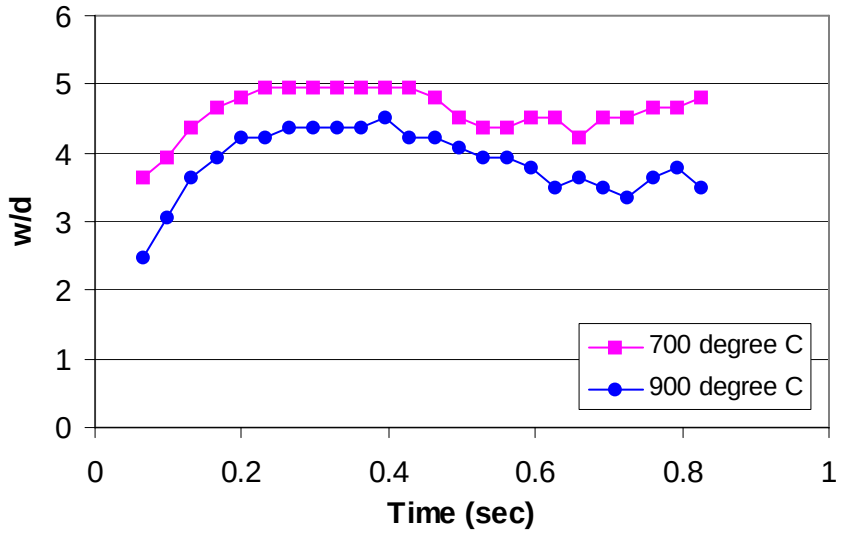

Figure 4.43 Normalized Flame Width Variation during the Microgravity Time Duration

T=0.000 sec T=0.433 sec

Figure 4.44 Increase of Flame Width under Microgravity

A comparison of the blue and yellow regions of the flame for the two experiments under low-gravity conditions is shown in Figures 4.45 and 4.46. At higher preheated air condition, the yellow region of the flame becomes larger and the blue region of the flame becomes smaller. Flames with higher air-preheat temperatures affect the shape more (with regards to their length and width) in the presence of microgravity. These results are in agreement with our studies carried out at normal-gravity conditions. The length of the yellow portion of the flame increases in proportion to the overall flame length at higher preheated combustion air temperature; the blue portion of the flame, however, is found to decreases as well with increasing the combustion air temperature. The photographs in Figure 4.47 compare yellow regions of the flames under normal and low-gravity conditions with 700^{o}C preheated combustion air. Longer residence times and much slower axial velocities under microgravity conditions result in wider flames with a yellowish color.

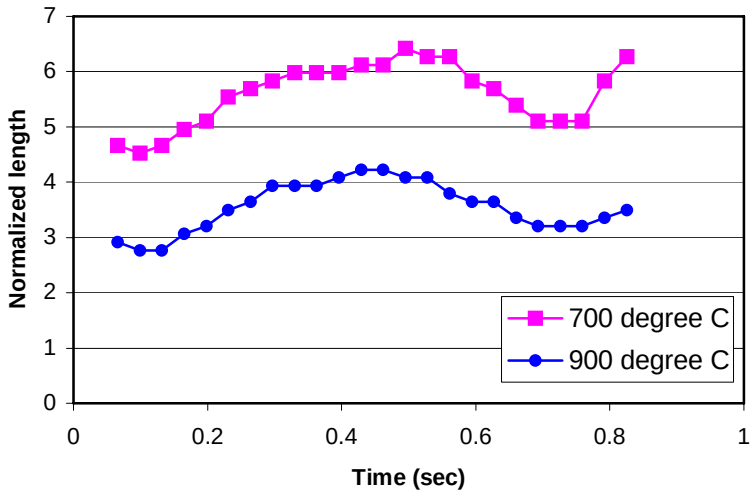

Figure 4.45 Normalized Blue Portion of the Flame Length Variation during the Microgravity Time Duration

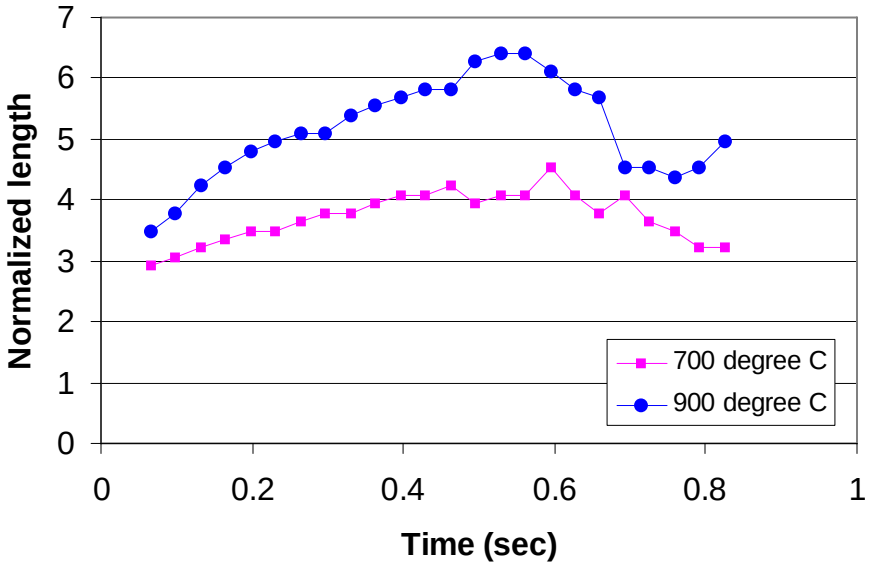

Figure 4.46 Normalized Yellow Portion of the Flame Length Variation during the Microgravity Time Duration

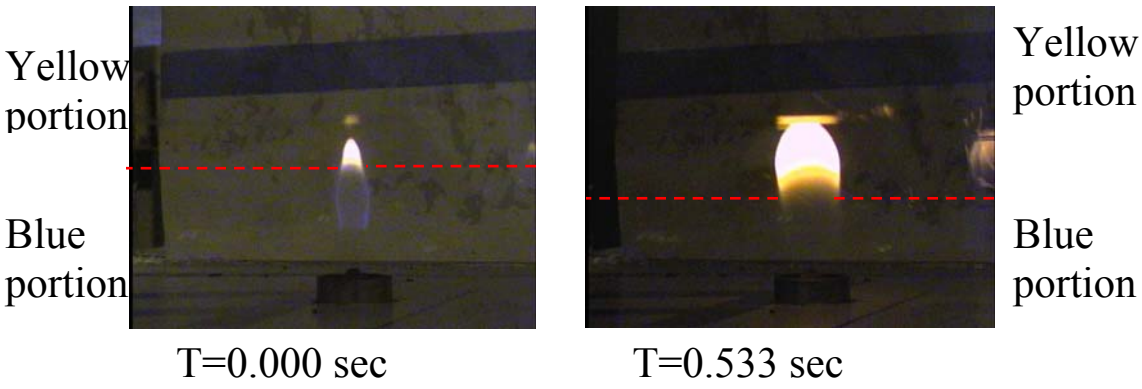

Figure 4.47 Effect of Gravity on Blue and Yellow Portion of the Flame

4.6 Comparison of Case III with Case IV

The data from our drop-tower experiments under low-gravity conditions with preheated combustion air are important for understanding the mechanisms at work in preheated combustion air flames. These results have been compared with the results obtained by Lin and Faeth [12]; who developed correlations representing predictions of coflow diffusion flame length and width at normal-temperature combustion air under low-gravity conditions. The results of this comparison reveal the effect of preheating upon laminar diffusion flames in the absence of buoyancy effects.

Figure 4.48 shows the relative change in flame width and length throughout the duration of our low-gravity experiment (at the condition explained in Table 3.1). Although the flame length and width both increase under microgravity conditions, the change in flame width is more significant than the change in length. For comparison low-gravity calculations of flame length and width using Lin and Faeth [12] correlations for normal temperature air, are shown in Figure 4.49. The fuel flow rate applied for calculation of the predicted flame shape was 78 cc/min (the same flow rate as we use in our experiments). While the trends for the flame length are similar, the predicted width of the flame is significantly wider in our experiments. This observation was also made under normal gravity experiments.

An additional normal-gravity observation (at the condition explained in Table 3.3) examines the effects of preheating upon flame volume; the fuel flowrate was adjusted in order to create a preheated flame that was as tall as its non-preheated counterpart. Figure 4.50 compares the flame structures thus obtained.

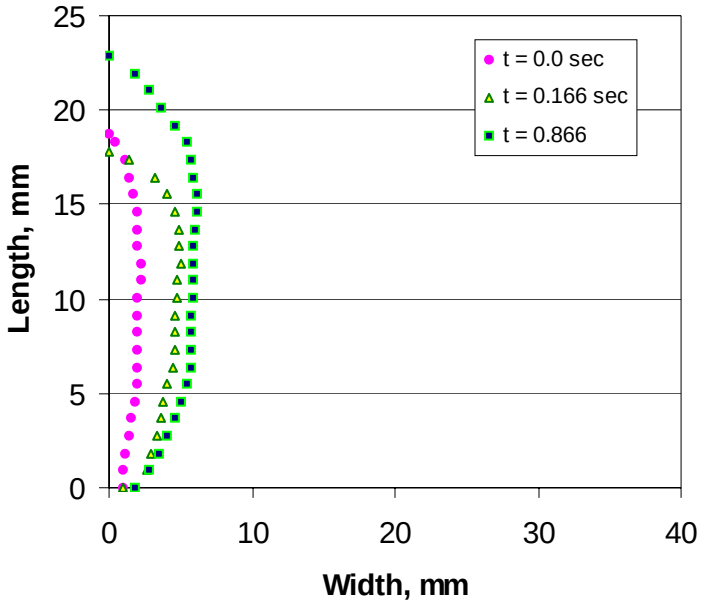

Figure 4.48 Relative Change in Flame Width and Length during the Low Gravity Test Duration

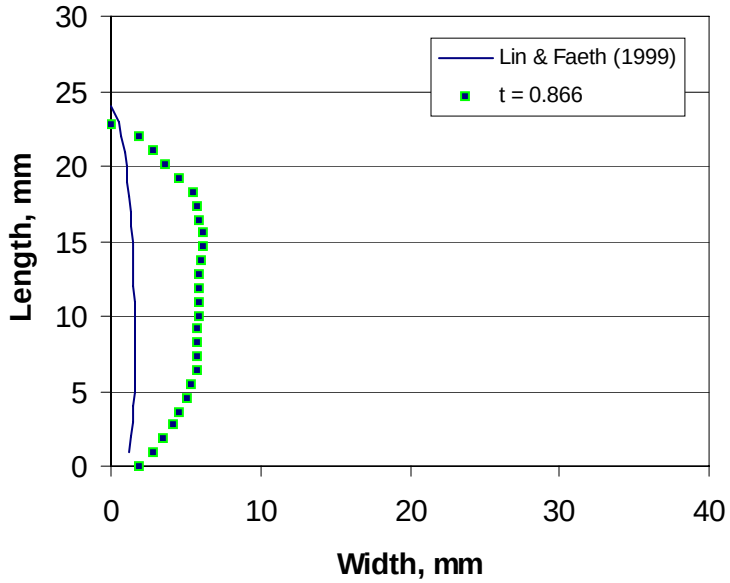

Figure 4.49 Comparison of Laminar Coflow Diffusion Flame Length and Width at Normal Temperature (Lin and Faeth Correlation) and High Temperature (Present Studies Experiment) Under Low Gravity Conditions

Increasing the fuel flow rate increases the energy release per unit volume, thereby compensating for the reduced flame length observed with preheated air in normal-gravity conditions. Although increasing the fuel flowrate produces a preheated combustion air flame of equal height, the width of the preheated combustion air flame remains smaller than that of the normal-temperature flame – the result of increased forces at the higher preheated combustion air temperature flames. Buoyant or momentum forces move the reaction zones radially inward, toward the centerline region of the flame. Higher energy release leads to a higher flame temperature and, presumably, higher NOx production.

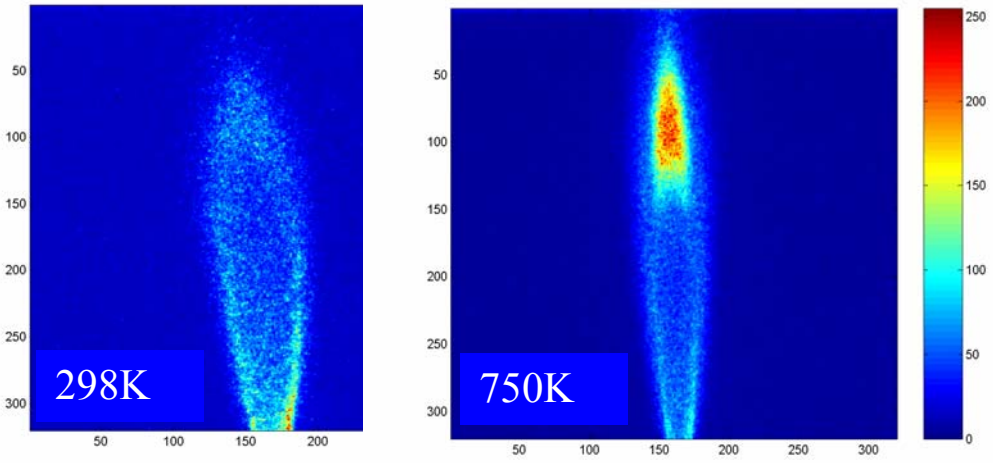

Figure 4.50 The Flames with Equal Length and Different Fuel Flow Rate.

The same observation under low gravity can be seen in Figure 4.49. Figure 4.49 compares the laminar coflow diffusion flame length and width at normal temperature (Lin and Faeth correlation) and high temperature (present studies experiment) under low gravity conditions. Prior to dropping the test rig, typically normal-gravity effects were observed; preheated combustion air diffusion flame

length is smaller than for a normal-air-temperature diffusion flame with the same fuel flow rate. The preheated combustion air flame length during low gravity test duration increased and after 0.166 sec the length of two the flames became equal. Figure 4.50 reveals that unlike the result seen under normal-gravity conditions, preheated combustion air ***increases*** the flame width under low-gravity conditions even more than the low gravity effect alone (i.e. it is well understood the microgravity increases flame length and width at normal-temperature condition air, but we find that preheating the combustion air increases the width even further). In the absence of buoyancy, reaction zones moves radially outwards from the centerline region of the flames even more than for a normal combustion air diffusion flame because of an increased diffusion effect. Fuel diffusion increases with greater temperature, thereby increasing the flame region volume. Thus the energy release intensity decreases, causing a decrease in the flame temperature, and an improvement in NO_x production. To obtain a similar result in a practical setting, one might use inlet air with a low-oxygen content. Flames produced under these conditions also have low energy density and low NOx production, due to their tendency to produce flames that are diffused over a wide area.

Based on the flame Froude number, either momentum-controlled or buoyancy-controlled regimes are responsible for the greater and faster mixing and delivering of oxygen to the flame. The flame Froude number is plotted against preheated combustion air temperature in Figure 4.51, in order to determine whether the flame structure is momentum-controlled or diffusion-controlled. This figure shows that, when the temperature of combustion air is increased, the Froude number

also increases. This indicates that preheating the oxidizer can alter the flame from the buoyancy-dominated regime to the momentum-dominated regime.

In practical, turbulent diffusion flame application, the role of buoyancy is negligible, but the preheated combustion air still causes a decrease in the flame size and an increase in the energy-release intensity. As has been observed through our PIV results, preheated air affects the flow field and enhances mixing. Our results suggest that, to obtain any benefit from the use of preheated combustion air in diffusion flames in practical applications one could use the flow field enhancement, but would need to provide a way to expand the flame zone. For example, one could decrease the oxygen content of the inlet air. In this way, beneficial effects of the changes in flowfield characteristics can be obtained, without the drawbacks of higher flame energy density and NO_x production.

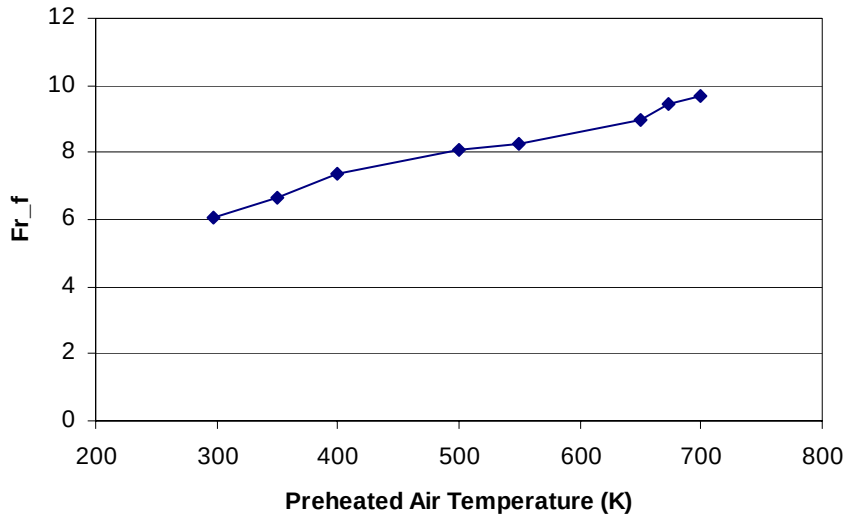

Figure 4.51 Effect of Preheated Combustion Air Temperature on Flame Froude Number

5 Conclusions

A comprehensive investigation of the effects of preheated combustion air on the structure and shape of diffusion flames has been conducted. The objective of this research is to explore how preheated combustion air affects the structure and shape of laminar coflow diffusion flames, and to explain why preheating exhibits such effects. Preheated combustion air is found to influence the flowfield, the thermal and the chemical behavior of the flame. For these studies an experimental facility has been designed and constructed. Innovative diagnostics are employed that enabled both the examination of the details of the combustion process, and its global characteristics. This data is of practical value to science and industry. This investigation represents one of the few, if not the only, study available in the open literature to detail the effects of preheated combustion air on the normal coflow laminar diffusion flame, flow field, chemistry and thermal behavior. It is also the first study to investigate a preheated, low gravity flame. The following sections summarize and emphasize the noteworthy considerations, observations and contributions made in the principle areas of this investigation.

Comparison of case I and Case III

- Under normal-gravity conditions, preheated combustion air causes shorter flame length and width as compared to normal-temperature combustion air. The results in this study show that increasing preheated combustion air temperature by about 400 K causes a 37.1% reduction in the flame length.

- Increasing the preheated air temperature results in a larger yellow region and a smaller blue region within the flame. The faster and earlier decomposition of the centerline fuel is responsible for increasing the soot yield and the consequent increase in the yellow region of the flame, implying a heat release improvement in the laminar diffusion flame.
- Increasing the preheated air temperature results in a significant amount of soot in the lower portion of the flame and, consequently, a more luminous flame.
- The radical emission distributions within the flame support the visual observations of the shortening and narrowing of the flame as the temperature of the preheated combustion air increases, as well as the redistribution of soot formation upstream toward the fuel nozzle.
- CH radical distribution, representing the stoichiometric flame front, is observed to move inward toward the centerline of the flame when the preheat temperature of the inlet air increased. The results in this study show that a 400K increase in the preheated air temperature increases the CH concentration of the flame by ~83.3%. CH radicals also show the location of maximum flame temperature, which is located at the center and downstream of the preheated combustion air diffusion flame. As a marker of heat release, CH radical intensities significantly increase, showing that the preheated combustion air increases the rate of chemical reactions.
- Increasing preheated combustion air temperature results in more compact and intense C2 radical regions. This again implies that the region in the flame

where soot is formed is affected by the preheat temperature. The results The results in this study show that a 352K increase in preheated air temperature increases the C_2 concentration of the flame by ~60%.

- Changes in the C2 and CH radical distributions (due to the increase in preheat temperature) are found to explain the changes in the region of soot formation. Increasing the rate of the chemical reactions, and reducing the flame volume results in a higher flame temperature. Faster and earlier fuel decomposition is therefore associated with higher flame temperatures, causing higher soot yields at suitable fuel fraction and temperature limits and consequently providing higher soot concentrations at the centerline and downstream of the preheated combustion air diffusion flame.
- Vibrational temperature distributions of the C2 vibrational bands of the laminar diffusion flames suggest that enhanced reactions in the flame zones result from increases in the preheated combustion air temperature. This observation supports results obtained from three-dimensional CH and C2 radical concentration measurements. The increased preheat-temperature causes the fuel to begin decomposition closer to the burner exit, due to a general increase in flame temperature. The results in this study show that raising preheated combustion air temperature by 352K increases the peak temperature of the flame by ~24.6% as a result of the increased reaction rate.
- Increasing the preheated combustion air temperature results in higher energy release inside the flame (based on CH emission intensities) and higher axial velocities (PIV results). The results in this study show that By increasing the

preheated combustion air from 25 to 80 ºC, the maximum velocity in the flame increases by about 26%.

- The enhanced reaction rate significantly increases the soot content of the diffusion flame at the centerline and in the downstream region of the flame. Although the flame temperature profile shows a maximum in the annular region located at the upper part of the flame, the maximum temperature contours do not converge to the axis in the upper part of the flame. This is due to the radiation cooling of the soot. Other researchers have observed similar tendencies in laminar diffusion flames as the combustion air temperature is increased.
- Preheated combustion air allows for stronger mixing in the shear layer region as reflected by high CH radical intensities and high strain rates being located close to the centerline of the flame.
- The enhancing mixing of preheated combustion air diffusion flames is the result of increased vorticity and axial strain rates.

Comparison of prhehated case I with case III

- Preheated combustion air causes a longer flame length, wider flame width and larger yellow region of the flame under low-gravity conditions.
- Increasing the preheated combustion air temperature affects the width of the flame more than the length, in a low gravity environment.

Comparison of case III with case IV

- When compared to normal gravity, microgravity increases the flame volume, although the increase in flame length is similar for both normal and preheated combustion air, the amount of increase in width under preheated combustion conditions is significantly greater than the increase in width using normal temperature combustion air.
- Under normal gravity conditions, preheated air flames are narrower than normal-temperature air flames. Under microgravity conditions, the opposite is true: preheated air flames are wider than normal-temperature flames.
- The expansion of the flame under microgravity conditions indicates a lower flame temperature and a lower NO_x production within the flames. This effect can be reproduced under normal gravity conditions by reducing the oxygen content of the inlet air.

Future Recommendations

Several recommendations are offered for future work.

- Instantaneous measurements of velocity and CH profiles are suggested. In this study it has been noticed that the CH layer and the flow, which is represented by the velocity and strain rate field, interact with each other. The correlation between the position of the CH layer and stoichiometric velocity contour provide a good diffusion flame characteristic to study the effect of preheated combustion air on laminar diffusion flames in more detail.

- It has been noticed that the optical emission signatures from combustion experiments provide a convenient chemically based diagnostic. These techniques could be applied in microgravity, if experimental obstacles are first overcome.
- To date, measurements of laminar diffusion flames under microgravity conditions have included shape, color, temperature, soot properties, radiative emissions and compositions. Technological barriers associated with microgravity experimentation have largely precluded the measurement of flow fields in diffusion flame. In future work, applying PIV diagnostics to measure the flow field characteristics of coflow diffusion flames under microgravity conditions is suggested.
- An examination of the effects of preheated combustion air on propane-air diffusion flame structure using sampling and gas chromatography is possible. Species concentrations measurements along with PIV and optical emission spectroscopic data can provide a set of valuable data to better understanding the detailed effect of preheated air on reactions in the flame.
- Examination of the effect of preheated combustion air on laminar coflow diffusion flames is suggested using either higher drop tower or aircraft facilities to provide longer-duration low gravity.
- Examination of the effect of both of preheated combustion air and low oxygen concentration on laminar coflow diffusion flame is suggested using present diagnostics.

Appendices

Appendix A: Design of the Experimental Facility for Use in NASA 2.2 second Drop Tower

The purpose of this chapter is to (a) provide details for all components in the High Temperature Air Combustion (HiTAC) Rig. (b) Assembly of the various components for the designed rig. using high temperature combustion air under drop tower microgravity conditions, and (c) instructions of how to conduct the experiment. Methane and propane at room temperature will be used as the fuel.

The test objective is to determine the effect of air preheat temperature on flame characteristics in microgravity conditions and obtain information on the features of gas flames using high temperature combustion air. Also the data will be compared with that obtained under normal gravity conditions. The experiments will be conducted with the preheated air temperature approximately from 900°C to 1100°C.

In brief we will conduct experiments at 1g and micro-g conditions to determine the effect of air-preheat temperature on the flame combustion characteristics. Specifically we wish to determine the flame volume size and shape, strain rate, flame signatures for CH, C2 and OH as a function of air-preheat temperature, O2 concentration in air (from 21% down to 1%) and fuel-air equivalence ratio.

This document on the design of the rig includes Rig Description, Assembling Procedure, Operational Instructions and Data acquisition and data analysis system.

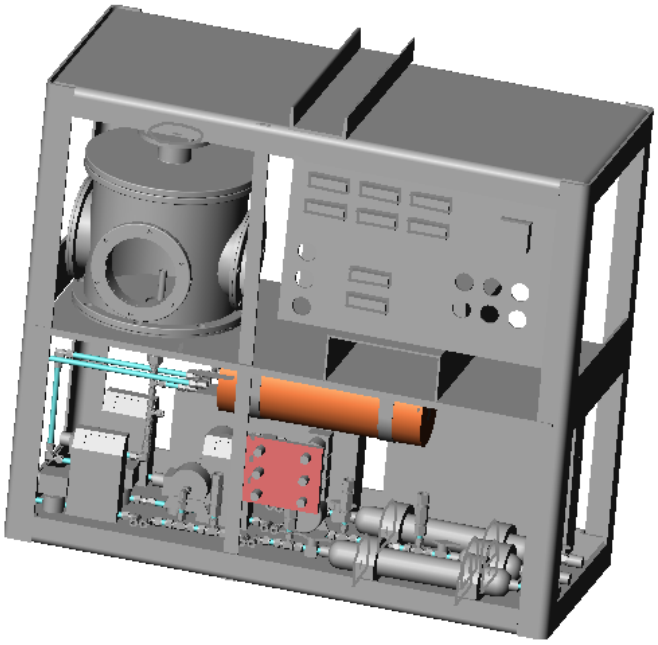

Figure A.1 General View of 2.2 Second Drop Tower Rig

A.1.1 General View of Drop Tower Rig

The drop tower rig consists of several components. The components are shown in Figure A.1 and the list of components is given in Table A.1. In this chapter the drop tower for HiTAC is divided into several parts. These parts are combustion chamber, fuel line, air line, coolant line, image and data acquisition system, electrical and electronic control system. Generally, hardware should be integrated into the metal frame to form the experiment package. Prior to inserting components into the frame, the components, such as combustion chamber, are pre-assembled and then inserted into frame. Specification and circumstance of assembling for each part will be explained below

Table A.1- List of Main Components of Drop Tower Rig

No.	Components	No	Components
1	Frame	8	Battery Pack
2	Combustion Chamber	9	Cylinders
3	Preheater	10	Mass Flow Controller
4	Control Panel		
5	CCD Cameras		
6	Lenses		
7	CCD Support		

A.1.1.1 Frame

The layout of the frame is given below in Figure A.2 (dimensions are in mm).

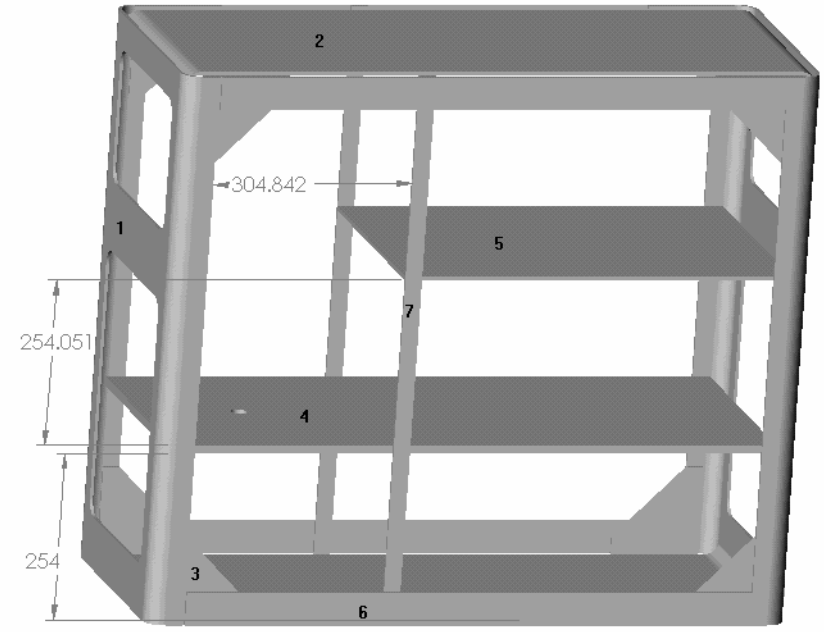

Figure A.2. Frame

A.1.1.2 Combustion Chamber

Combustion chamber (Figure A.3), to be assembled by UMCP, is made of stainless steel with four optical view ports placed on the circumference at 90^{o} apart. This combustion chamber will be operated at normal atmospheric pressure. There is a vent at the top of the chamber and there is a hot wire igniter inside the chamber. Burner is inserted into the chamber from the bottom plate of combustion chamber. A copper hemispherical shape copper block heat sink is placed inside at the top and of the chamber. This copper block absorbs the heat evolved from the burner so that the temperature at the exit from the chamber is low. The combustion chamber is operated at one atmosphere, so that there is no issue on safe operation of the chamber since it will not be operated at high pressure. (The detail of every component is put in Appendix at the end). The total components of combustion chamber are:

- Main Body
- Optical View Ports
- Top Plate
- Bottom Plate
- Igniter
- Burner
- Vent
- Heat Sink

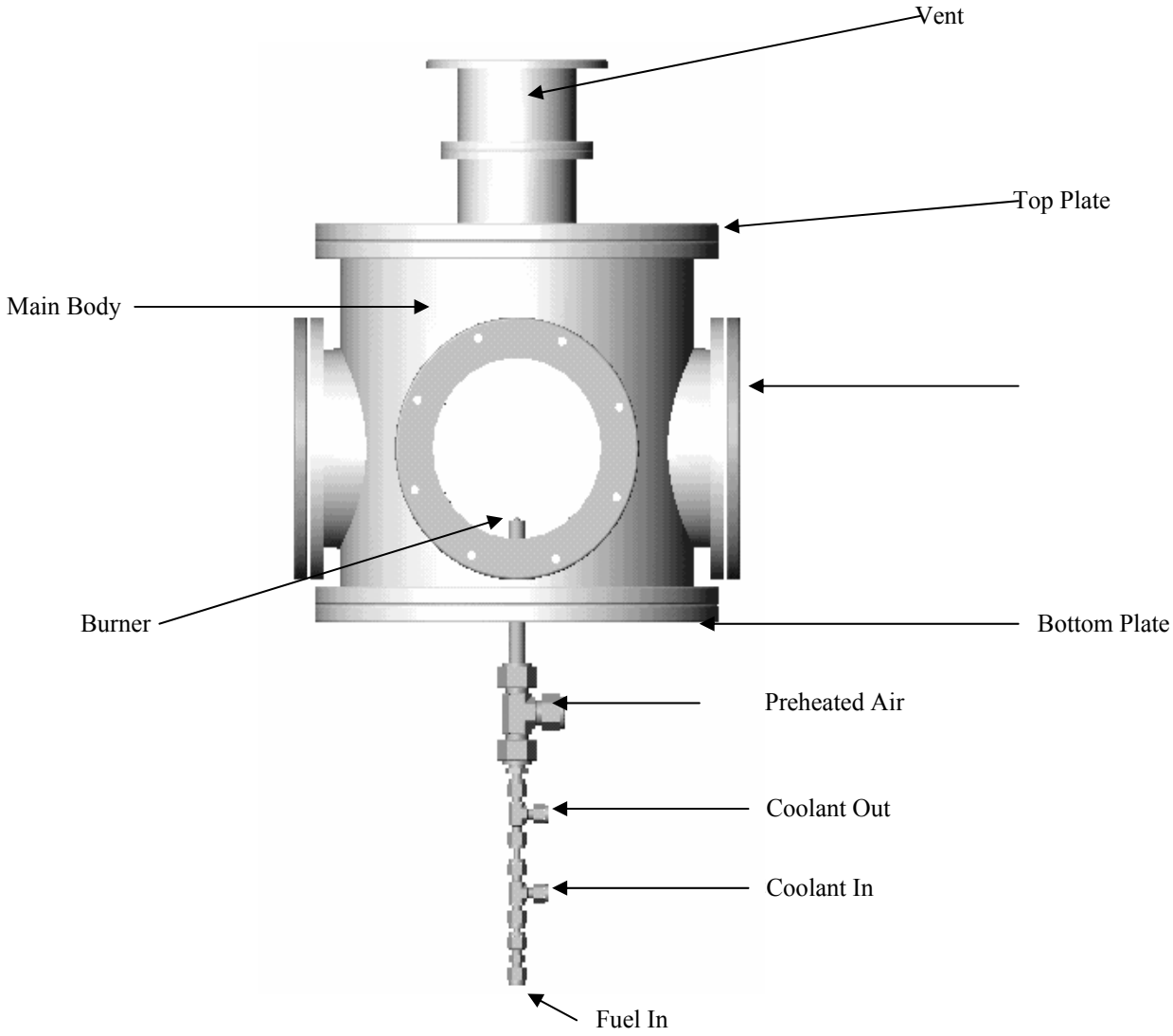

Figure A.3 Combustion Chamber

Main Body

The geometry and dimension of chamber's main body is given below in Figures A.4 and A.5:

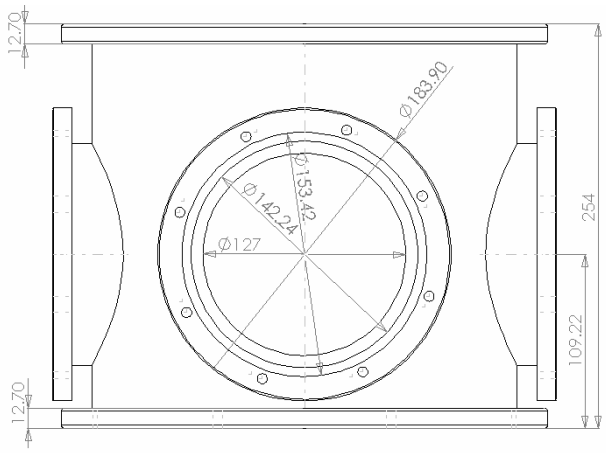

Figure A.4. Front View of Main Body of Combustion Chamber

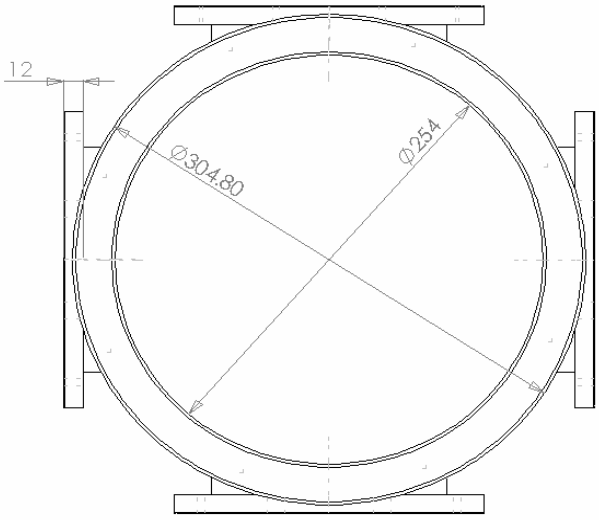

Figure A.5 Top View of Main Body Combustion Chamber

Flange of Optical Window

The details of flange of optical window (all four windows are same in size) are given as the Figure A.6 below. Four quartz glass having a diameter of 153.42 mm and thickness of 12.5 mm is held with the flange shown in Figure A.7.1 and Figure A.7.2.

Figure A.6 3-D Shape of Flange

Figure A.7.1 Flange of Optical Window- Front View

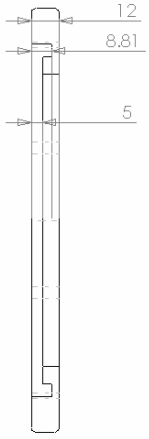

Figure A.7.2 Flange of Optical Window- Side View

Top plate

The details of top plate and vent are illustrated in Figure A.8 below.

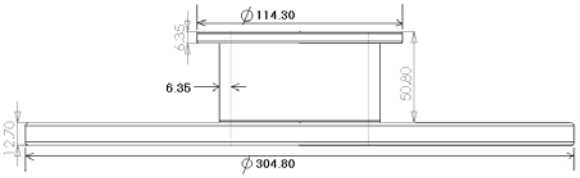

Figure A.8.1 Top Plate-Front View

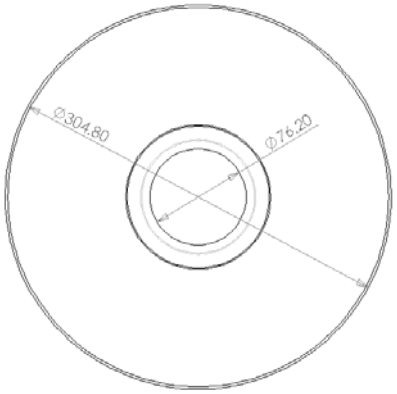

Figure A.8.2 Top Plate and-Top View

Bottom plate

The details of bottom plate are illustrated in Figure A.9 below.

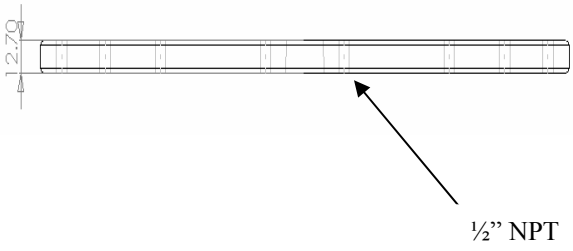

Figure A.9.1 Bottom Plate-Side View

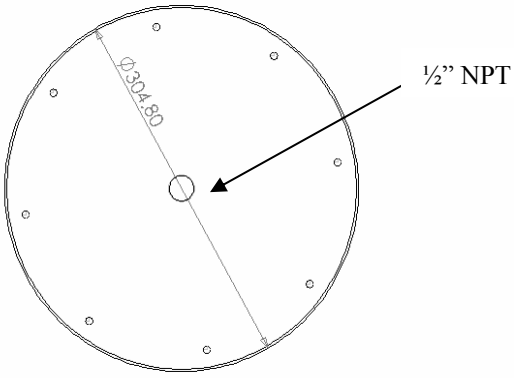

Figure A.9.2 Bottom Plate-Top View

Igniter

Igniter (Figure A.10) contains of a vertical plate having a solenoid attached to a metal support. The igniter element consists of hot-wire element. The leads for this igniter pass through the ceramic tube. This tube is then cased in a metal tube, by pushing the igniter on the control panel, both of solenoid and hot wire position above the burner. After igniting the flame, the igniter reverts back to its original position. The specifications of igniter components are given in Table A.2.

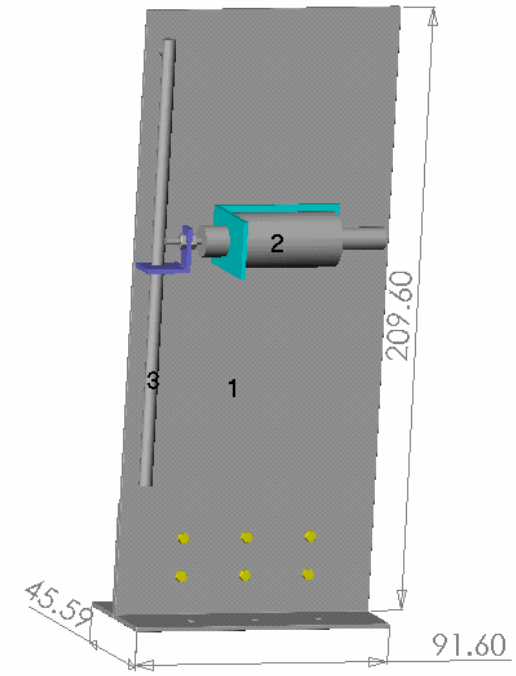

Figure A.10 Igniter

The sketch of Part 3 (Ignition Part) is given below:

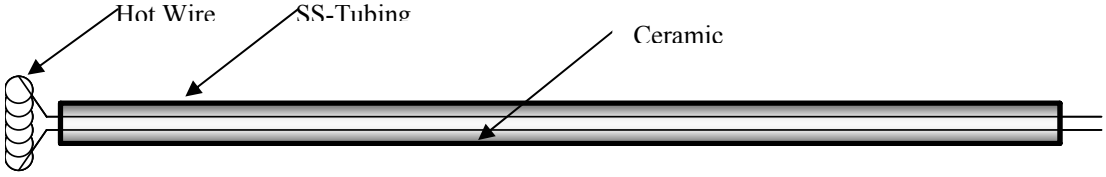

Figure A.11 Sketch of Ignition Parts

Table A.2 Specifications of Igniter Components

	Components	Dimension (mm)		
1	Stainless Steel Bracket	45.6X91.6X209.6 (WXDXH)		
2	DC Voltage Cylindrical Push Solenoid	Solenoid	Push Rod	
			Dia. (mm)	Length (mm)
		19.05X38.1	2.1	26.187
3	Ignition Parts	Stainless Steel Tubing	O.D (mm) 4.575	
			I.D (mm) 3.575	
			Length (mm) 145	
		Ceramic Tubing	Dia. (mm) 3.175 Length (mm) 155	
		Hot Wire	Kanthal AF Wire, 24 Gage	

Burner

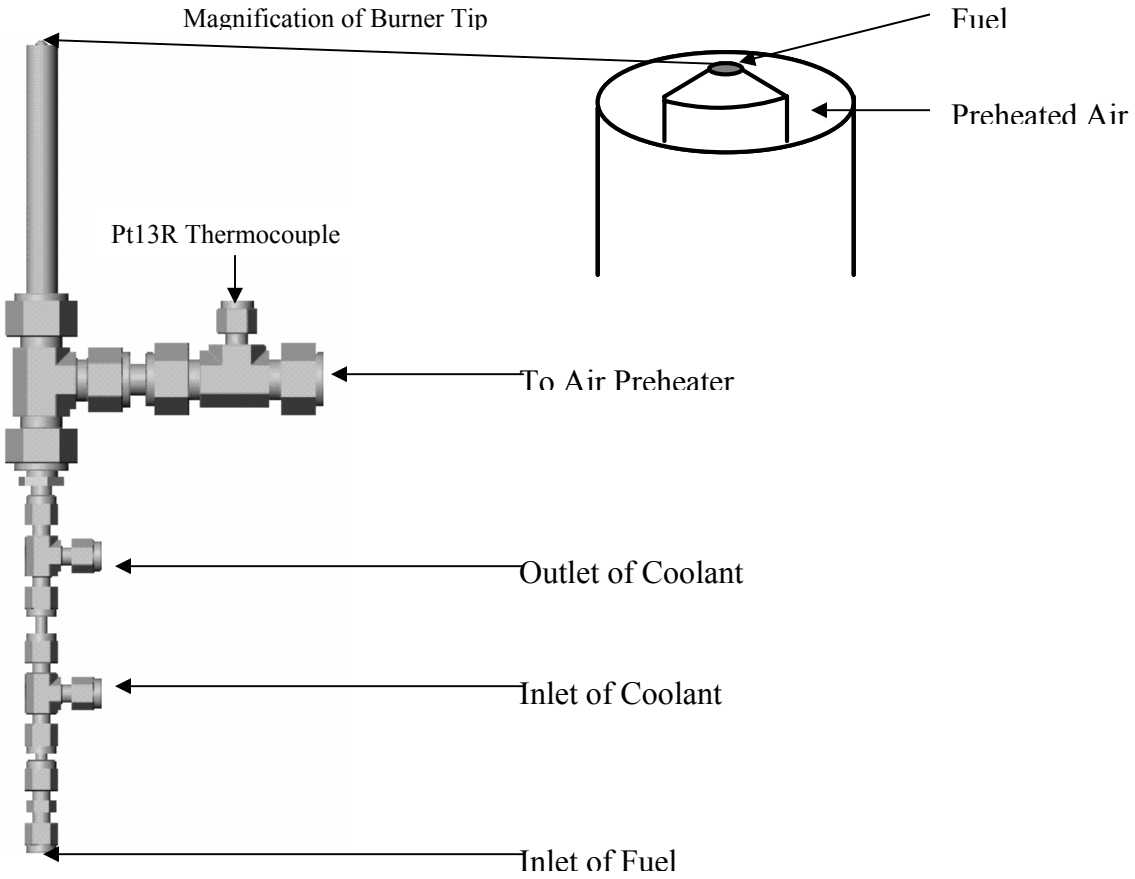

Figure A.12 Burner

The burner provides a diffusion type flame. The burner (Figure A.12) is made of Stainless steel and all dimensions are listed in the Tables A.3 and A.2.

Table A.3 Specifications of the Components for the Burner

Description	Size (mm)
ID of outlet fuel nozzle	0.6858
OD of outlet fuel nozzle	4.7625
ID of outlet air nozzle	10.7
OD of outlet air nozzle	12.7
Thermocouple Pt13R	Dia. of Tip: 0.5

Table A.4 Description of Gas Port

Gas Port	Supplier
Air Port, Union Tee SS-810-3-8-4	Swagelok
Coolant Port, Union Tee SS-300-3 (2 pieces)	Swagelok
Fuel Port, Union SS-300-6	Swagelok
Stainless Steel Tubing	
Reducing union SS-400-6-3, to transfer 3/16" Swagelok to ¼"	Swagelok

Vent

The geometry and dimension of the vent is showed below in Figure A.13:

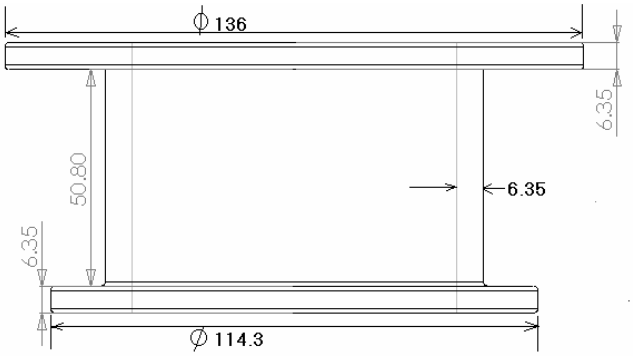

Figure A.13.1 Vent-Side View

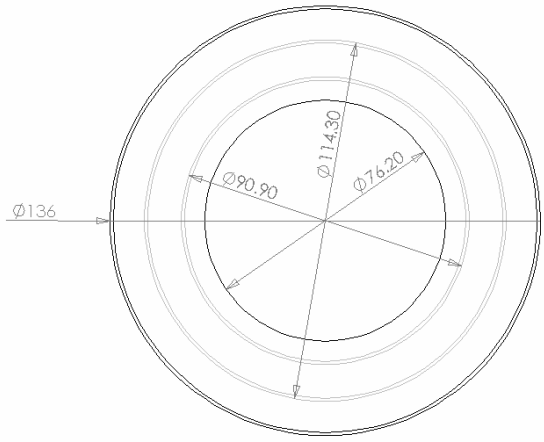

Figure A.13.2 Vent-Top View

Heat sink

In order to reduce the temperature of the exhausted air, a copper block heat sink is used. The location of this heat sink is given in Figure A.14. The shape of heat sink is like a hemisphere. Some air channels are made in this heat sink in order to enhance the heat transfer between the hot gases and the heat sink. While the exhaust gas passes through the holes, heat will be transferred from the gas to the heat sink. The heat sink is made of copper, and it has 8 stubs and nuts for attaching and adjusting it to the top plate of combustion chamber. The shape and dimension of heat sink is so selected that it is not seen through the optical windows of the combustion chamber. The detail specifications of heat sink are given in Figure A.14 below:

In order to obtain these dimensions some engineering calculations have been made. The operational conditions and the assumptions are given below:

ID of outlet of air pipe in burner: 10.7 mm

OD of outlet of fuel pipe in burner: 4.57 mm

Diameter of fuel nozzle: 0.69 mm

Velocity of preheated air: 0.047~0.14 m/s

We assume preheated airflows with 1200°C around a semi-sphere without considering channels on it. Thermo-physical properties of air at 1200 °C and copper are given from thermodynamic table:

$\upsilon_a = 9.865 \times 10^{-5} m^2 / s$

$k_a = 0.0627287 W / m \cdot k$

$k_{cu} = 346 W / m \cdot k$

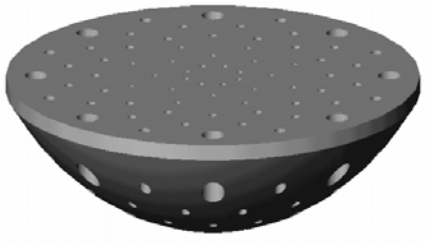

Figure A.14.1 3D View of Heat Sink

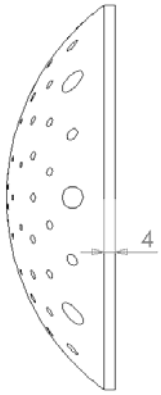

Figure A.14.2 Side View of Heat Sink

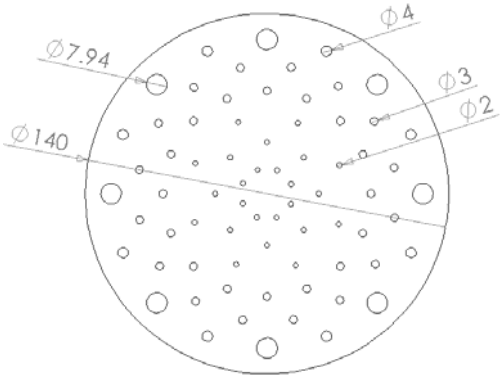

Figure A.14.3 Top View of Heat Sink

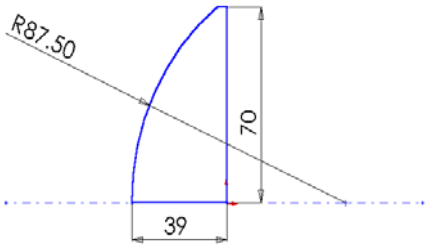

Figure A.14.4 Sketch of Revolved Body

Here, υ_a is dynamic viscosity of air, k_a is conduction heat transfer coefficient of air, and k_{cu} is conduction heat transfer coefficient of copper.

Then, it can be obtained that:

$$\mathrm{Re} = 601$$

From the formula of sphere:

$$\bar{h} = \frac{k_a}{D}(0.37)(R_e)^{0.6} = 7.7W/m^2 \cdot k \qquad \text{(A.1)}$$

Biot number should be obtained in order to calculate the temperature of heat sink surface as a function of time. If Biot number is enough low, lumped method can be sued. For calculating Biot number, characteristic length is needed with knowing the geometry of heat sink.

$$L = \frac{V}{A} = 0.04345m \qquad \text{(A.2)}$$

$$B_i = \frac{\bar{h}L}{k} = 9.67 \times 10^{-4} \qquad \text{(A.3)}$$

So we can use lumped method.

$$\frac{T(t) - T_\infty}{T_s - T_\infty} = e^{-(B_i \cdot F_o)} \qquad \text{(A.4)}$$

The results are given in Figure A.15. They show that as the exhausted gas passes, the temperature of heat sink increases. These results show that after five minutes, the temperature will reach to 54.86°C and after 10 minutes it reaches 83.95°C. However, the heat transfer rate will be reduced, see below in Figure A.16.

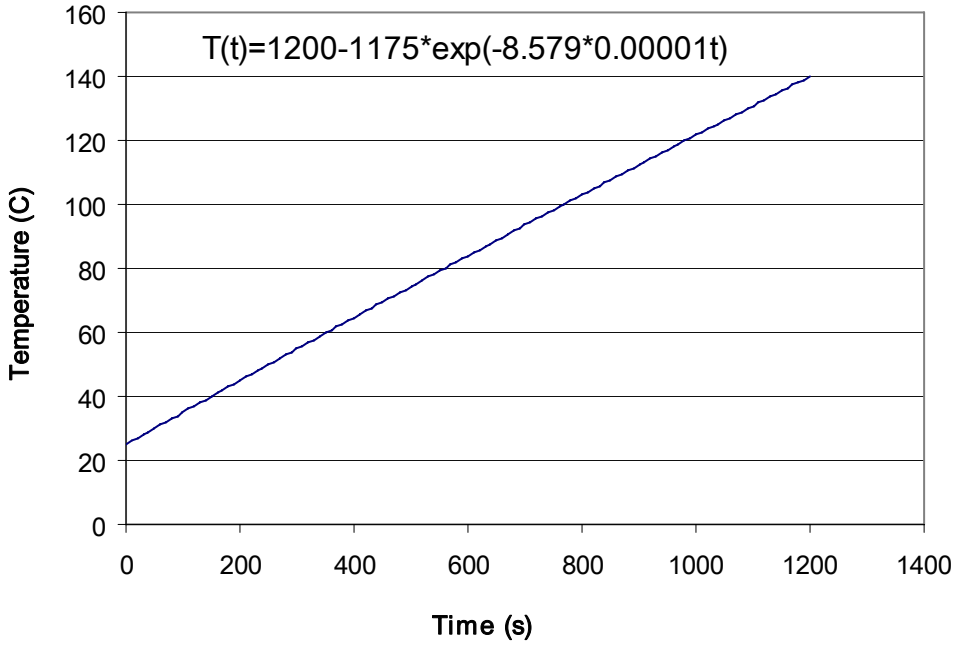

Figure A.15 Heat Sink Temperature vs Time

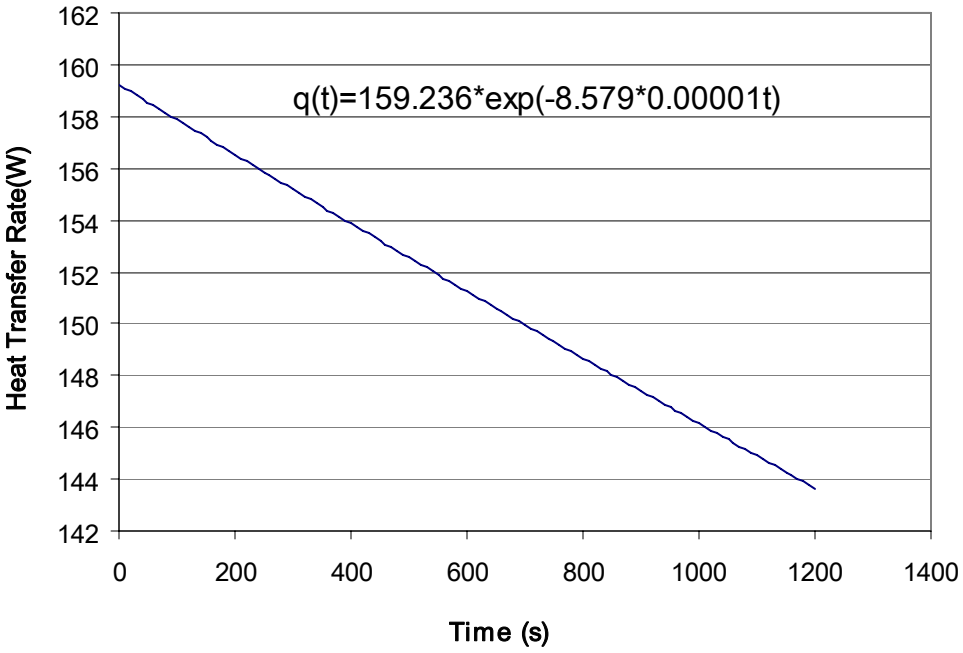

Figure A.16 Heat Sink Heat Transfer Rate vs Time

A.1.1.3 Assembling combustion chamber

One of the important considerations for the assembly of combustion chamber is proper location and adjustment of the igniter. When igniter is turned on, hot wire should be on the top of burner. Another important issue is to adjust the position of burner in combustion chamber so that flame can be seen easily and clearly from the windows of the combustion chamber.

Attaching Bottom Plate

First, the bottom plate of combustion chamber should be attached to the main body, as the Figure A.17 below:

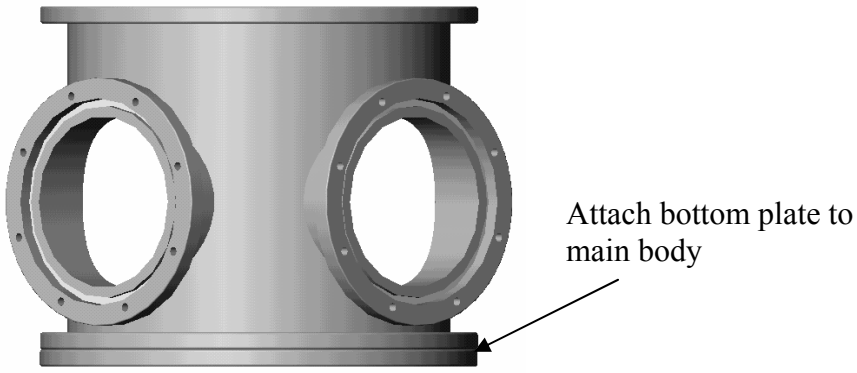

Figure A.17 Attaching Bottom Plate to Main Body

Attaching the Igniter Assembly

Igniter should be attached on the bottom plate with nuts and bolts. It should be noted that hot wire must be on the top of the burner when solenoid is turned on. And the position details are illustrated as Figure A.18 below:

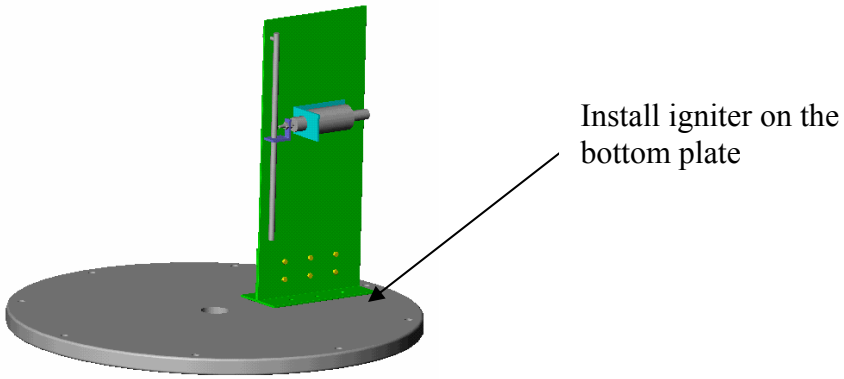

Figure A.18 Attaching Igniter

Attaching the Burner

Burner should be installed in the center of bottom plate in combustion chamber by a male connector (Swagelok SS-1010-1-12). The assembled burner and igniter as well as the dimensions of the burner above plate are given below in Figure A.19.

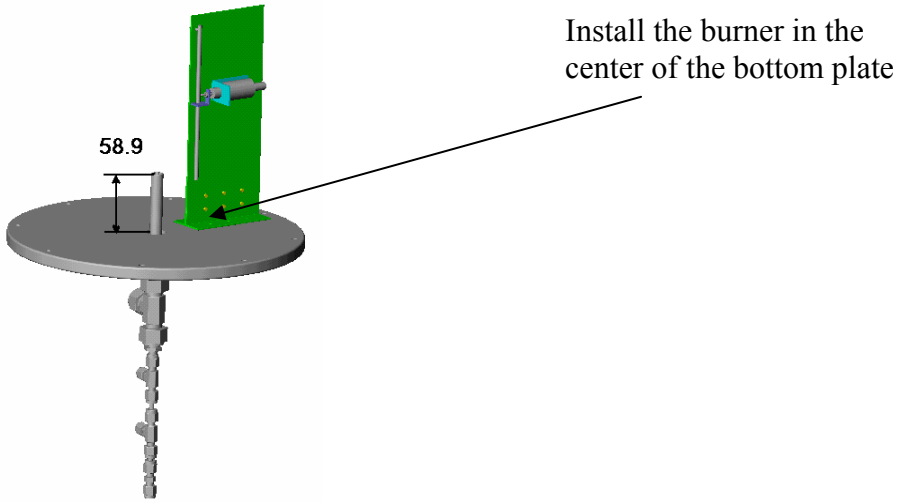

Figure A.19 Attaching the Burner in the Bottom Plate

Attaching Flange of Optical Window

First, place the O-ring in the grove of the flange. Quartz glass with thickness of half inch can be put above the O-ring. The glass is fixed with a flange. The screws hold the glass in position to the chamber.

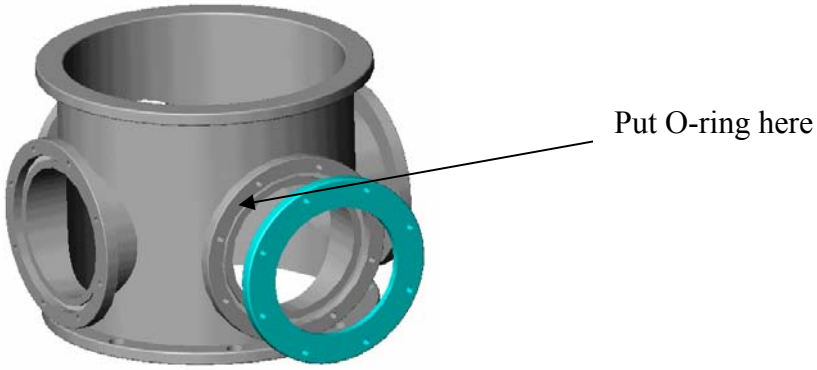

Figure A.20 Attaching Flange of Optical Window

Attaching Upper Plate

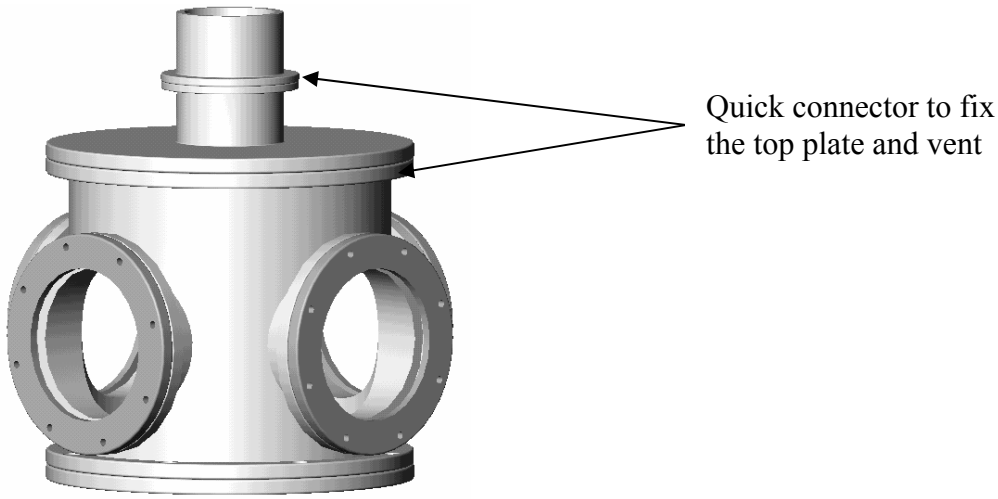

Figure A.21 Attaching Upper Plate

Upper plate should be installed on the main body of chamber by quick connector. As can be seen in the Figure A.21, a vent is also attached to the top plate by quick connector, through which the reaction gas can leave the chamber. Then another extension rubber pipe is connected with the vent. A copper block heat exchanger is placed just upstream of the top vent.

Attaching Heat Sink to Top Plate

The heat sink is fixed on the top plate by 8 stubs and nuts. Between the heat sink and top plate are spacers, which are used to keep the distance between top plate and heat sink as 5 mm. The full assembly is given in Figure A.23. The dimension of the components are given in Table A.5:

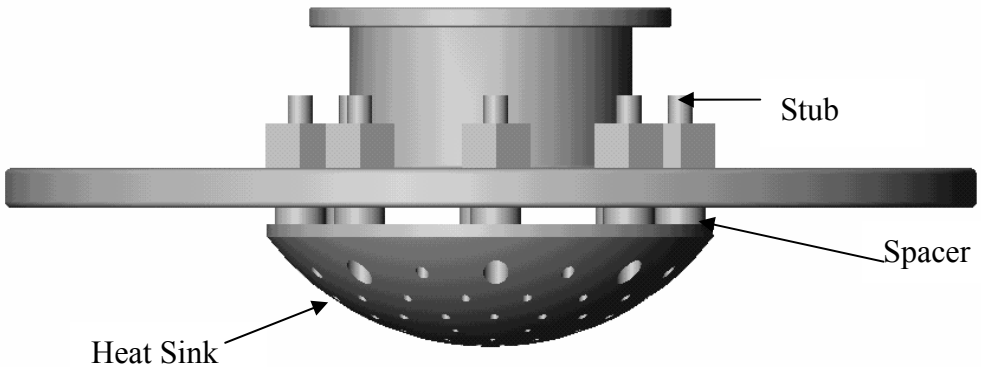

Figure A.22 Assembly of Top Plate and Heat Sink

Table A.5 The Dimension of the Parts in Assembly of Top Plate and Heat Sink

Name	Dimension (mm)
Spacer (8 pieces)	ID: 8 OD: 16 Thickness: 5
Stub (8 pieces)	Dia.: 7.9375 Length: 50.8
Nut (8 pieces)	Side Distance: 14.2875 Thickness: 7.9375

The Assembly of Vent and Fan

To reduce the temperature of exhausted gas, a fan is used to mix hot exhaust gases with the surrounding air. The specifications of the fan chosen are given below:

Table A.6 Specification of the Fan

Fan Size	92 mm sq.
Fan Depth	25.4 mm
Mounting Center	82.55 mm
Flow Rate	45 SCFM
Power	24 VDC/0.1Amp
Manufacture	McMaster-Carr

The assembly of fan and vent is given as the Figure A.23. The cooling fan is fixed to vent by 4 long bolts. Also 4 spacers (25.4 mm long each) are also applied to keep the distance between fan and vent. Temperature measurement of combustion product without and with cooling fan is presented below Figure A.24.

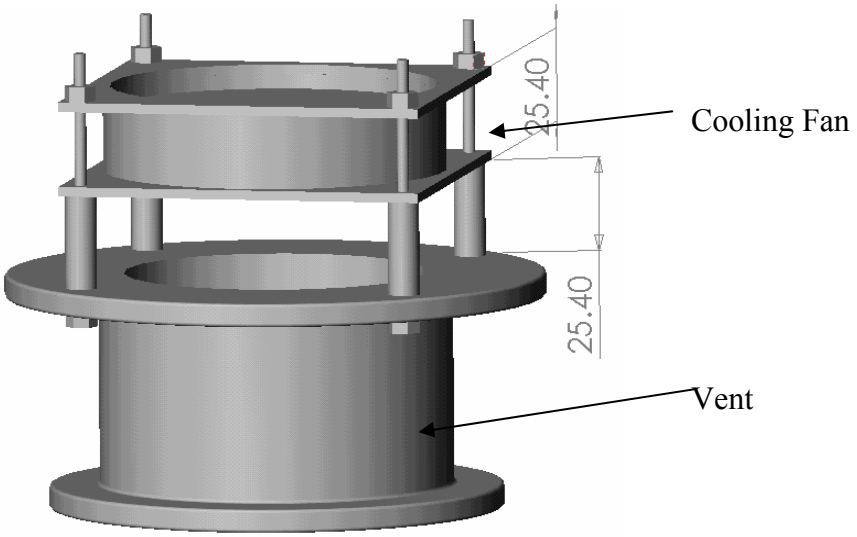

Figure A.23 Assembly of Fan and Vent

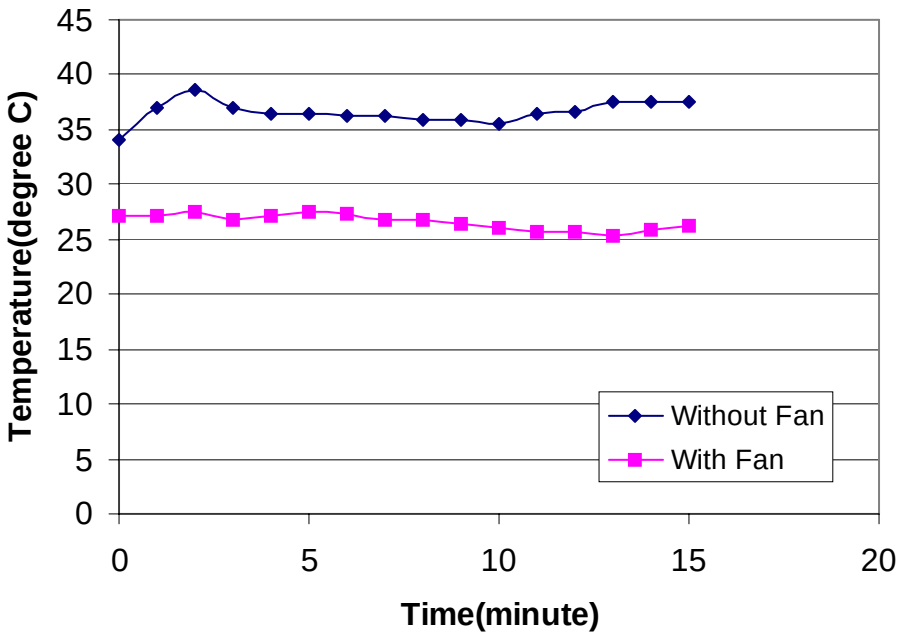

Figure A.24 Combustion Product Temperature Before and After Cooling Fan

A.1.2 Pipelines

A.1.2.1 Air Line

Most of the components for the air line are the same as that for fuel and coolant (CO_2) lines. However, there is some difference in the air line, such as, air preheater in the air line. For preheating the incoming air, we use an electrical air preheater. The incoming air is heated by an electrical element (hot wire). All the pipes are SS. Relief Valve 14 is set at 25 psi to assure the safety of the plumbing line. The upstream pressure in the air line is nominally set in the range of 3 to 5 psig on the pressure gauge in the plumbing line.

A schematic diagram of the plumbing for the air (and also the fuel and coolant) line is given in Appendix 1 (for clarity the older plumbing line is left below as this provides easy reference to the part number).

Air Preheater

The main body of preheater is the stainless steel tubing, which houses the ceramic tube and the heating element (hot wire). The power supply for heating the air can be varied by a variable DC/DC converter. The power supply input for DC/DC converter is 48 VDC, which can be obtained by connecting two 24VDC batteries. Here we have assumed that the batteries have 22 VDC available for use over long time operation of the battery packs. The components of the preheater and its section view are shown below in Figures A.25 and A.26.

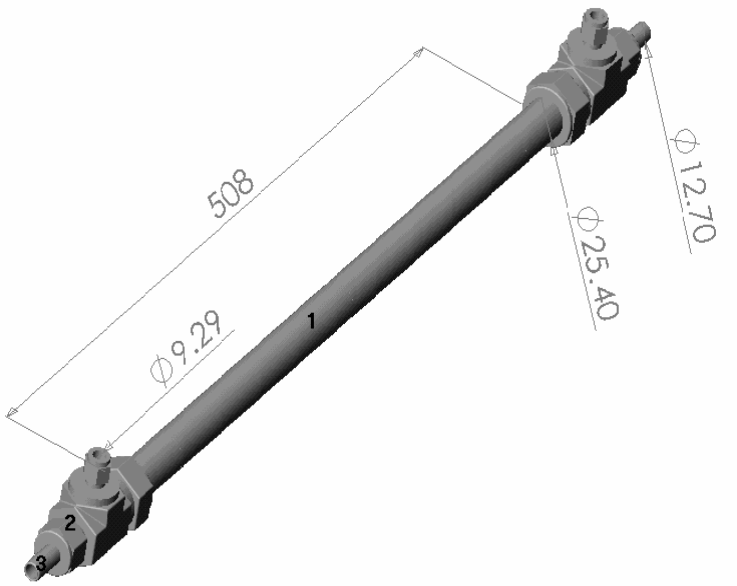

Figure A.25 View of Air

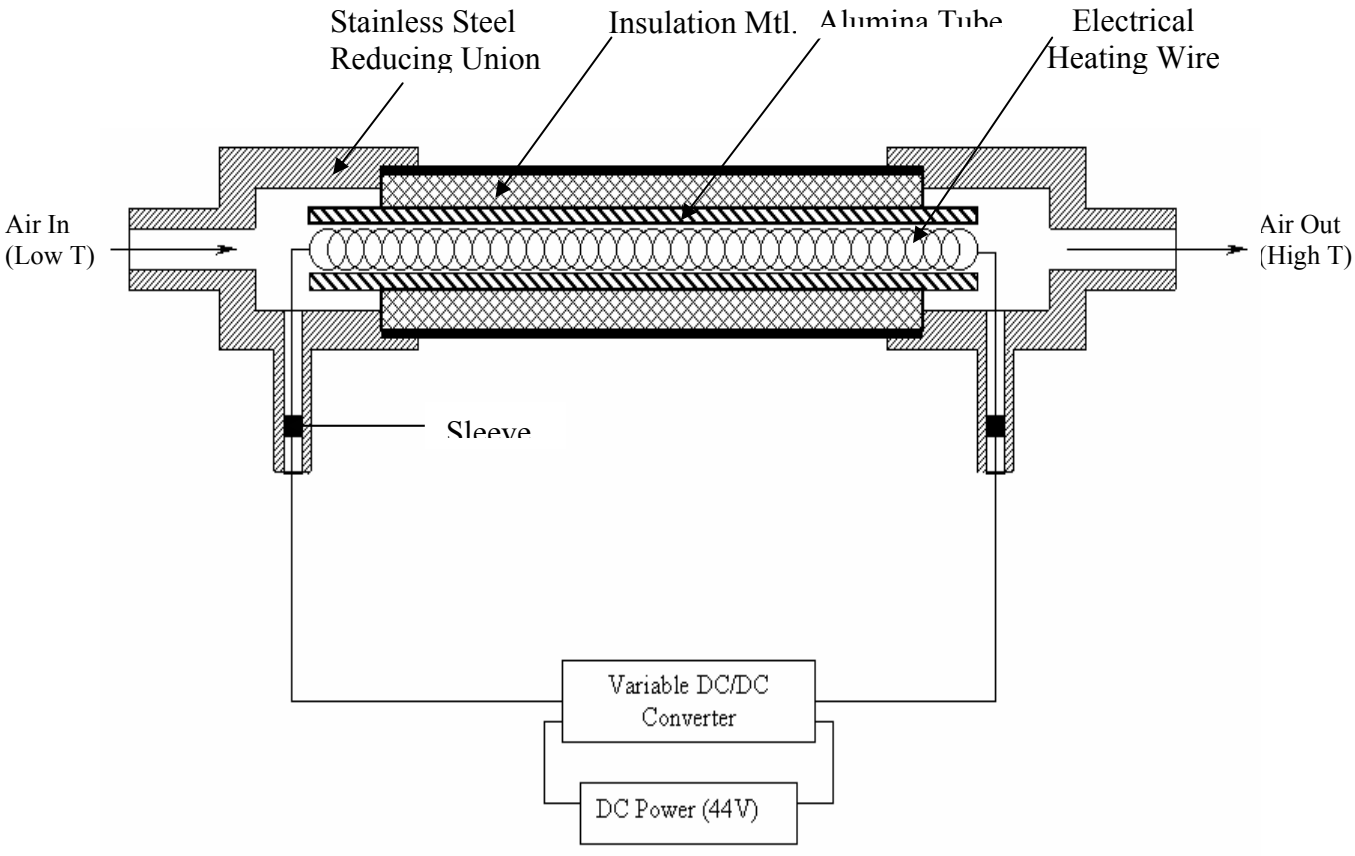

Figure A.26 Section View of Air Preheater

The descriptions of components are brought in Table A.7 and Table A.8.

Table A.7 Components of Air Preheater

No.	Description	Amount
1	304 stainless steel with O.D 1”	1
2	Reducing union SS-1610-3-12-6 (Swagelok)	2
3	Port connector SS-1211-PC-8 (Swagelok)	2

Table A.8 Accessories of Preheater

Hot Wire	Kanthal AF Wire, 24 Gage
Insulation Material 1. Alumina Paper 2. Sleeving	 APA-1, 18”X24” (Zircar Ceramic Inc.) Nextel 440 (OMEGA)

The energy needed to heat the air flow (14 SCFH) is given in Table A.9.

Table A.9 The Energy Needed to Heat Air (Assuming 80% Transfer Coefficient)

Air Preheated Temperature (°C)	Heat Transfer Rate (w)
800	112.7
900	127.84
1000	142.9
1100	158.5

Air Preheater Output Temperature Controller

To control the temperature of preheated air, Watlow Seies 93 temperature controller has been used. This temperature controller is a 1/16 DIN microprocessor-based temperature controller. There is a single input which accept J,K,T,N or S thermocouple, RTD or process input. There are dual outputs; the primary output can be heating or cooling while the secondary output could be a control output opposite the primary output (heat or cool), alarm or none. A mechanical relay was ordered to turn on or turn off the current to power supply by temperature controller. The

temperature controller acts based on a thermocouple, which measures the output temperature of, preheated air.

A.1.2.2 Coolant Line

There is a CO_2 line in this rig, and the CO_2 is conducted through burner. CO_2 is used to cool the fuel to room temperature and the exhausted CO_2 can also cool the whole rig. All of the pipes are ¼" SS Swagelok. The relief valve 33 is set at 35 psi. The upstream pressure in the coolant line is nominally set in the range of 8 to 12 psig. The plumbing diagram for the coolant line is given in Appendix D.

A.1.2.3 Fuel Line

Fuel line contains some quick connector for easy and rapid connection. Some union tee for adding components like valve and measurement instrumentation are incorporated into the plumbing line. Similarly various valves such as needle valve, relief valve are incorporated. Flow measurement components for the measurement of pressure and mass flow are incorporated into the plumbing line and use pressure transducer and mass flow controller. For regulation of fuel flow, flow regulator is used. Before the burner, two solenoid valves are applied for more safety. All of the components are connected using ¼" SS pipes. Also, relief valve 52 is set at 25psi. The pressure in the fuel line is set to 5 psig. The revised version of the plumbing diagram for the fuel line (and also air and coolant lines) is given in Appendix D. An internal electromagnetic flow controller controls the mass flow rate. Command signal

is supplied by the internal set point the output will be 0-5 VDC linear or 4-20 mA linear.

Some tests have been made to determine the flow rate range for the fuel. The range should be between 0.1 SCFH to 0.25 SCFH. With the previous HiTAC experiment done in our lab, the ratio volume flow rate of fuel and air should be kept at 0.1, that is $\frac{\dot{V}_{fuel}}{\dot{V}_{air}} = 0.1$. So the corresponding air flow rate range should be from 9.52SCFH to 23.81SCFH. At present, we choose fuel flow rate of 0.15 SCFH as our main operation point. For this fuel flow rate the corresponding airflow rate is 14 SCFH. When this airflow rate has been fixed the equivalence ratio can be changed by changing oxygen concentration in air, see Table A.10 below:

Table A.10 Oxygen Concentration, Flow Rates and Equivalence Ratios (at 14 SCFH)

Oxygen Concentration (%)	O_2 Flow Rate (SCFH)	N_2 Flow Rate (SCFH)	Equivalence Ratio (SCFH)
2%	0.28	13.72	1.07
3.5%	0.49	13.51	0.612
5%	0.7	13.3	0.429
8%	1.12	12.88	0.268
15%	2.1	11.9	0.143
21%	2.94	11.06	0.1

A.1.3 Control Panel

A schematic diagram (Figure A.27) gives a global picture of control panels in frame. The control panels are made of metal plates, electrical control panel for digital displays, switches and electronic control devices whose illustration are given in

Figure A.28, also the layout of its electrical components is illustrated in Figure A.29 and Mechanical control panel which pressure regulators and needle valves are mounted on it. Figure A.30 gives a picture of mechanical control panel. The Research Group at UMCP will assemble all these components onto metal plates. NASA will provide the wiring of these components.

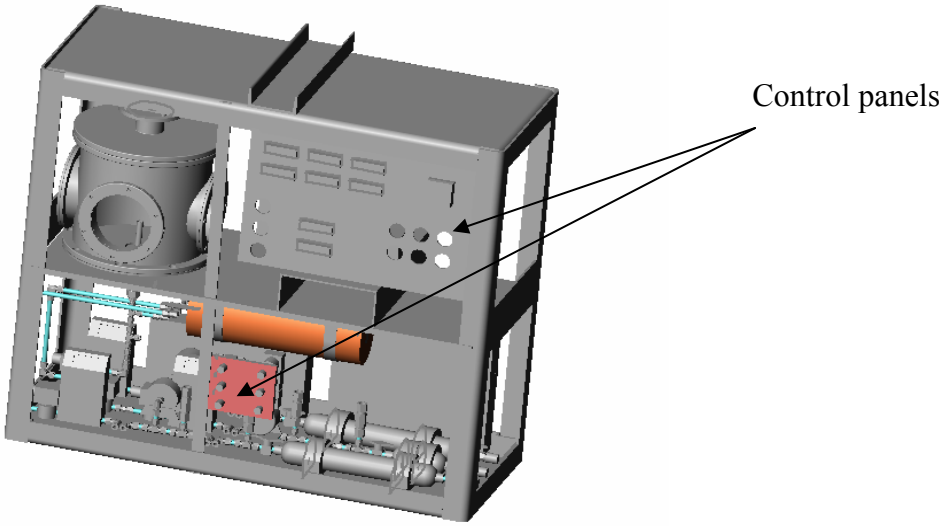

Figure A.27 Location of Control Panels into Frame

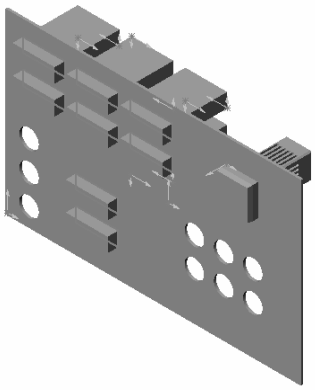

Figure A.28 Electrical Control Panel

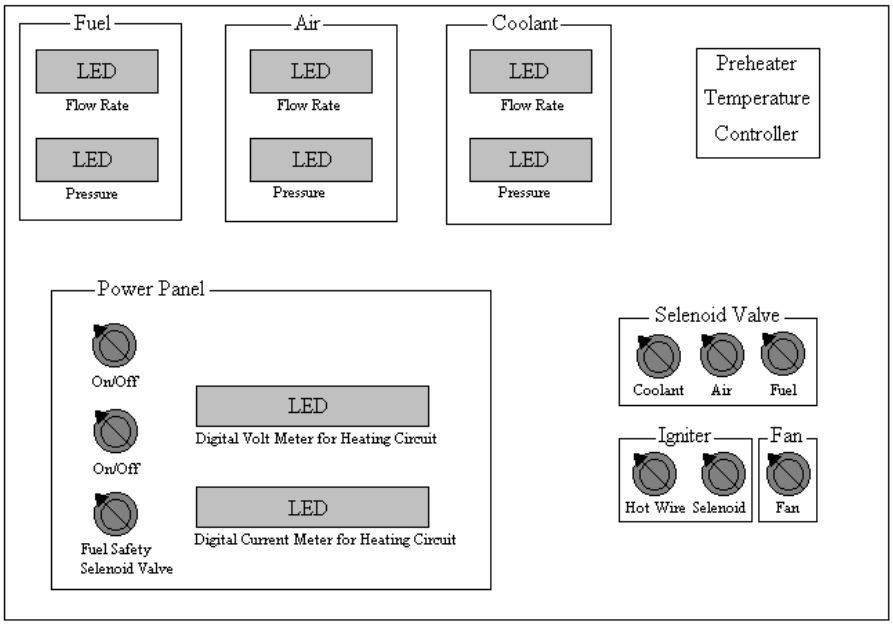

Figure A.29 The Layout of Components in Control Panel

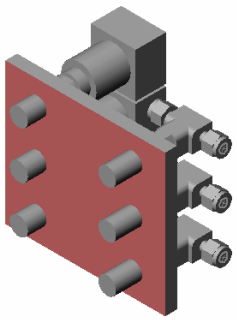

Figure A.30 Mechanical Control Panel

Fuel Line Control

Table A.11 The Specifications of Fuel Line Control

Items	Part No.	Supplier	Dimension (mm)
Flow Rate LED	DPF51-PV3-7/32	OMEGA	72X24 (LXH)
Pressure LED	DPF51-PV3-7/32	OMEGA	72X24 (LXH)
Flow Regulator	44-2262-242	Tescom	Dia. 60
Needle Valve	SS-20KM4-F4	Whitey	Dia. 26
Mass flow meter and controller	FMA-A2403	omega	89X153(LXW)

Air Line Control

Table A.12 The Specifications of Air Line Control

Items	Part No.	Supplier	Dimension (mm)
Flow Rate LED	DPF51-PV3-7/32	OMEGA	72X24 (LXH)
Pressure LED	DPF51-PV3-7/32	OMEGA	72X24 (LXH)
Metering Valve	SS-22RS4	Swagelok	Dia. 10
Flow Regulator	44-2262-242	Tescom	Dia. 60
Ball Valve	SS-42S4	Swagelok	Dia. 48

Coolant Line Control

Table A.13 The Specifications of Coolant Line Control

Items	Part No.	Supplier	Dimension (mm)
Flow Rate LED	DPF51-PV3-7/32	OMEGA	72X24 (LXH)
Pressure LED	DPF51-PV3-7/32	OMEGA	72X24 (LXH)
Metering Valve	SS-22RS4	Swagelok	Dia. 10
Flow Regulator	44-2262-242	Tescom	Dia. 60
Needle Valve	SS-20KM4-F4	Whitey	Dia. 26

Power Control

Table A.14 The Specifications of Power Control

Items	Part No.	Supplier
On/Off Switch		
On Sign		
Safety Solenoid Valve	8262G86-24VDC	Asco
Voltage Meter		
Current Meter		

Solenoid Valve Control

Table A.15 The Specifications of Solenoid Valve Control

Items	Part No.	Supplier
Fuel Solenoid Valve	8262G86-24VDC	Asco
Air Solenoid Valve	8262G86-24VDC	Asco
Coolant Solenoid Valve	8262G86-24VDC	Asco

Preheater Control

Table A.16 The Specifications of Preheater Control

Item	Part No.	Supplier
On/Off Switch		
On Sign		
Temp. Controller	93BB-1CA0-00RR	Watlow Series 93
Temperature Meter & LED	DPI32-DC	OMEGA

Installation of Control Panel

The control panel should be installed particularly on edge of the upper supporting plate . The bottom and right edge of control panel should be along the frame.

Electric wiring

The layout for the electrical wiring should be done as shown in Figure A.31 below. The voltage and current requirement of all electronic components are given in Table A.17. There are two main circuits:

One circuit supports the igniter and preheater. This circuit contains: 2X24VDC battery pack, power switch, igniter components (switch, solenoid and hotwire), preheater components (variable DC/DC converter, potential meter and hot wire)

The other circuit contains all element devices and camera system. In this circuit, 24 VDC, power switch and 24VDC/12VDC converter are used, see in Figure A.32,

Two circuits would be independent of each other. There is a ground in test rig for protecting ground fault.

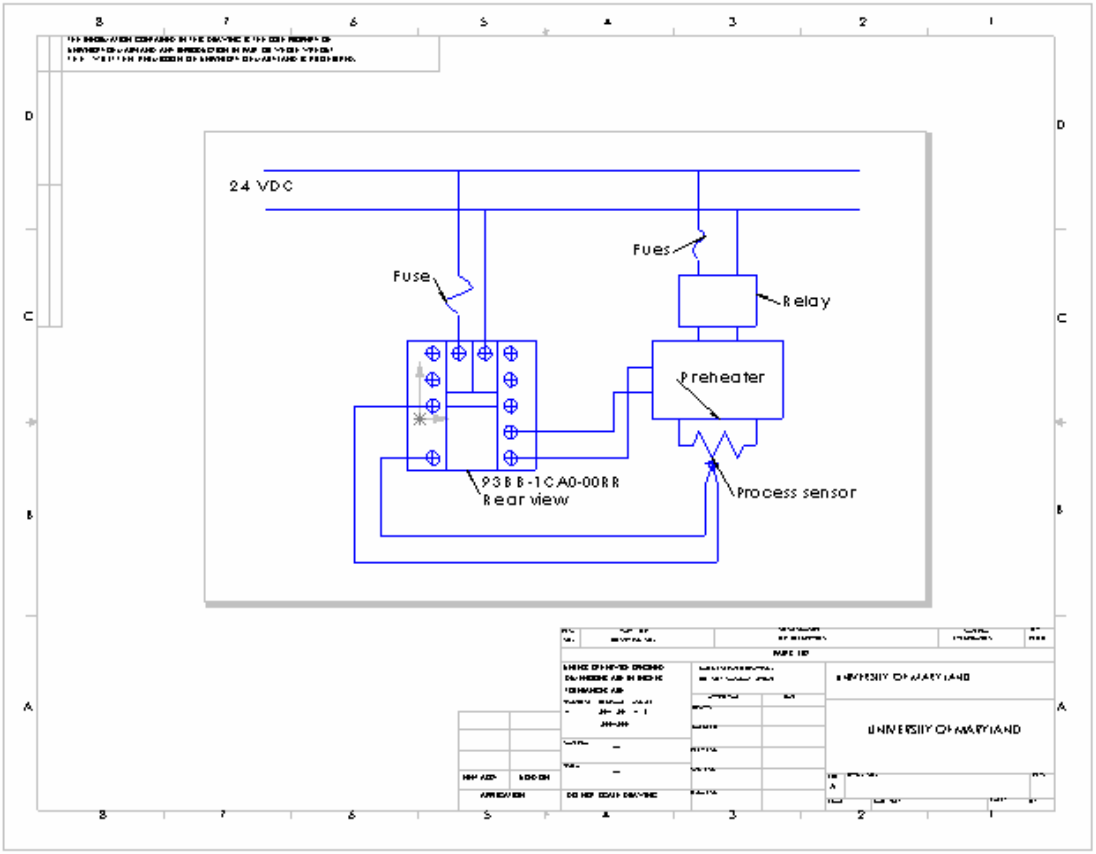

Figure A.31 Electrical Wiring of Preheater

Table A.17 List of Voltage and Current/Power Requirements of All Components

Name	Part No.	Voltage	Current or Power	Suppliers
Components in Fuel Line				
Flow Rate LED	DPF51-PV3-7/32	7~32VDC	2 Watts	Omega
Mass Flow Controller	FMA-A	24VDC	300mA	Omega
Pressure Transducer LED	DPF51-PV3-7/32	7~32VDC	2 Watts	Omega
Pressure Transducer	204	24VDC	100mA	Setra
Solenoid Valve	8262G86	24VDC	10.6 Watts	Asco
Safety Solenoid Valve	8262G86	24VDC	10.6 Watts	Asco
Components in Coolant Line				
Flow Rate LED	DPF51-PV3-7/32	7~32VDC	2 Watts	Omega
Mass Flow Meter	FMA-18-12-ST	12VDC	200mA	Omega
Pressure Transducer LED	DPF51-PV3-7/32	7~32VDC	2 Watts	Omega
Pressure Transducer	204	24VDC	100mA	Setra
Solenoid Valve	8262G86	24VDC	10.6 Watts	Asco
Components in Air Line				
Flow Rate LED	DPF51-PV3-7/32	7~32VDC	2 Watts	Omega
Mass Flow Meter	FMA-18-12-ST	12VDC	200mA	Omega
Pressure Transducer LED	DPF51-PV3-7/32	7~32VDC	2 Watts	Omega
Pressure Transducer	204	24VDC	100mA	Setra
Thermometer	DPI32-DC	10~34VDC	5 Watts	Omega
Solenoid Valve	8626G86	24VDC	10.6 Watts	Asco
CCD Camera	CV-S3300N	12VDC	3 Watts	JAI
Igniter	Custom Made	24VDC	8A	Custom Made
Solenoid of Igniter	9572/0016	24VDC	200mA	MSA
Preheater	Custom Made	44VDC	Variable	Custom Made

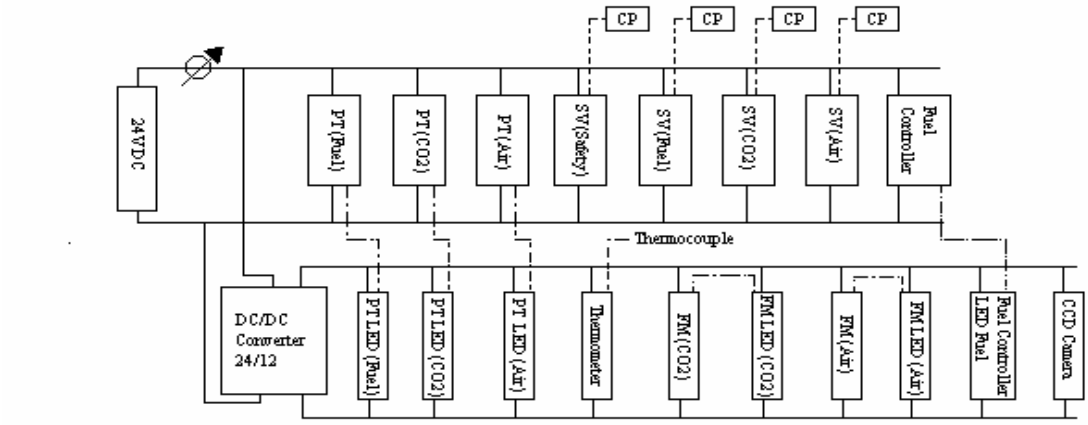

Figure A.32 Electrical Wiring Layout

Appendix B: Operational instruction

Step-1: Turn on the main power switches (one for heating circuit and the other for electronic components).

Step-2: Turn on the coolant solenoid valve.

Step-3: Adjust the flow rate and pressure of coolant

Step-4: Turn on the air solenoid valve.

Step-5: Adjust the pressure and flow rate of air.

Step-6: Turn on the solenoid so that the igniter position is on top of the fuel nozzle in the burner. Then turn on the igniter (hot wire may take 10 to 15 seconds to get red hot).

Step-7: Turn on the fuel solenoid valves. (There are two solenoid valves in the fuel line. One of them is used for additional safety so that the switches off after the experiments). Ignite the fuel.

Step-8: Adjust the fuel pressure and flow rate.

Step-9: Check the pressure and flow rate of fuel, air and coolant. It should take about 15 seconds.

Step-10: Turn on the air preheater and adjust the temperature of air.

Step-11: Adjust and focus the lens for zoom on the CCD camera.

Step-12: Lower the drag shield over the experimental rig.

Step-13: Turn on the Camcorder to begin recording. Give warning signal on the drop test. Drop the rig.

After Experiment:

Step-14: Turn off the camcorder to stop recording.

Step-15: Turn off the solenoid valves in the sequence of fuel, air and coolant.

Step-16: Turning off fuel safety solenoid valve.

Step-17: Turn off the power in the rig so that the electrical heater, igniter and other components are switched off.

Appendix C: Safety

Touch Temperature

The components described for the experimental rig fabrication should be designed and operated in a safe way. The burner assembly consists of a cylindrical burner, in which the fuel is injected on the central axis, surrounding which high temperature combustion air is injected. Electrical heating produces the high temperature of the air. Tests conducted showed that the temperature of air could be raised to about 1100°C. The air-preheater will be well insulated and temperature on the outer surface of the insulation will be near room temperature. Similarly the pipes connecting the air preheater to the burner will be well insulated to minimize the heat losses and maintain the high air preheat temperature.

Solenoid Valves for Fuel

Two solenoid valves are used in the fuel line before supplying the fuel to the burner to assure safety in case of any unwanted fuel discharge into rig shield between the drops. These valves will be nominally closed and only opened for fixed time duration of the experiments in the drop tests. At the conclusion of the drop, after prescribed time duration of few seconds the solenoid valves will be closed. This will assure that there is no hazard associated with the fuel leaks during the experiments since the mixture ratio will be well outside the flammability limits. The fuel tank will be securely mounted to the frame in the rig.

Piping

For safety and robustness, all plumbing lines are made of stainless steel.

Electric Shock

With the exception of the fast-acting solenoid valve, the rig operates at a maximum of 48 Volts (down to 44 volts). Also, the rig is equipped with fuses and grounded to prevent shorts and electrical shock.

Fire Protection

Burner and igniter are located inside the combustion chamber so that no spark emanating from outside the combustion chamber can have an influence to ignite the fuel-air mixture inside the combustion chamber. Similarly no burning fuel can escape outside of the combustion chamber. The igniter located in the combustion chamber is only allowed to heat when desired. This prevents any possibility of unwanted fire development.

Chamber Pressure

The chamber operates at one atmosphere pressure, so that there is no safety issue related to high-pressure operation of the combustion chamber.

Leakage

With suppose that there is some release of fuel in combustion chamber and in test rig for some reason. Therefore the flammable time limit must be calculated in

case of fuel release in the combustion chamber. Calculations given below are on the nature of the flammability limits for the mixture. First of all, volume of combustion chamber is

$V = 0.0129 m^3$

The amount of stoichiometric fuel air ratio (using methane as the fuel) can be obtained from reaction formula.

$$\left.\frac{A}{F}\right)_{Stoich} = 9.52$$

So we can obtain the amount of fuel

$V_f = 1.355 \times 10^{-3} m^3$

In case of lean limit for methane (0.46), we have

$V_{lean\_limit\_fuel} = 6.23 \times 10^{-4} m^3$

For fuel flow of 0.00704 SCFH we can obtain the flammable time limit.

$t \approx 166 \min$

Similar calculations have been done for propane as the fuel and also by considering the volume as the entire volume of the rig. A summary of the results for the flammable time limits are shown below in Table C.1.

Table C.1 Flammable Time Limits

Volume / Fuel	Frame	Combustion Chamber
CH_4	4781 minutes	166 minutes
C_3H_8	2122 minutes	83 minutes

For supporting fuel of test rig for 15 minutes, 0.00822 ft^3 fuel will be put into fuel cylinder. In case of releasing all the fuel into test rig calculation shows that we will not reach to flammability limit into test rig. For methane the lean limit condition is 0.561 ft^3 and for propane this limit is 0.2488 ft^3 which both of them are greater than the whole amount of supporting fuel in the cylinder.

Appendix D: Plumbing Diagram for Air, Fuel and Coolant Lines

Fuel Line

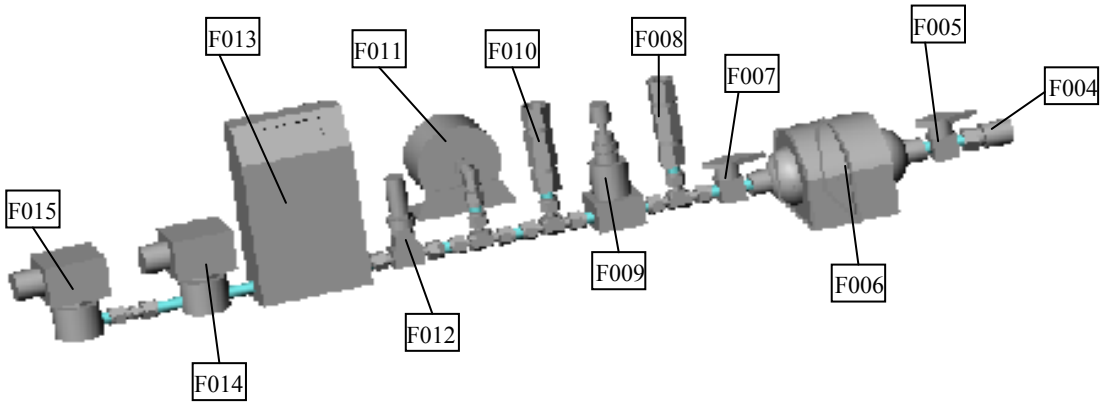

No.	ITEM	MFR.	TYPE	SIZE	W.P.PSIG
F001	Quick Connect Body	Swagelok	SS-QC4-B1-400	1/4 TUBE	
F002	Reducer				
F003	Filter	Swagelok	B-4TF-05	1/4 TUBE	1500
F004	Quick Connect Body	Swagelok	SS-QC4-B1-400	1/4 TUBE	
F005	Plug Valve	Swagelok	SS-4P4T2-M1	1/4 MNPT	
F006	Fuel cylinder	Whitey	304L-HDF4-150		1800
F007	Plug Valve	Swagelok	SS-4P4T1	1/4 MNPT	
F008	Relief Valve	Swagelok	SS-4CPA4-150	1/4"	150-300
F009	Pressure Regulator	Scott gas	51-23A-100	1/8 FNPT	250
F010	Relief Valve	Swagelok	SS-4CPA4-150	1/4"	150-300
F011	Pressure Transducer	Asco	HPO-W3-1-500-P	1/4 FNP	1000
F012	Needle Valve	Whitney	SS-20KM4-F4	1/4"	
F013	Mass Flow Controller	Omega	FMA-A2403	1/4"	250
F014	Solenoid Valve	Asco	8262G86-24VDC	1/4"	150
F015	Solenoid Valve	Asco	8262G86-24VDC	1/4"	150
F016	Filling block				

Air Line

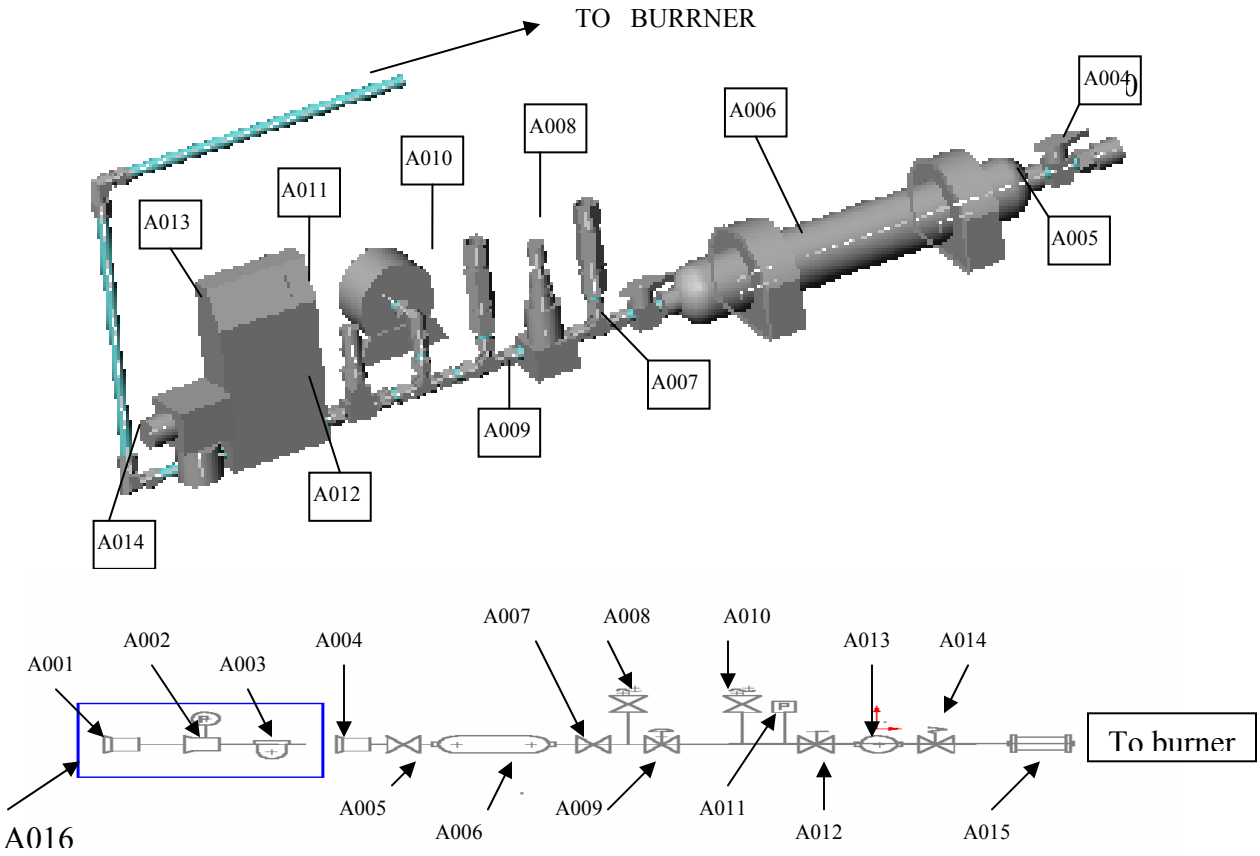

No.	ITEM	MFR.	TYPE	SIZE	W.P.PSIG
A001	Quick Connect Body	Swagelok	SS-QC4-B1-400	1/4 TUBE	
A002	Reducer				
A003	Filter	Swagelok	B-4TF-05	1/4 TUBE	1500
A004	Quick Connect Body	Swagelok	SS-QC4-B1-400	1/4 TUBE	
A005	Plug Valve	Swagelok	SS-4P4T2-M1	1/4 MNPT	
A006	Air Cylinder	Whitey	304L-HDF4-500		1800
A007	Plug Valve	Swagelok	SS-4P4T1	1/4 MNPT	
A008	Relief Valve	Swagelok	SS-4CPA4-150	1/4"	150-300
A009	Pressure Regulator	Scott gas	51-23A-100	1/8 FNPT	250
A010	Relief Valve	Swagelok	SS-4CPA4-150	1/4"	150-300
A011	Pressure Transducer	Asco	HPO-W3-1-250-P	1/4"	500
A012	Metering Valve	Swagelok	SS-20KM4-F4	1/4"	
A013	Mass Flow Controller	Omega	FMA-A2403	1/4"	250
A014	Solenoid valve	Asco	8262g86-24vdc	1/4"	150
A015	Pre-Heater				
A016	Filling block				

Coolant Line

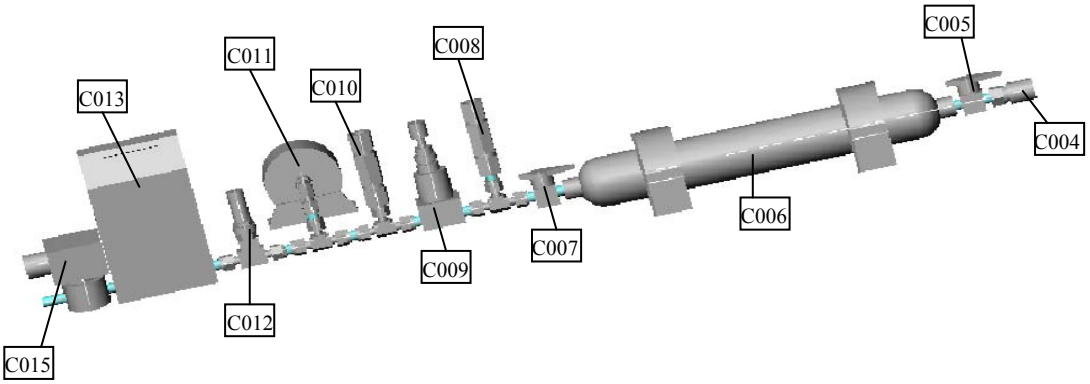

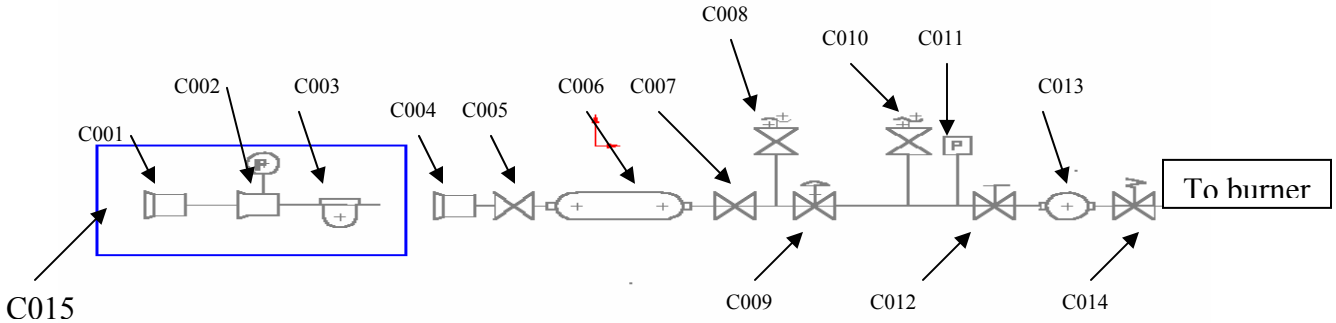

No.	ITEM	MFR.	TYPE	SIZE	No.
C001	Quick Connect Body	Swagelok	SS-QC4-B1-400	1/4 TUBE	C001
C002	Reducer				C002
C003	Filter	Swagelok	B-4TF-05	1/4 TUBE	C003
C004	Quick Connect Body	Swagelok	SS-QC4-B1-400	1/4 TUBE	C004
C005	Plug Valve	Swagelok	SS-4P4T2-M1	1/4 MNPT	C005
C006	Coolant cylinder	Whitey	304L-HDF4-500		C006
C007	Plug Valve	Swagelok	SS-4P4T1	1/4 MNPT	C007
C008	Relief Valve	Swagelok	SS-4CPA4-150	1/4"	C008
C009	Pressure Regulator	Scott gas	51-23A-100	1/8 FNPT	C009
C010	Relief Valve	Swagelok	SS-4CPA4-150	1/4"	C010
C011	Pressure Transducer	Asco	HPO-W3-1-500-P	1/4 FNP	C011
C012	Needle Valve	Swagelok	SS-20KM4-FA	1/4"	C012
C013	Mass Flow Controller	Omega	FMA-A2403	1/4"	C013
C014	Quick Connect Body	Swagelok	SS-QC4-B1-401	1/4 TUBE	C014
CO15	Filling Block				

References

[1] Tsuji, H., Gupta, A. K., Hasegawa, T., Katsuki, M., Kishimoto, K., and Morita, M., "High Temperature Air Combustion. From Energy Conservation to Pollution Reduction", CRC Press, 2003.

[2] Lloyd, S. A., and Weinberg, F. J., "A Burner for Mixtures of Very Low Heat Content", Nature, Vol. 251, pp. 47, 1974.

[3] Lloyd, S. A., and Weinberg, F. J., "Limits to Energy Release and Utilization from Chemical Fuels", Nature, Vol. 257, pp. 367, 1975.

[4] Lloyd, S. A., and Weinberg, F. J., "Heat-Recirculating Burners: Principles and Some Recent Development", Combustion Science and Technology, Vol. 12, pp. 3, 1996.

[5] Faeth, G. M., "Homogeneous Premixed and Nonpremixed Flames in Microgravity: A Review", Proceedings of the AIAA/IKI Microgravity Science Symposium – Moscow, AIAA, Washington, pp. 281-293, 1991.

[6] Law, C. K., and Faeth, G. M., "Opportunities and Challenges of Combustion in Microgravity", Progress in Energy and Combustion Science, Vol. 20, pp. 65-113, 1994.

[7] Ross, H. D., "Microgravity Combustion: Fire in Free Fall", Academic press, 2001.

[8] Jaluria, Y., “Basics of Natural Convection, Handbook of Single Phase Heat Transfer”, pp. 12.1-12.31, Hemisphere, New York, NY, 1985.

[9] Chung, S. H., and Law, C. K., ” Influence of Physical Mechanisms on Soot Formation and Destruction in Droplet Burning”, Combustion and Flame, Vol. 64, pp. 237-241, 1986.

[10] Ostrach, T. S., “Analysis of Natural Convection Heat Transfer Process”, Advanced Heat Transfer, Vol. 8, pp. 161-181, 1972.

[11] Spalding, D .B., “Combustion and Mass Transfer”, Pergamon Press, New York, Ch. 10, 1979.

[12] Lin, K. C., and Faeth, G. M., “Shapes of Nonbuoyant Round Luminous Laminar Jet Diffusion Flames in Coflowing Air”, AIAA J., Vol. 37, pp. 759-765, 1999.

[13] Lin, K. C., and Faeth, G. M., Sunderland, P. B., Urban, D. L., and Yuan, Z. G., ”Shapes of Nonbuoyant Round Luminous Hydrocarbon/Air Laminar Jet Diffusion Flames”, Combustion and Flame, Vol. 116, pp. 415-431, 1999.

[14] Roper, F. G., “Prediction of Laminar Jet Diffusion Flames: Part I, Theoretical Model”, Combustion and Flame, Vol. 29, pp. 219-226, 1977.

[15] Roper, F. G., Smith, C., and Cunningham, A. C., "The Prediction of Laminar Jet Diffusion Flame Sizes: Part II, Experimental Verification", Combustion and Flame, Vol. 29, pp. 227-234, 1977.

[16] Sunderland, P. B., Mendelson, B. J., Yuan, Z. G., and Urban, D. L., "Shapes of Buoyant and Non-buoyant Laminar Jet Diffusion Flames", Combustion and Flame, Vol. 116, pp. 376-386, 1999.

[17] Cochran, T. H., and Masica, W. J., "An Investigation of Gravity Effects on Laminar Gas-Jet Diffusion Flames", Thirteen Symposium (International) on Combustion, Combustion Institute, Pittsburgh, PA, pp. 821-829, 1970.

[18] Haggard, J. B., and Cochran, T. H., "Stable Hydrocarbon Diffusion Flames in a Weightless Environment", Combustion Science and Technology, Gordon & Breach, Amsterdam, Netherlands, Vol. 5, pp. 291-298, 1972.

[19] Bahadori, M. Y., Edelman, R. B., Stocker, D. P., and Olson, S. L., "Ignition and Behavior of Laminar Gas-Jet Diffusion Flames in Microgravity", AIAA J., Vol. 28, pp. 236-244, 1990.

[20] Bahadori, M.Y., Stocker, D.P., Vaughan, D. F., Zhou, L. and Edelman, R B., "Modern Development in Energy, Combustion and spectroscopy", (F. A. Williams et al., eds.), Pergamon, New York, 1993.

[21] Bahadori, M. Y., Edelman, R. B., Sotos, R. G., and Stoker,.D. P., "Radiation Form Gas-Jet Diffusion Flames in Microgravity Environment",

29th Aerospace Sciences Meeting &. Exhibit, AIAA, Reston, VA, AIAA-9-0719, pp. 1-4, 1991.

[22] Bahadori, M. Y., Edelman, R. B., Stocker, D. P., Sotos, R. G., Vaughan, D. F., "Effects of Oxygen Concentration on Radiative Loss from Normal-Gravity and Microgravity Methane Diffusion Flames", 30th Aerospace Sciences Meeting & Exhibit, AIAA, Reston, VA, AIAA-92-0243, pp. 1-6, January 6, 1992.

[23] Schug, K. P., Manheimer Timnat, Y., Yaccarino, P., and Glassman, I., "Sooting Behavior of Gaseous Diffusion Flames and the Influence of Additives", Combustion Science and Technology, Vol. 22, pp. 235, 1980.

[24] Burke, S. P., and Schumann, T. E. W., "Diffusion Flames", Indust., Eng., Chem., Vol. 20, No. 10, pp. 998, 1928.

[25] Kuo, K. K., "Principles of Combustion", John Wiley & Sons, New York, pp 360, 1986.

[26] Klajn, M., and Oppenheim, A. K., "Influence of Exothermicity on the shape of a Diffusion Flame", Nineteenth Symposium (International) on Combustion, The Combustion Institute, Pittsburgh, Pa., pp. 223-235, 1982.

[27] Li, S. C., Gordon, A. S., and Williams, F. A., "A Simplified Method for the Computation of Burke-Schuman Flames in Finite Atmospheres", Combustion Science and Technology, Vol. 104, pp. 75-91, 1995.

[28] Ban, H., Vankatesh, S., and Saito, K., "Convection-Diffusion Controlled Laminar Flames", J. Heat Transfer, Vol. 116, pp. 954-959, 1994.

[29] Bahr, D.W., "Gas Turbine Combustion Problems", Hemisphere, Washington, DC, pp. 205-223. 1979.

[30] Haynes, B. S., and Wagner, H. G., "Soot Formation", Progress in Energy and Combustion Science, Vol. 7, pp. 229-273, 1981.

[31] Sunderland, P. B., Faeth, G. M., "Soot Formation in Hydrocarbon /Air Laminar Jet Diffusion Flames, Fall Technical Meeting of the Eastern States Section", Combustion Institute, Pittsburgh, PA, pp. 333-336, December 05, 1994.

[32] Sunderland, P. B., Mortazavi, S., Faeth, G. M., and Urban, D. L., "Laminar Smoke Points of Nonbuoyant Jet Diffusion Flames", Combustion and Flame, Vol. 96, pp. 97-103, 1994.

[33] Urban, D. L., Yuan, Z. G., Sunderland, P. B., Linteris, G. T., Voss, J. E., Lin, K. C., Dai, Z., Sun, K., and Faeth, G. M., "Structure and Soot Properties of Nonbuoyant Ethylene/Air Laminar Jet Diffusion Flames", AIAA J., Vol. 36, pp. 1346-1360, 1998.

[34] Sugiyama, G., "Non-luminous Diffusion Flame of Diluted Acetylene in Oxygen Enriched Air", 25th Symposium (International) on Combustion, The Combustion Institute, Pittsburgh, PA, pp. 601-608, 1994,

[35] Du, J., and Axelbaum, R. L., "The Effect of Flame Structure on Soot-Particle Inception in Diffusion Flames", Combustion and Flame, Vol.100, pp. 367-375. 1995.

[36] Sunderland, P. B., Axelbaum, R. L., and Urban, D. L., "Effects of Structure and Hydrodynamics on the Sooting Behavior of Spherical Microgravity Diffusion Flames", Fifth International Microgravity Combustion Workshop, Cleveland; NASA CP-1999-208917, pp. 475-478, 1999.

[37] Kang, K. T., Hwang, J. Y., Chung, S. M., and Lee, W., "Soot Zone Structure and Sooting Limit in Diffusion Flames: Comparison of Counterflow and Co-Flow Flames" Combustion and Flame, Vol. 109, pp. 266-281. 1997.

[38] Lin, K. C., and Faeth, G. M., "Structure of Laminar Permanently Blue, Opposed-Jet Ethylene-Fueled Diffusion Flames", Combustion and Flame, Vol.115, pp. 468-480, 1998.

[39] Lin, K. C., and Faeth, G. M., "Effects of Hydrodynamics on Soot Formation in Laminar Opposed-Jet Diffusion Flames", Journal of Propulsion and Power Vol. 12, No. 4, pp. 691-698, 1996.

[40] Kaplan, C. R., and Kailasanath, K., "Flow Field Effects on Soot Formation in Normal and Inverse Methane-Air Diffusion Flames", Combustion and Flame, Vol.12, pp. 275-294. 2001.

[41] Dai, Z., and Faeth, G. M., "Hydrodynamic Suppression of Soot Formation In Laminar Coflowing Jet Diffusion Flames" Proceedings of the Combustion Institute, Vol. 28, pp. 2085-2092. 2000.

[42] Syed, K. J., Steward, C. D., and Moss, "Modeling Soot Formation and Thermal Radiation in Buoyant Turbulent Diffusion Flames" J. B., Proceedings of the Combustion Institute, Vol. 23, The Combustion Institute, Pittsburgh, PA, pp. 1533, 1990.

[43] Xu, F., Dai, Z., and Faeth, G. M., "Flame and Soot Boundaries of Laminar Jet Diffusion Flames", AIAA Journal, Vol. 40, No. 12, pp. 2439-2446, 2002.

[44] Mahalingam, S., Ferziger, J. H., and Cantwell, B. L., "Self-Similar Diffusion Flame", Combustion and Flame, Vol. 82, pp. 231-234, 1990.

[45] Raffel, M., Willert, C. E., Kompenhans, J., "Particle Image Velocimetry" Springer-Verlag Berlin Heidelberg New York, 1998.

[46] Adrian, R. J., "Particle Image Techniques for Experimental Fluid Mechanics", Annual Rev. Fluid Mech., Vol. 23, pp. 261-304, 1991.

[47] Bernard, P., Wallace, J., "Turbulent Flow: Analysis, Measurement, and Prediction", John Wiley & Sons, Inc., 2002.

[48] Adrian, R. J., and Yao, C. S., "Pulsed Laser Technique Application to Liquid and Gaseous Flow and the Scattering Power of Seed Materials", Applied Optics, Vol. 24, pp. 44-52, 1987.

[49] Blackwelder, R. F., "Hot-Wire and Hot Film Anemometry", Methods of Experimental Physics: Fluid Dynamics, American Press, New York, 1981.

[50] Gupta, A. K., Lourenco, L., Linck, M., and Archer, S., "New Particle-Image-Velocimetry Method to Measure Flowfield in Luminous Spray Flames", J. Propulsion and Power, Vol. 20, No. 2, pp. 369-372, March-April 2004.

[51] Gaydon, A. G., "The Spectroscopy of Flames", Chapman and Hall Ltd., London 1974.

[52] Kitagawa, k., Nitta, S., Shinoda, M., and Arai, N., "Spectroscopic Observation and Stabilization During Combustion of Hydrocarbon with Pre-Heated Air", The First Aisa-Pasific Conference on Combustion May 12-15, Osaka, Japan, 1997.

[53] Ishiguro, T., Tsuge, S., Furuhata, T., Kitagawa, K., Arai, N., Hasegawa, T., Tanaka, R., Gupta, A. K. "Homogenization and Stabilization During Combustion of Hydrocarbons with Preheated Air", Twenty-Seventh Symposium on Combustion Institute, pp. 3205-3212, 1998.

[54] Konishi, N., Kitagawa, K., and Arai, N., "Two-Dimentional Spectroscopic Analysis of a Flame Using Highly Preheated Combustion Air", Journal of Propulsion and Power Vol. 18, No. 1, 2002.

[55] Ghaderi, M., Gupta, A. K., "Experimental Investigation on the Effect of Highly Preheated Air Diffusion Flames", Proceeding of ASME Power Conference, Baltimore, Maryland, USA, March 30 – April 1, 2004, Paper No. PWR 2004-52179.

[56] Han, D., Mungal, M. G., "Simultaneous Measurements of Velocity and CH Distributions. Part 1: Jet Flames in Coflow", combustion and flame, Vol. 132, pp. 565-590, 2003.

[57] Donbar, J. M., Driscoll, J. F., Carter, C. D., "Reaction Zone Structure in Turbulent Nonpremixed Jet Flames—from CH-OH PLIF Images**",** Combustion and Flame, Vol.122, pp. 1-19, 2000.

[58] Watson, K. A., Lyons, K. M., Donbar, J. M., Carter, C. D., "Simultaneous Rayleigh Imaging and CH-PLIF Measurements in a Lifted Jet Diffusion Flame**",** Combustion and Flame, Vol. 123, pp. 252-265, 2000.

[59] Gerhard, H., "Molecular Spectra and Molecular Structure, Spectra of Diatomic Molecules", Van Nostrand Rienhold, New York, pp. 78, 1950.

[60] Dasch C. J., “One-Dimensional Tomography; A Comparison of Abel, Onion-Peeling, and Filtered Back projection Methods”, Applied Optics, Vol. 31, pp. 1146-1152, 1992.

[61] Santoro, R. J., Yeh, T. T., Horvath, J. J. and Semerjian, H. G., "The Transport and Growth of Soot Particles in Laminar Diffusion Flames" Combustion Science and Technology, Vol. 53, pp. 89-115, 1987.

[62] Friedman, R., and Burk, E., “Measurement of Temperature Distribution in Low Pressure Flat Flame”, J. Chem. Phys., Vol. 22, pp. 824, 1954.

[63] Hussaini, M. Y., Kumar, A., Voigt, R. G., “Major Research Topics in Combustion”, Springer-Verlag, pp. 23-44, 1991.

[64] Lim., J., Gore, J., and Viskanta, R., “A Study of the Effects of Air Preheat on the Structure of Methane/Air Counterflow Diffusion Flames”, Combustion and Flame, Vol. 121, pp. 262-274, 2000.

[65] Guo, H., Liu, F., Smallwood, G. J., and Gulder, O. L., “The Flame Preheating Effect on Numerical Modeling of Soot Formation in a Two – Dimensional Laminar Ethylene – Air Diffusion Flame”, Combustion Theory and Modeling, Vol. 6, pp.173-187, 2002.

[66] Ronney, P. D., “Understanding Combustion Process Through Microgravity Research”, Twenty-Seventh Symposium On Combustion, the Combustion Institute, 1998, pp. 2485-2506, 1998.